An Old but New Issue; Viscous Properties of Polymer Geosynthetic Reinforcement and Geosynthetic-Reinforced Soil Structures

F. Tatsuoka & D. Hirakawa
Department of Civil Engineering, Tokyo University of Science, 2641, Yamazaki, Noda-shi, Chiba, 278-8510, Japan
tatsuoka@geot.t.u-tokyo.ac.jp & dhirakaw@rs.noda.tus.ac.jp

M. Shinoda
Structures Technology Division, Railway Technical Research Institute, 2-8-38, Hikari-cho, Kokubunji-shi, Tokyo, 185-8540, Japan
shinoda@rtri.or.jp

W. Kongkitkul & T. Uchimura
Department of Civil Engineering, the University of Tokyo, 7-3-1, Hongo, Bunkyo-ku, Tokyo, 113-8656, Japan
warat@geot.t.u-tokyo.ac.jp & uchimura@geot.t.u-tokyo.ac.jp

Abstract: Viscous deformation characteristics of geosynthetic as well as those of backfill and geosynthetic-reinforced soil structures are discussed based on results from laboratory load/stress-strain tests of geosynthetic and backfill as well as behaviours of small-scaled reinforced soil models and proto-type full-scale geosynthetic-reinforced soil structures and associated numerical simulations of experimental results, including FE simulations. The following remarks are presented: a) creep is not a degrading phenomenon with both geosynthetic and backfill, while the isochronous concept is not able to relevantly predict the load/stress-strain time behaviour of geosynthetic as well as soil and reinforced backfill subjected to arbitrary loading histories; b) a non-linear three-component rheology model is relevant to represent the viscous properties of geosynthetic and backfill; and c) tensile force in the geosynthetic arranged in the backfill subjected to sustained loading could decrease with time in ordinary field cases, where the safety factor against ultimate failure of the structure is sufficiently high. The design rupture strength of geosynthetic obtained using a relatively larger creep reduction factor determined based on the conventional creep rupture curve could be overly conservative. An alternative design procedure is tentatively proposed. It is demonstrated that the creep deformation rate substantially decreases; therefore the possibility of creep rupture of geosynthetic reinforcement can be eliminated, by applying a relevant preloading history.

1 INTRODUCTION

A great number of permanent geosynthetic-reinforced soil (GRS) structures were constructed due to their high cost-effectiveness and stability (e.g., Tatsuoka et al., 1997). Despite the above, it should be admitted that geosynthetic-reinforced soil (GRS) structures, including walls and abutments, are not as stiff as steel-reinforced concrete (RC) structures. Therefore, it is of paramount importance:

1. To become capable of accurately predicting the residual deformation when subjected to long-term sustained and cyclic loading:
2. To develop a relevant and rational design procedure taking into account the viscous properties of both backfill and geosynthetic reinforcement; and
3. To develop a method (or methods) that can effectively reduce the residual deformation by long-term sustained and cyclic loading.

These requirements are particularly important for GRS structures allowing a limited amount of residual deformation.

With respect to objective 1, it is not possible to properly predict such residual deformation by any elastic or elasto-plastic analysis, but it is possible only by taking into account the viscous properties of geosynthetic reinforcement and backfill and the effects of rate-independent cyclic loading effects when necessary (i.e., objective 2). With respect to objective 2, it is important to note that the development of residual deformation of backfill and geosynthetic by sustained and cyclic loading histories is not a degrading phenomenon. With respect to objective 3, the preloading procedure is effective to reduce residual strains caused by sustained and cyclic loading and thereby to eliminate the possibility of creep rupture of geosynthetic reinforcement.

In this paper, it is first shown that the current design procedure using a relatively large "creep reduction factor" could be overly conservative. It is particularly the case when the design rupture strength of geosynthetic reinforcement for seismic design of GRS structure is obtained by this method. Related to the above, it is then argued that the time history of strain and stress in geosynthetic reinforcement when GRS structure is subjected to sustained loading is controlled by the viscous properties of not only geosynthetic reinforcement but also backfill among other factors (i.e., reinforcement arrangement and interface friction). It is shown that, by an interaction between the effects of the viscous properties of geosynthetic reinforcement and backfill, during sustained loading of reinforced backfill, the tensile force acti-

vated in geosynthetic reinforcement arranged in the backfill may decreases with time. It is then shown that the current design procedure is linked to the Isochronous concept, while demonstrating that, when based on this concept, it is not possible to property predict the load-strain-time behaviour of geosynthetic reinforcement subjected to arbitrary loading histories (including sustained loading). A set of experimental data supporting these arguments, obtained from a series of special tensile loading tests on different types of geosynthetic reinforcements, are presented. Then, these experimental data are analysed by a non-linear three-component rheology model. The viscous properties of reinforced sand are then described and analysed. It is shown that, due to an interaction between effects of the viscous properties of sand and geosynthetic, the tensile force in the geosynthetic reinforcement arranged in a sand specimen subjected to sustained loading in plane strain compression decreased with time during sustained loading of the reinforced sand specimen. In this case, therefore, the potential for creep rupture of geosynthetic decreased with time. The non-linear three-component can be incorporated into a FEM code. FEM simulations of experimental data showing the viscous properties of geosynthetic reinforcement and geosynthetic-reinforced sand are presented. Then, it is shown that the residual strain of geosynthetic reinforcement that develops when subjected to cyclic loading is due essentially to yielding by an increase in the load and viscous deformation of geosynthetic, while rate-independent cyclic loading effects are negligible. Finally, it is shown that creep deformation rate of reinforced backfill can be made substantially small, or negligible, by relevant preloading with prestressing.

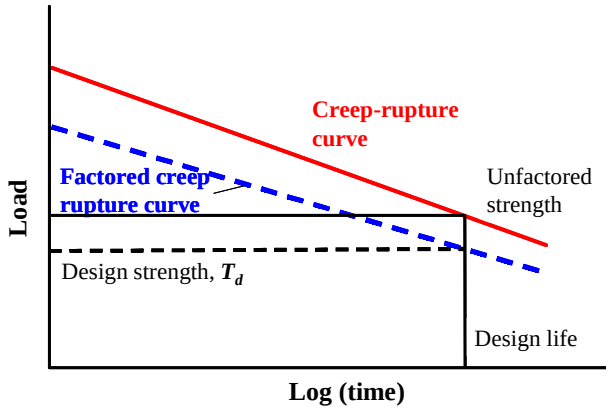

Fig 2-1 Current design assumptions relating to geosynthetic reinforcement under a sustained design load (Greenwood et al., 2001)

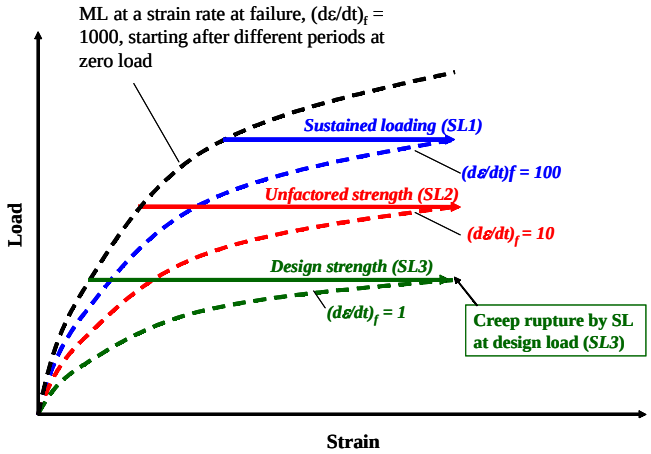

Fig. 2-2 Load-strain relations of geosynthetic reinforcement to obtain conventional rupture strength curve and residual strengths I.

2 REVIEW OF CURRENT DESIGN METHOD

2.1 *Introduction*

One of the advantages of the use of metal reinforcement is its high stiffness and rupture strength with a small creep deformation potential. On the other hand, one of the potential disadvantages of using metal reinforcement, in particular with strip metal reinforcement, is a relatively small contact area with backfill, which may result in a relatively high possibility of pull-out failure. Another large potential problem is a low bond stress when arranged in the backfill of a high water content clayey soil.

The advantages and disadvantages of the use of planar polymer geosynthetic reinforcement are inverse ones of the above. That is, due to its relatively low stiffness and strength, the deformation of GRS structure during construction is generally larger than that of metal-reinforced one under similar design and construction conditions. It is to be noted however that the deformation of reinforced soil structure at the end of construction, before opened to service, is usually not an engineering problem unless it is too large. Rather, excessive residual deformation of structure due to residual deformation of backfill and reinforcement that would take place after opened to service and creep rupture of reinforcement are among potential serious problems. The current design method aims at preventing the failure of reinforced structure due to creep rupture of geosynthetic reinforcement.

2.2 *Creep reduction factor*

Fig. 2-1 shows schematically the creep rupture curve for a given type of geosynthetic reinforcement, obtained by performing a set of sustained loading tests at different load levels leading to creep rupture (**Fig. 2-2**). In the current design method, it is usual that the rupture strength against static working load is obtained by substituting the specified design life into the creep-rupture curve as shown in **Fig. 2-3**. The same procedure is used to obtain the rupture strength against seismic load in some codes. The creep rupture strength obtained as above is then factored (i.e., reduced by the overall safety factor) to give the design strength, which is the same with the estimated applied load.

More specifically, the FHWA (1997) uses:

$$T_d = T_{ult} / \{RF_{CR} \cdot RF_D \cdot RF_{ID} \cdot (F_s)_{overall}\} \qquad (2\text{-}1)$$

where:

T_d is the long-term tensile design strength;

T_{ult} is the ultimate (or yield) tensile strength based on minimum average role value;

RF_{CR} is the creep reduction factor (larger than one);

RF_D is the durability reduction factor (typically 1.1 – 2.0);

RF_{ID} is the installation damage factor (typically 1.05 – 3.00); and

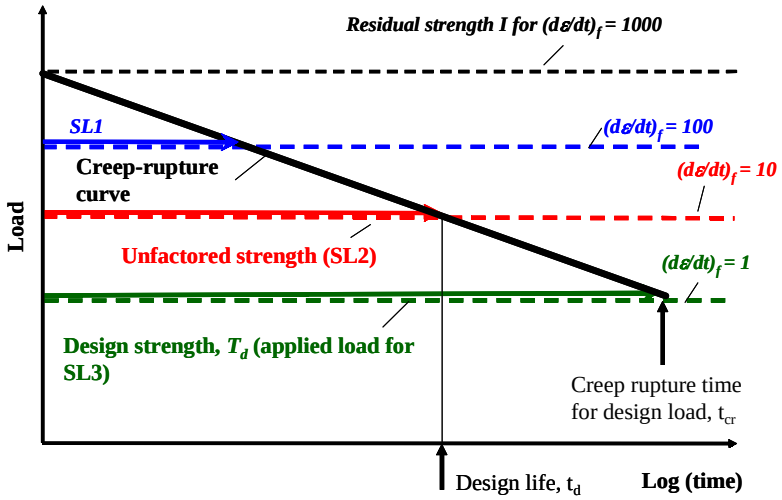

Fig. 2-3 Conventional creep rupture curve and residual strengths I for different strain rates at rupture.

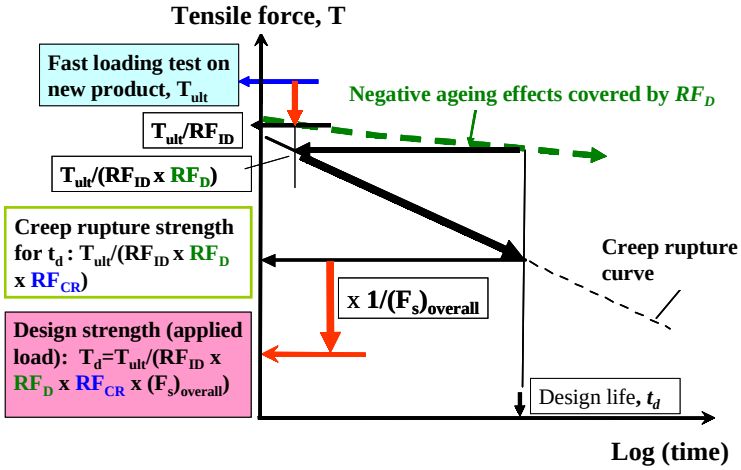

Fig. 2-4 FHWA design procedure to determine the design strength for a given design life time.

$(F_s)_{overall}$ is the overall factor of safety to account for uncertainties in the geometry of the structure, fill properties, and external applied loads. A minimum factor of safety of 1.5 has been typically used.

The meaning of Eq. 2-1 is illustrated in **Fig. 2-4**. T_d is the long-term tensile design strength, equal to the design applied load. The value of T_{ult} is obtained by tensile loading tests at a strain rate equal to 1.0 %/min or 5.0 %/min for, respectively, railway and highway structures in Japan, while 20 %/min in Europe and 10 %/min in the North America. As the rupture strength increases with an increase in the strain rate at rupture, the values of these factors depend on the strain rate by which T_{ult} is evaluated.

RF_D is the factor (larger than unity) to account for possible degrading due to long term chemical or biological effects (i.e., negative ageing effects). RF_{CR} is the creep reduction factor (larger than one), which is obtained from a given creep-rupture curve (as explained above). The values of RF_{CR} are not uniform among different types of geosynthetic reinforcement and among different countries. The typical values used in Japan are 1.43 - 1.82 (Polyester, PET) and 1.67 (HDPE). On the other hand, Elias and Christopher (1996) proposed relatively high values; 1.6 - 2.5 (PET), 4.0 -5.0 (Polypropylene, PP); and 2.6 -5.0 (HDPE). The typical values of these reduction factors are summarized in **Table 2-1**. **Table 2-2** lists the creep reduction factors for different geosynthetic types.

Despite its popular use, *"it (Fig. 2.1) is not a diagram of reduction in strength (for a given strain rate at rupture) against time, even though this may appear to be so. The strength of a geosynthetic (for a given strain rate at rupture) is in fact maintained until late in its service life."* (Greenwood et al., 2001). The notions in the parentheses in the quoted sentence were added by the authors based on the fact that the strain rate at creep rupture is not constant, but it decreases with an increase in the time to creep rupture. As shown in Chapter 5, experimental data showing that the rupture strength of geosynthetic is a function of strain rate at rupture, not time, are presented. Therefore, the creep rupture curve is not the upper bound, but we can go above it in case the tensile load is applied at a strain rate higher than the value at creep rupture at a certain time. That is, for a given elapsed time (e.g., a specified design life), the strength is not unique, but it is a function of strain rate at rupture, which would be different for different loading histories.

Table 2-1 Typical reduction factors in the current design procedures

	Durability reduction factor: RF_D	Installation damage factor: RF_{ID}	Creep reduction factor: RF_{CR}	References
Railways in Japan	1.0 – 1.35	1.0 – 1.2	1.4 – 1.8	RTRI (2000)
Highways in Japan	1.0 – 2.0	1.0 – 1.2	1.5 – 1.8	PWRI (2001)
FHWA	1.1 – 2.0	1.05 – 3.0	1.6 – 5.0	FHWA (2001)
GRI	1.4	1.4	3.0 or 3.5	GRI*

*) Geosynthetic Research Institute

Table 2-2 Typical creep reduction factor.

	Polyvinyl alcohol (PVA)[1)]	Polyamide (PA)[2)]	Polypropylene (PP)	Polyester (PET)	High-Density Polyethylene (HDPE)	Stiff / Flexible	References
Railways in Japan	1.43-1.82	1.43-1.67	1.67	1.43-1.82	1.67	-	RTRI (2000)
Highways in Japan	1.52-1.67	-	-	1.52-1.55	1.64-1.70	-	PWRI (2001)
FHWA	-	-	4.0-5.0	1.6-2.5	2.6-5.0	-	FHWA (2001)
GRI	-	-	-	-	-	3.5/3.0	GRI

1) Vinylon; 2) Nylon

On the other hand, the design strength obtained based on Eq. 2-1 decreases with an increase in the design life even when the strain rate at rupture is the same for different design lives. Therefore, the actual residual strength, which is the strength available at a given time, could be higher than the value evaluated based on the creep rupture curve (i.e., Eq. 2-1), being a function of loading history, as shown below. That is, the residual strength at a given design life could be much greater than anticipated following the current design procedure.

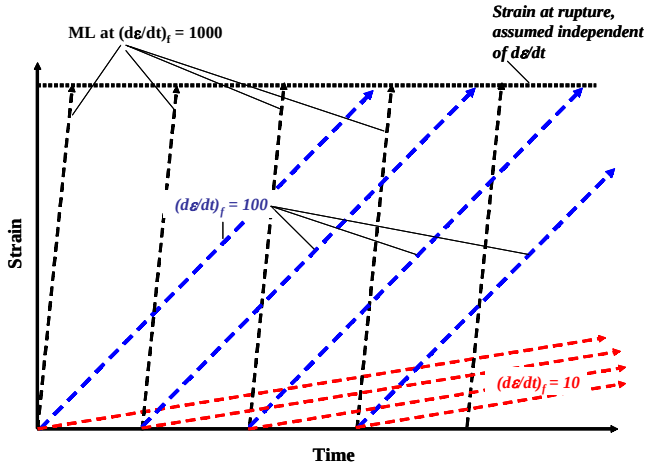

Fig. 2-5 Loading histories to obtain residual strengths I

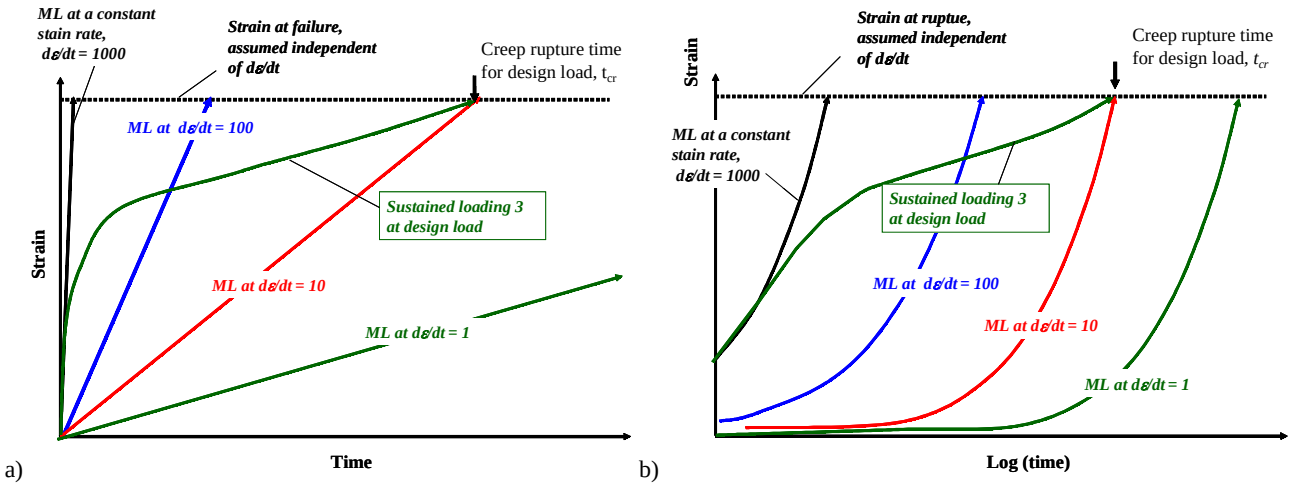

Fig. 2-6a Loading histories to obtain residual strengths II

2.3 *Residual strength*

Different residual strengths could be defined depending on different loading histories. In the following, several possible different definitions are presented.

Residual strength I: Suppose that we perform a set of ML tests at a certain strain rate starting after different periods lasting at zero load and repeat such ML tests for different constant strain rates, as illustrated in **Fig. 2-5**. To construct Figs. 2-2 and 2-5 (and other similar figures), it is assumed for a simplicity of illustration that the strain at rupture in ML is independent of strain rate. This assumption is consistent with experimental results for some types of geosynthetic reinforcement while not with others, as shown in Chapter 5. The arguments made herein are not affected by this assumption. Then, suppose that the load-strain curves for four different strain rates, as illustrated in Fig. 2-2, are obtained. Then, we obtain a set of residual strength curves I for different strain rates, as illustrated in Fig. 2-3. To construct these residual strength curves I, it is assumed that the rupture strength is independent of elapsed time at rupture. Data showing that the rupture strength is in proportional to the logarithm of strain rate at rupture are presented in Chapter 5.

For the loading histories depicted in Fig. 2-5, there is no possibility for creep rupture, as the load in the geosynthetic reinforcement is equal to zero during service life, which is not realistic with typical prototype GRS structures. Therefore, the use of this type of residual strength in design is not relevant.

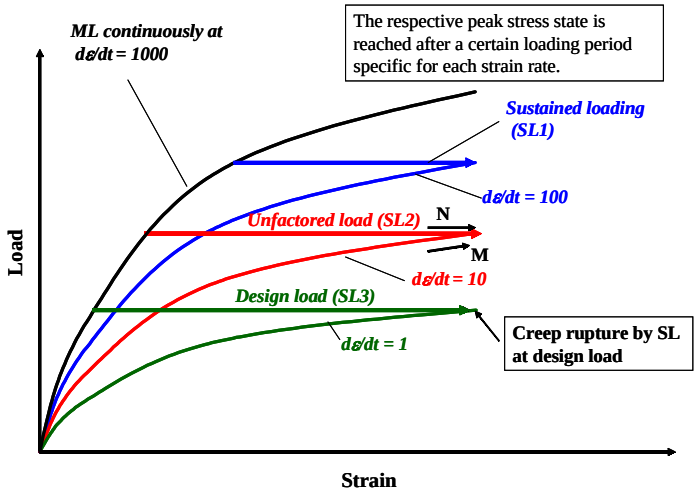

Fig. 2-7 Load-strain relations of geosynthetic reinforcement to obtain conventional rupture strength curve and residual strengths II.

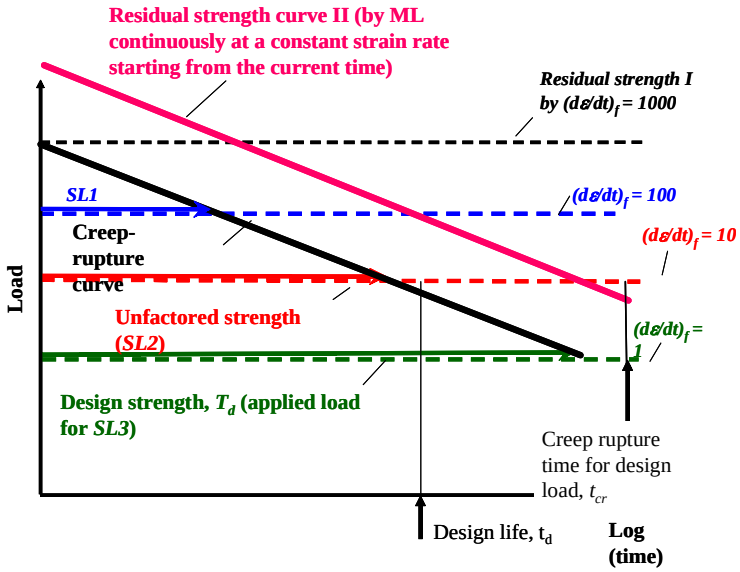

Fig. 2-8 Conventional creep rupture curve and residual strength curves I & II.

Residual strength II: This is the residual strength that is reached by ML continuously at a constant strain rate starting from the current time, as illustrated in **Fig. 2-6a** (in the arithmetic scale of time) and **Fig. 2-6b** (in the logarithmic scale of time). That is, ML continues at a constant strain rate from the present time (at zero elapsed time) until tensile rupture. **Fig. 2-7** shows the load-strain relations from these ML tests as well as the sustained loading tests starting from ML at dε/dt = 1,000, performed to obtain the conventional creep rupture curve (described above). The time history of sustained loading test 3 at the design load is presented in Figs. 2-6a and b.

Residual strength curve II obtained by performing a set of such ML tests is illustrated in **Fig. 2-8,** in which residual strength curve II is compared with the conventional creep-rupture curve and residual strength curves I for different strain rates at rupture. Although it is not very certain, it is herein assumed for the sake of simplicity that residual strength curve II is straight like the conventional creep rupture

curve, in this load – log(time) plot. It is also assumed that residual strength curve II and the conventional creep rupture curve are parallel to each other by considering the fact that the time difference between the two curves for a given load level should increase with a decrease in the concerned load level.

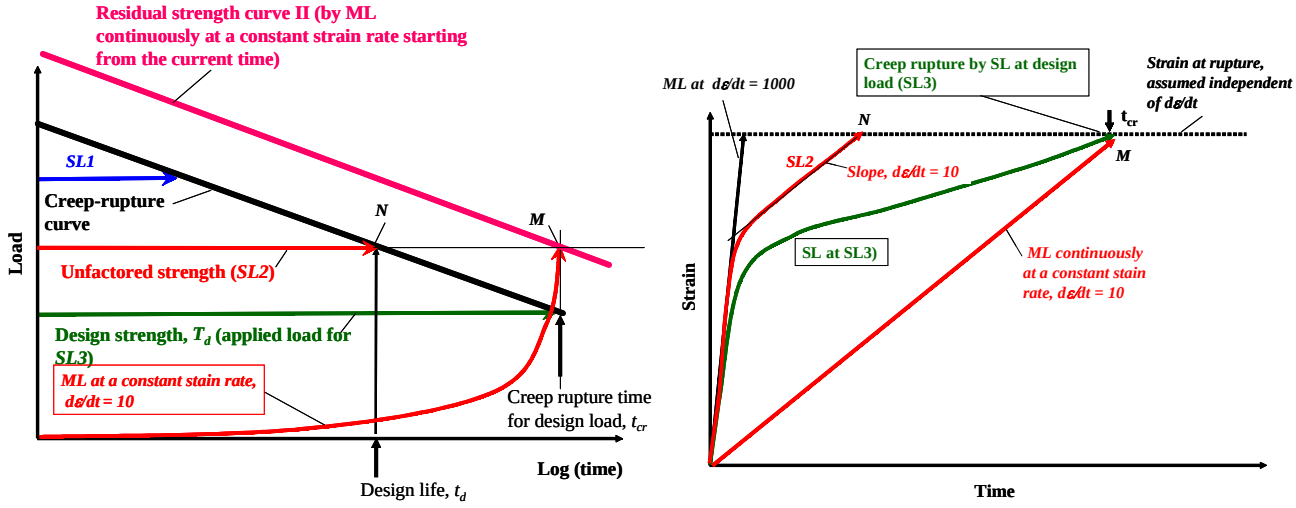

Fig. 2-9 Difference between conventional creep-rupture curve and residual strength curve II.

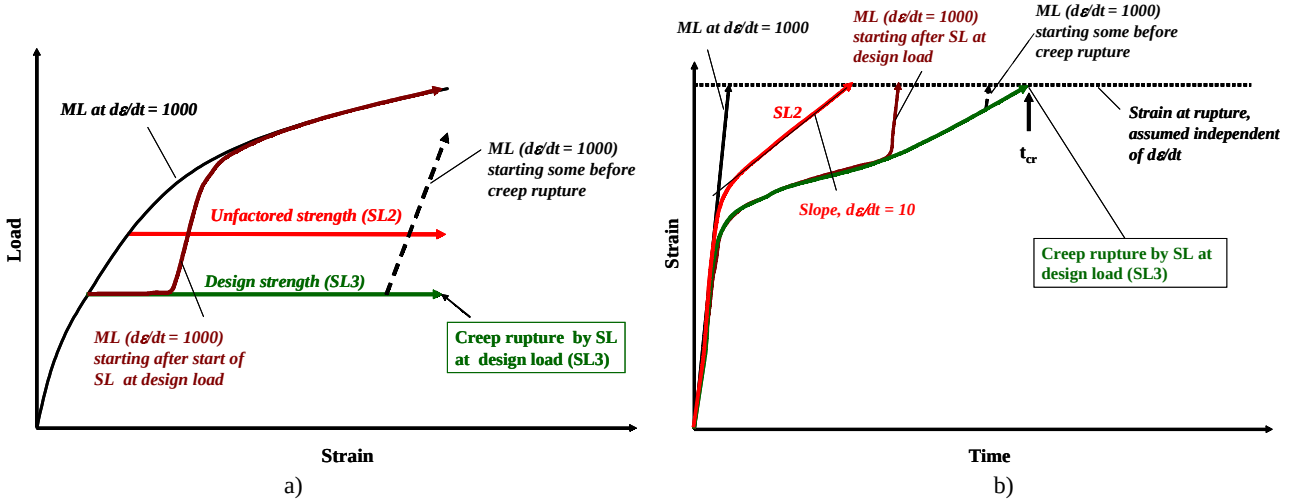

Fig. 2-10 a) Load-strain relations of geosynthetic reinforcement to obtain conventional creep rupture curve and residual strengths *III*.; b) difference between strain histories for conventional creep-rupture curve and residual strength curve III.

The following notions are important:

1. Residual strength curve II should be located below residual strength curve I for rupture time longer than some value, after which the difference in the strength between residual strength curves I and II increases with an increase in the time where the residual strength is to be obtained.
2. Residual strength curve II should be located above the conventional creep rupture curve.

The second point can be explained as follows:

a) In **Fig. 2-9a**, suppose that, in continuous ML at a constant strain rate = 10 starting from the current time, rupture takes place when the load is equal to SL2 at point denoted by the letter *M*. On the other hand, in sustained loading test SL2 (at the load equal to the unfactored load), creep rupture takes place at the end of the design life, t_d (point *N*). Then, the time at point M, t_{cr}, should be much longer than the time t_d.

b) The strain rate at rupture in sustained loading test SL3 (at the load equal to the design strength) should be much smaller than the strain rate = 10, **Fig. 2-9b**. Therefore, the rupture strength from ML continuously at a constant strain rate = 10 should be larger than the design strength.

These two features result from such properties of geosynthetic that the load–strain relation (including the rupture strength) is controlled by strain rate (more rigorously by irreversible strain rate; i.e., the isotach viscosity). These two features were also observed with sedimentary soft rock in drained triaxial compression (Hayano et al., 2001).

The use of residual strength curve II would however be too conservative with prototype GRS structures, because such continuing slow ML (such as the one at a strain rate = 10 or 1, Fig. 2-9) is not likely in typical field cases.

Residual strength curve III: With typical prototype GRS structures, the reinforcement is continuously subjected to non-zero tensile load during a service period. Suppose that, after some period of sustained loading at constant load equal to the design strength (SL3), the reinforcement is subjected to fast ML at a strain rate equal to 1,000 (as seismic loading), which is substantially higher than the value at the

end of sustained loading SL3, as illustrated in **Figs. 2-10a** and **b**. Then, the rupture strength that is substantially higher than the value estimated based on the conventional creep rupture curve is obtained. By repeating such tests as above starting after different periods of sustained loading, we obtain residual strength curve III, as illustrated in **Fig. 2-11**.

As shown in **Fig. 2-12**, residual strength III is the same with residual strength I for the same strain rate at rupture (i.e., 1,000 in this illustration) except for some period close to the rupture time for sustained loading at the design strength, t_{cr}. This is because residual strength III should become the same as the design strength when ML starts at $t = t_{cr}$ (i.e., when creep rupture is about to take place during sustained loading at the design strength). It is not certain how the horizontal portion is connected to the creep rupture point at $t = t_{cr}$. It is possible that the rupture strength when ML starts immediately before the creep rupture is smaller than the value when ML starts well before (**Fig. 2-13**). Then, residual strength curve III is curved at places close to the creep rupture point. The residual strength curve inferred based on the similar concept as above, having a more conservative shape, is shown in **Fig. 2-14**.

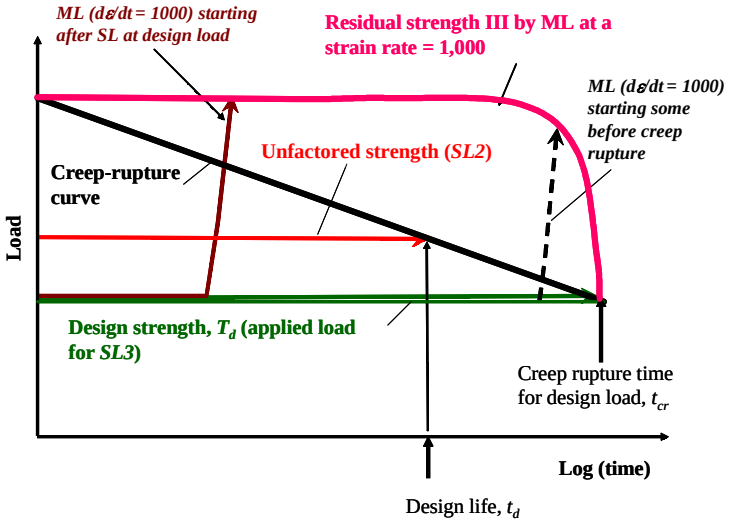

Fig. 2-11 Conventional creep rupture curve and residual strength curve III.

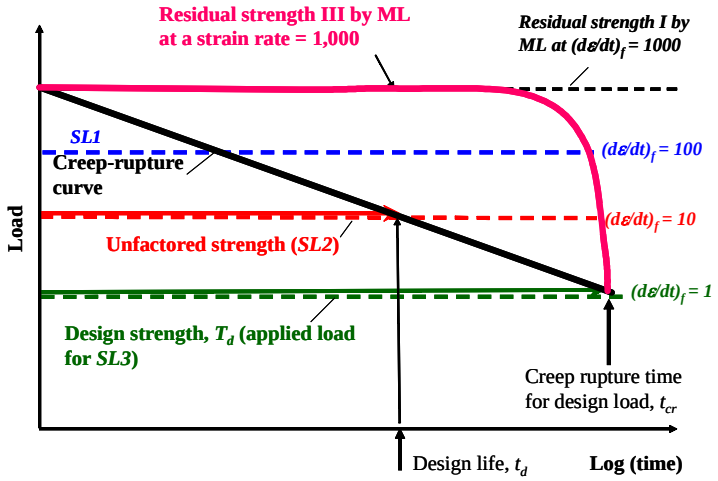

Fig. 2-12 Conventional creep rupture curve and residual strength curves I & III.

Then, it is seen that rupture strength curve III depends on the strain rate at rupture and also on the sustained load before the start of ML towards rupture, as illustrated in **Fig. 2-15**. Residual strength I is equivalent to residual strength III in the case with zero sustained loads before the start of "ML at a prescribed strain rate toward rupture".

In the seismic design code for GRS retaining walls for railway in Japan (RTRI, 2000) and segmental retaining wall in the North America (NCMA, 1998), the creep reduction factor is not applied but residual strength curve III is used. On the other hand, in many other codes, the seismic design strength is determined fully based on, or partially considering, the conventional creep rupture curve. Therefore, the rupture strength available for a given seismic load is grossly underestimated. That is, the margin for the rupture strength at the design life when the design load is determined fully based on the creep rupture curve while using a safety factor could be very large (**Fig. 2-16**).

Time history of tensile force in the reinforcement arranged in the backfill: Creep deformation and creep rupture of geosynthetic reinforcement results from its viscous properties. Therefore, if the tensile strain imposed to the reinforcement arranged in the backfill is kept constant under vertical sustained loading conditions, the tensile force activated in the geosynthetic reinforcement decreases with time due to the phenomenon of load relaxation. Then, due to a decrease in the lateral constraint to the backfill by the reinforcement, the lateral strain of the backfill somehow increases. Moreover, the backfill has also viscous properties. Therefore, as the creep deformation phenomenon, the lateral tensile strain in the backfill tends to increase with time when subjected to constant sustained vertical loading while it

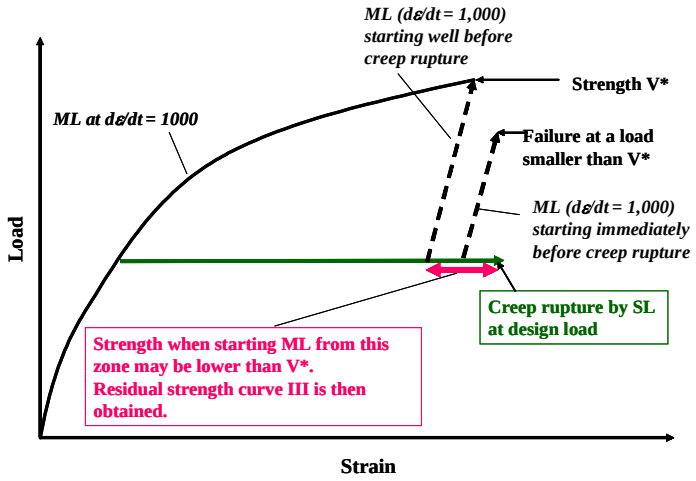

Fig. 2-13 Effects of the time of the start of ML on the residual strength III

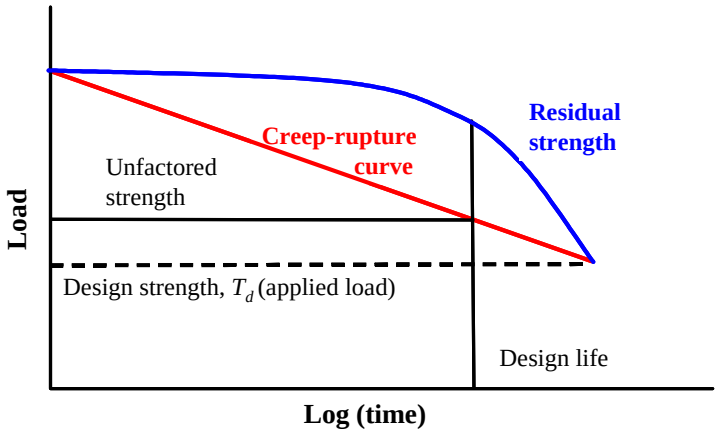

Figure 2-14 Schematic diagram showing the reduction in strength with time of a geosynthetic under a sustained design load. The unfactored strength is reduced by a safety factor to give the design load; the residual strength at the design life is now much greater than anticipated (Greenwood et al., 2001).

tends to decrease due to the lateral confining pressure provided by tensile force in the reinforcement. It is shown in Chapter 7 that the tensile force in the geogrid arranged in Toyoura sand in plane strain compression decreased with time during a sustained loading of the reinforced specimen at a stress state not close to ultimate failure. It is highly possible with ordinary GRS retaining walls having a sufficiently high safety factor against ultimate failure that the tensile force activated in the geosynthetic reinforcement arranged in the backfill having viscous properties decreases with time under ordinary static loading conditions. That is, the viscous properties of polymer geosynthetic help in decreasing the possibility of creep rupture. This situation is illustrated in **Figs. 2-17 a** through **d**. A decrease in the reinforcement force with time leads to a substantial increase in the time to creep rupture and some increase in the margin for rupture strength for fast loading starting at the design life (Fig. 2-17). The data of full-scale structures showing the above are reported by Tatsuoka et al. (2001). More detailed analysis of this issue is given in Chapter 7.

3 ISOCHRONOUS THEORY

3.1 *Introduction*

When based on the conventional creep rupture curve, the design rupture strength decreases with an increase in the design life. One of the serious misunderstandings about the creep reduction factor resulting from the above is that the rupture strength under the same loading condition (i.e., at the same strain rate) decreases with time. This misunderstanding is seemingly linked to the isochronous theory, which states that the current stress is a function of the instantaneous strain and the time that has elapsed since the start of loading. Then, the development of creep deformation by sustained loading at a fixed load/stress state means a degrading phenomenon; i.e., creep is treated just as the process of time elapsing. In actuality, however, the strength of geosynthetic reinforcement does not decrease because of creep deformation at pre-peak intermediate loading stages (as shown in Chapter 5). That is, the creep phenomenon should be understood as the process where the irreversible strain rate decreases with time.

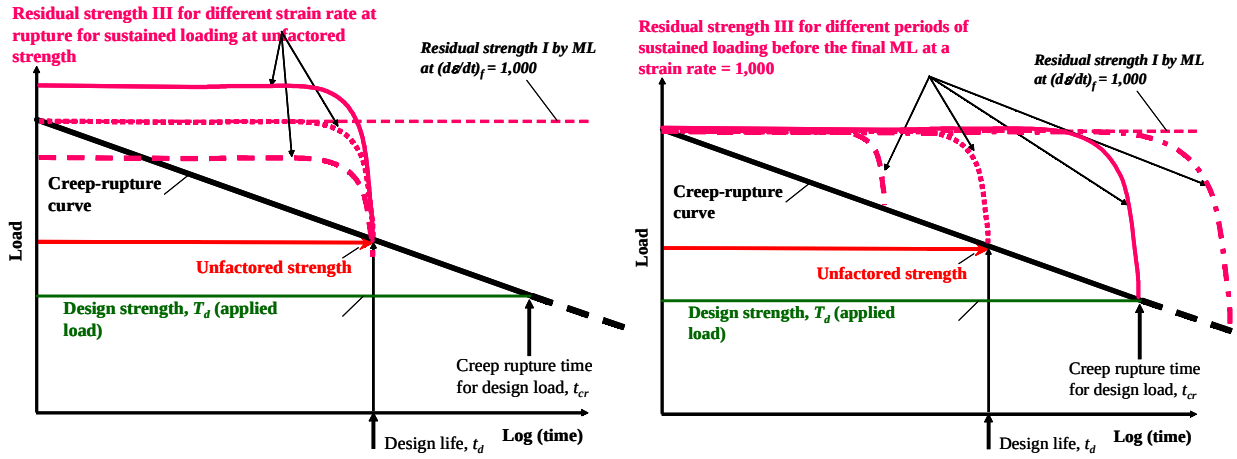

Fig. 2-15 a) Effects of strain rate at rupture residual strength curve III; and b) Effects of sustained load on residual strength curve III.

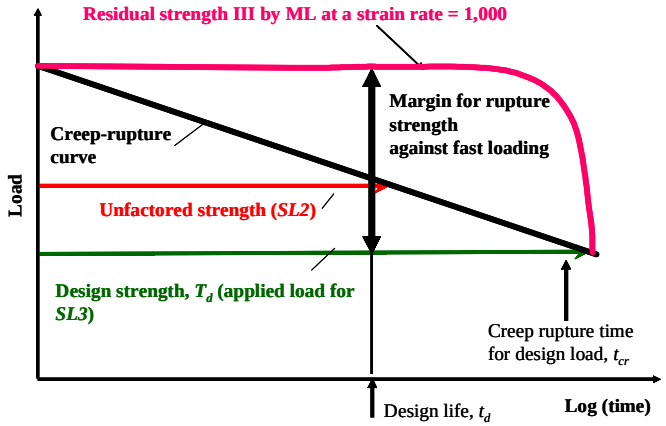

Fig. 2-16 Difference in the design strength based on the creep-rupture strength and likely actual strength during seismic loading.

3.2 *Response of geosynthetic to different loading histories*

It is very difficult, if not possible, to find that the isochronous theory is not relevant only based on results from a set of ML tests performed at different constant strain rates, as illustrated in **Fig. 3-1**. In this figure, the tensile load–tensile strain curves from three continuous ML tests performed at three different constant strain rates, denoted as 1, 10, and 100, are depicted. From these test results, it is possible to construct contours of time (i.e., isochrones). Then, it appears that the stress-strain curve is controlled by time.

On the other hand, a relevant examination of the isochronous theory (and others) becomes possible by analysing load-strain behaviour during and after sustained loading tests performed under otherwise ML at a constant strain rate, together with those from a set of continuous ML tests at different constant strain rates. That is, referring to **Fig. 3-2**, suppose that the following three tests are performed:

Test 1: ML continues at a high strain rate (= 100) towards ultimate failure.

Test 2: ML continues at a high strain rate until point ***a*** (at a relatively high load level), from which sustained loading starts and ends at point ***b***. From point ***b***, ML restarts at the original high strain rate (= 100) and continues towards rupture.

Test 3: The loading history is similar as that of test 2, except that the load level during sustained loading is very low.

Then, the question is whether the strength obtained from tests 2 and 3 is the same as the one obtained from test 1. According to the isochronous concept, the following trends of behaviour should be obtained (**Fig. 3-3a**):

1. For the same elapsed time ($t = t_4$) since the start of loading, the same stress-strain state (point ***b***) is reached by:
   a) fast loading until point ***a***, followed by sustained loading until point ***b*** (test 2);
   b) fast loading until point ***c***, followed by load relaxation until point ***b***; and
   c) continuous slow ML until point ***b***.
2. When fast ML at a strain rate equal to 100 restarts from point ***b*** in test 2, the load-strain relation should be located below the isochrone for $t = t_4$, passing through point ***b***, since we cannot go back to the past. Then, the strength obtained from test 2 becomes smaller than the one obtained by test 1 (i.e., continuous fast ML until failure), while the reduction in the strength by sustained loading increase with an increase in the period of sustained loading ***a-b***. This indeed implies that creep is a degrading phenomenon.
3. The same amount of strength reduction by sustained loading is observed in test 3 despite that the sustained load at stage ***e-f*** is quite low (**Fig. 3-3b**). **Fig. 3-3c** compares the load-strain curves from tests 2 and 3.

It is seen from the above that the isochronous concept cannot predict realistically the load-strain-time behaviour of geosynthetic subjected to general loading histories that would be encountered in full-scale structures.

On the other hand, **Fig. 3-4a** illustrates the actual behaviour of geosynthetic reinforcement, as presented in Chapter 5, that is:

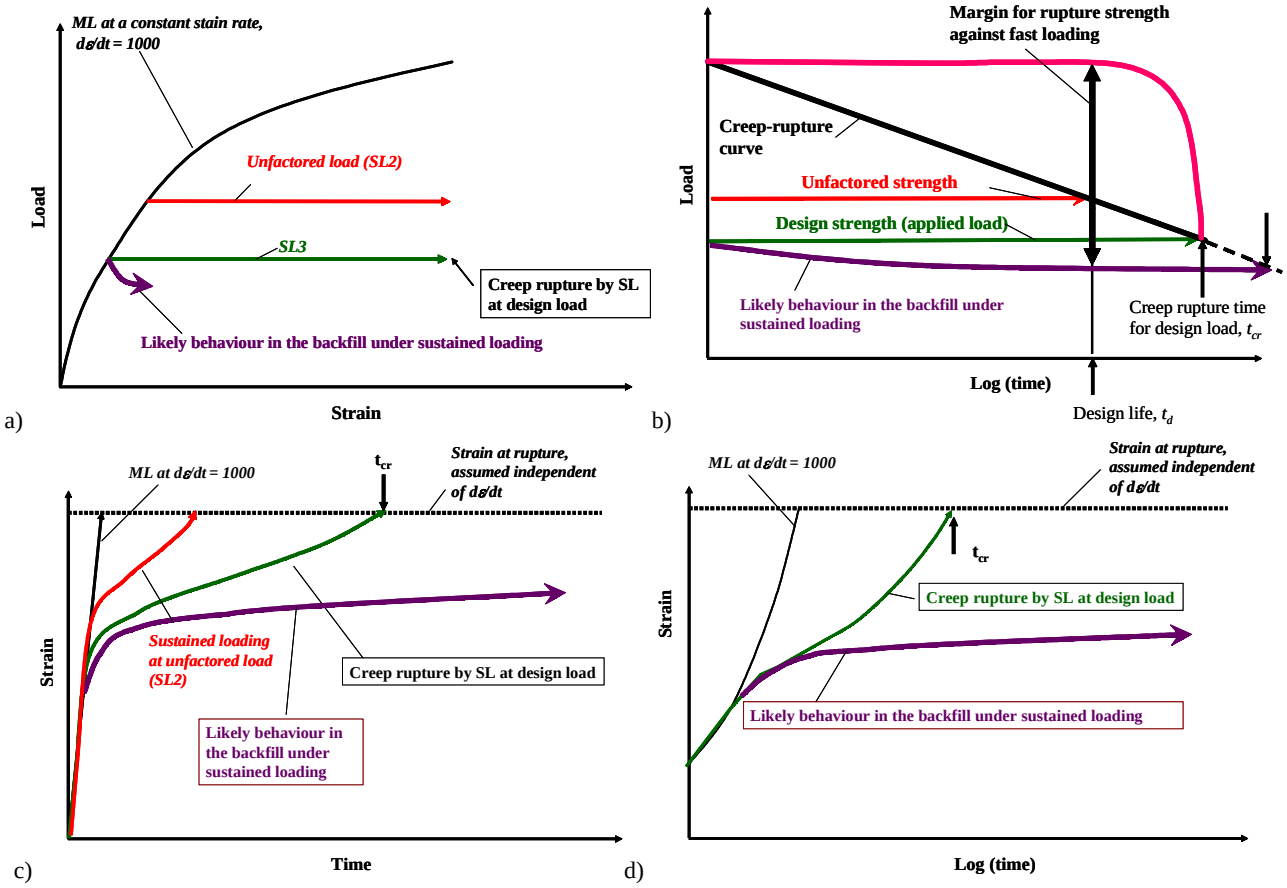

Fig. 2-17 Likely behaviour of geosynthetic reinforced arranged in sand.

1. For the same elapsed time since the start of loading, the same stress-strain state (point ***b***) is <u>not</u> reached by the following three loading histories:
   a) fast loading until point ***a,*** followed by sustained loading (until point ***b'***) (test 2);
   b) fast loading until point ***c***, followed by load relaxation (until point ***b***); and
   c) continuous slow ML (until point ***b''***).
2. When fast ML at a strain rate equal to 100 restarts at point ***b'*** in test 2, the load-strain relation first shows very stiff behaviour, close to the elastic one. In the case of isotach viscosity (explained in Chapter 6), the stiff behaviour continues until reaching the relation from test 1 (i.e., continuous fast ML until rupture). Then, the load-strain relation in test 2 rejoins the latter. Therefore, the rupture strength obtained from test 2 is essentially the same as the one from test 1, irrespective of the period of sustained loading ***a-b'***. This implies that creep is <u>not</u> a degrading phenomenon.
3. The same behaviour after sustained loading is observed in test 3 (**Fig. 3-4b**). **Fig. 3-4c** compares the load - strain curves from tests 2 and 3.

In summary, creep is not a degrading phenomenon and the isochronous concept is unable to predict in the relevant way the time-dependent deformation of geosynthetic subjected to general arbitrary loading histories, while it is a quite misleading concept. Typical experimental data supporting this argument is presented in Chapter 5.

4 NEW DESIGN METHOD (TENTATIVELY PROPOSED)

4.1 *Introduction*

It is to be noted that the backfill has also noticeable viscous properties as geosynthetic reinforcement, which means that:

1) it is not possible to accurately predict the long-term residual deformation of a given GRS structure by taking into account only the viscous properties of a given geosynthetic reinforcement; and
2) the design procedure to take into account the effects of viscous properties on the strength of geosynthetic reinforcement should be consistent with that of backfill.

With respect to the first item, for example, the long-term residual settlement of the backfill may not be prevented even when using a great amount of reinforcement having an extremely high stiffness.

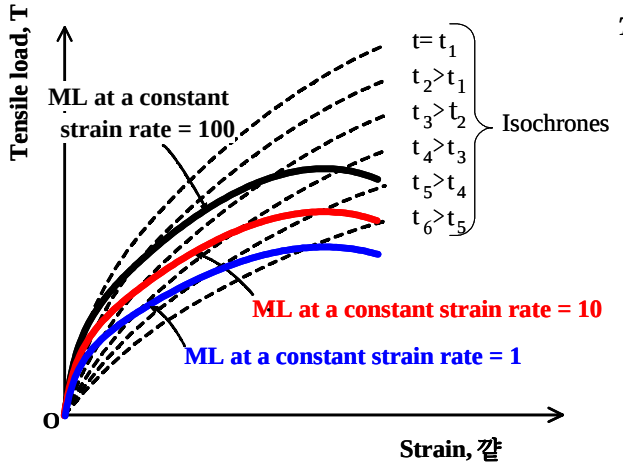

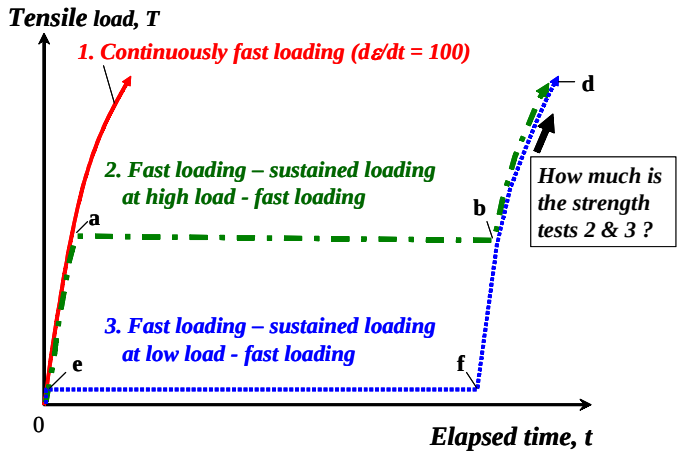

Fig. 3-1 (left) Interpretation of results from ML at different constant strain rates by Isochronous concept.
Fig. 3-2 (right) Loading histories relevant to examine the relevance of Isochronous concept.

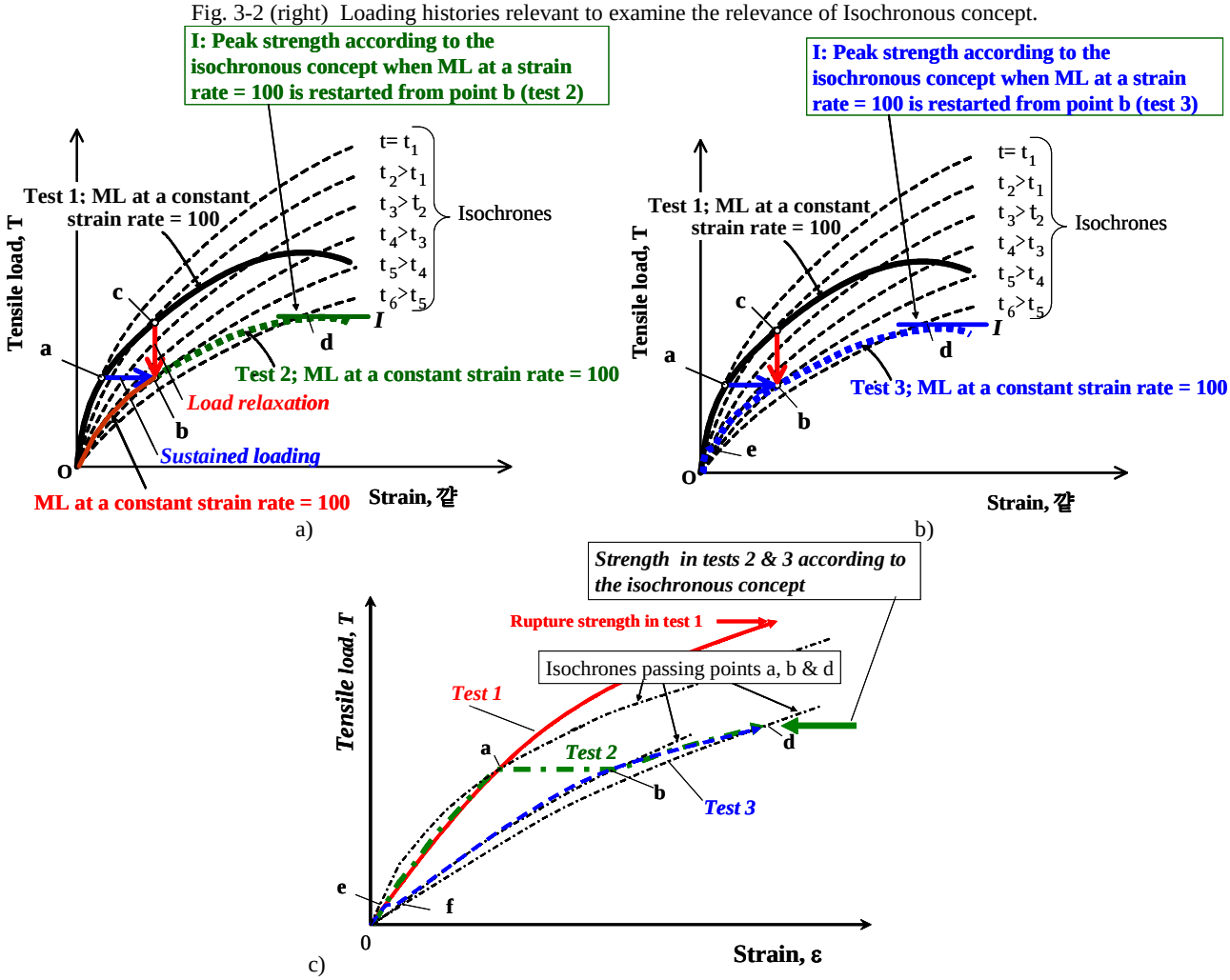

Fig. 3-3 Response of geosynthetic reinforcement according to Isochronous concept to different loading histories presented in Fig. 3-2.

4.2 *Creep rupture potential does not necessarily means the need for a creep reduction factor*

The fact that geosynthetic reinforcement has a creep rupture potential does not necessarily mean that the design strength should be always determined based on the creep rupture curve.

First of all, the time-dependent change in the tensile force in the reinforcement arranged in the backfill is controlled by at least the following three factors, referring to **Fig. 4-1**:

1) An increase imposed by an increase in the viscous lateral tensile strain of backfill taking place by static load (weight of structure and external dead load) applied vertically on the reinforced soil.
2) A decrease associated with the development of viscous lateral compressive strain of backfill caused by confining pressure due to rein-

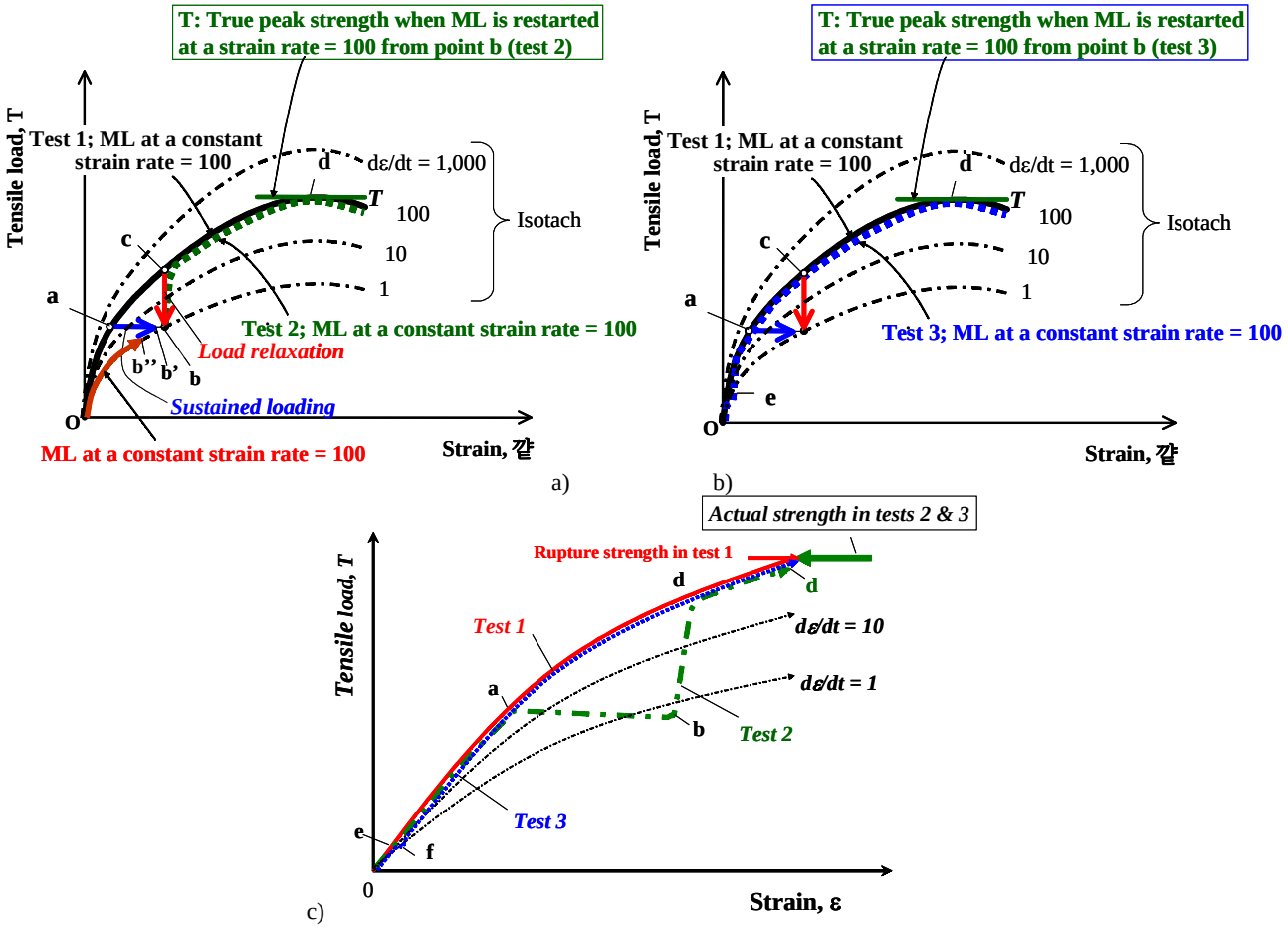

Fig. 3-4 Actual response of geosynthetic reinforcement to different loading histories presented in Fig. 3-2.

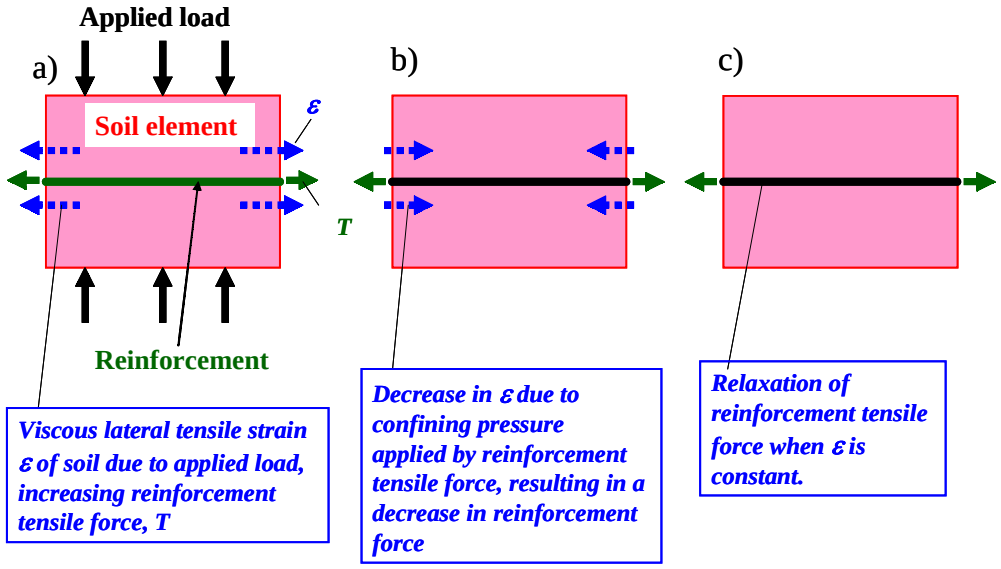

Fig. 4-1 Schematic diagram showing interaction between viscous behaviours of sand and geogrid.

forcement tensile force.

3) A decrease due to viscous deformation of geosynthetic reinforcement that would take place even under constant strain (i.e., the phenomenon of load relaxation).

With respect to the first factor, generally, the creep deformation rate of GRS structure increases with a decrease in the global structural safety factor against ultimate failure, $(F_s)_{overall.static}$, which results in relatively high creep deformation rates of both geosynthetic reinforcement and backfill, which are interacting with each other. In case the effects of the first factor become stronger than those of the second and third factors, the tensile force in the reinforcement could be maintained constant or even increase with time. In this case, the potential for creep rupture in a long run of geosynthetic reinforcement becomes higher. This case is possible only when the failure of geosynthetic-reinforced soil (GRS) structure is imminent. This case is exceptional with ordinal GRS structures, because of the following two factors:

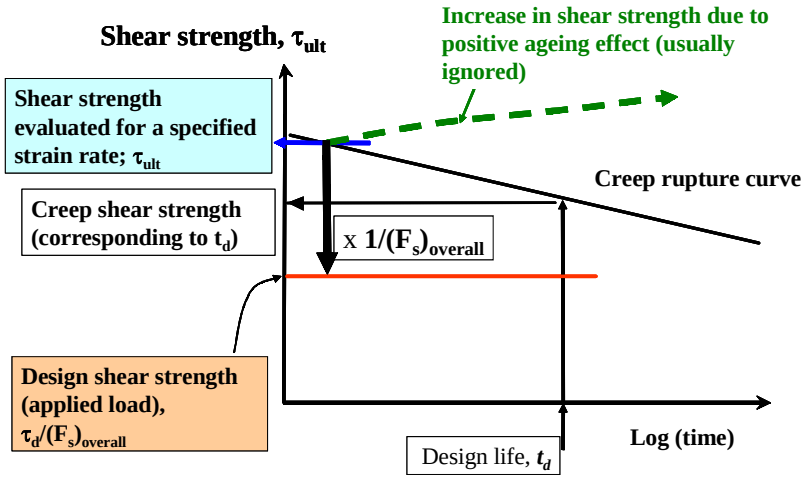

Fig. 4-2 Design shear strength of soil in usual cases

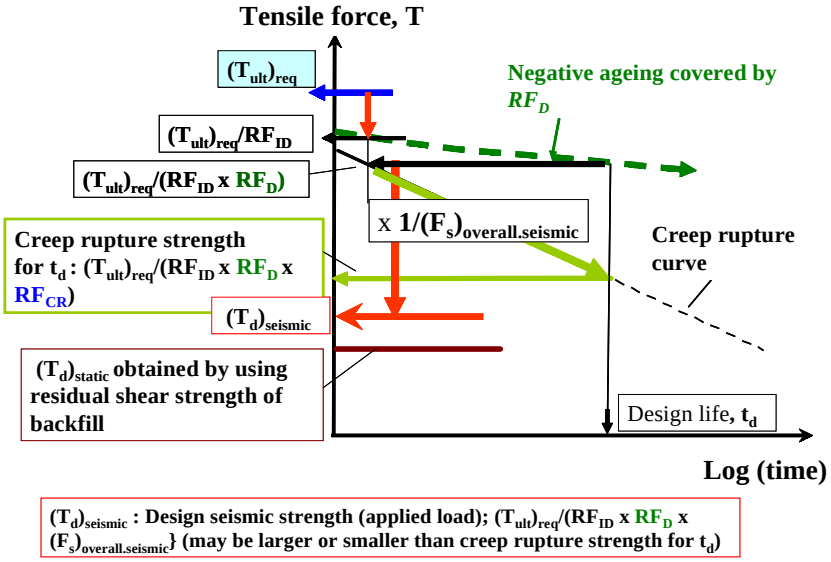

Fig. 4-3 Case where the design strength is not controlled by creep rupture strength.

1) When relevant aseismic design is performed, it is usual that the structural safety factor against static working load of a given GRS structure is higher than sufficient, which results in a creep deformation rate under static working conditions that is very low, or negligible, while much lower than anticipated when following the current design procedure.
2) The design shear strength of backfill used in the current design procedure for GRS structures is usually similar to the residual strength, or intentionally determined to be so. This design procedure results into a gloss underestimation of the structural safety factor against ultimate failure and a gloss over-estimation of creep deformation rate of GRS structure, in particular when the backfill is constructed by using a high quality soil and is well-compacted.

A number of reports found in the literature (e.g., Simac et al., 1990, Carrubba et al., 1999, Allen et al., 1992 Allen and Bathurst, 2002, Abu-Hejleh et al., 2002) showed that measured strains in the geosynthetic reinforcement of prototype GRS structures are much smaller than anticipated. Moreover, any case of failure of prototype GRS structures because of creep rupture of geosynthetic reinforcement has not been reported (e.g., Simac et al. 1990; and as far as the authors know). These facts indicate that the above considerations are relevant.

Secondly, the shear strength of soil is also rate-dependent. For example, Ladd (1986) reported that "the undrained shear strength, c_u, of saturated soft clay decreases with a decrease in the strain rate; in consolidated undrained triaxial compression on isotropically consolidated specimens of OCR = 1 clay, the parameter $\lambda = (\Delta c_u / c_{u0}) / \Delta \log \dot{\varepsilon}$, where c_{u0} is the reference strength, say at $\dot{\varepsilon}$ = 1 % per hour, is equal to 0.1 ± 0.05 for the failure to time ranging from several minutes to several hours." That is, soil could exhibit creep failure when subjected to sustained loading at a load higher than some limit. Despite the above, creep failure of soil is considered in geotechnical design only when it could be the major cause for the failure of soil mass (e.g., slope, ground and soil structure) that would take place during service time. The most typical one is the prediction of the time to failure of a natural slope continuously exhibiting noticeable creep deformation. In most other cases, although soil has a potential for creep failure, the design shear strength is determined without reducing because of a potential for creep failure, but it is defined implicitly or explicitly for a certain strain rate at failure. For example, Ladd (1986) reported that "*general experience based on a balance between practicality and limited case histories has resulted in the following practice by many leading research-consulting laboratories: axial strain rate of 0.5 % - 1 % per hour for triaxial tests; and shear strain rate of 5 % per hour for direct simple shear tests*" as the typical values to be used to determine the design shear strength of soft clay in the stability analysis of soft clay deposits. As illustrated in **Fig. 4-2**, this design procedure is relevant when the design shear strength of soil (equal to the an-

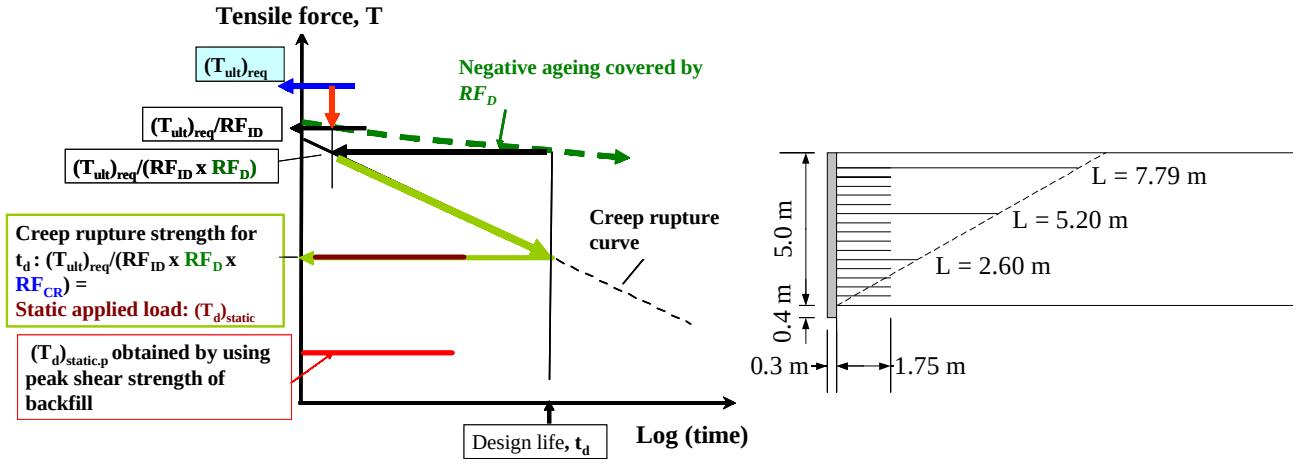

Fig. 4-4 (left) Case where the design strength is controlled by creep rupture strength.
Fig. 4-5 (right) Working example to demonstrate the difference between conventional and newly proposed methods.

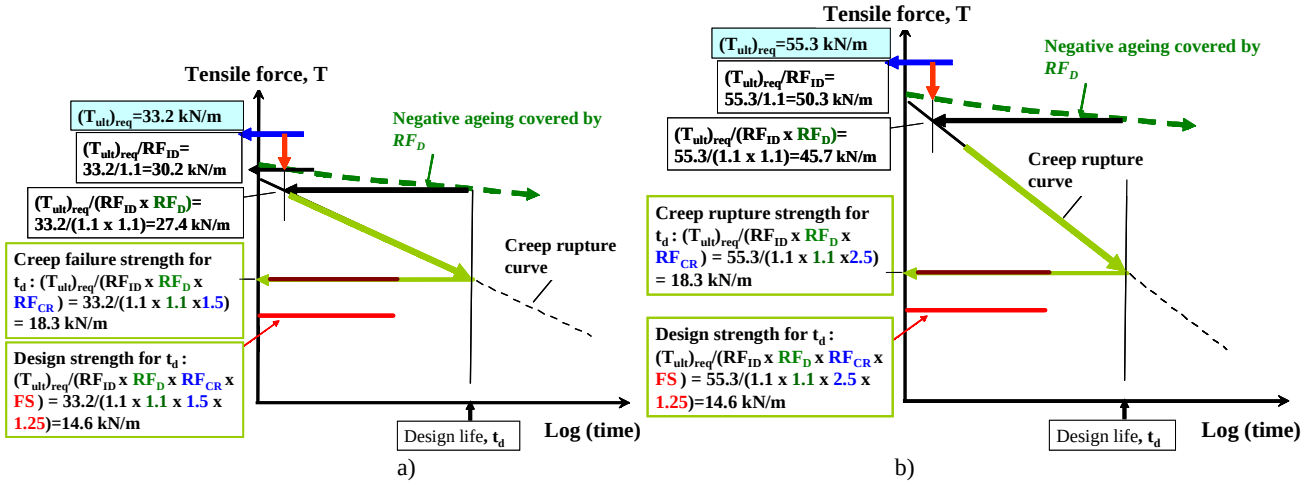

Fig. 4-6 Conventional design method; a)RF_{CR} = 1.5; and b) RF_{CR} = 2.5

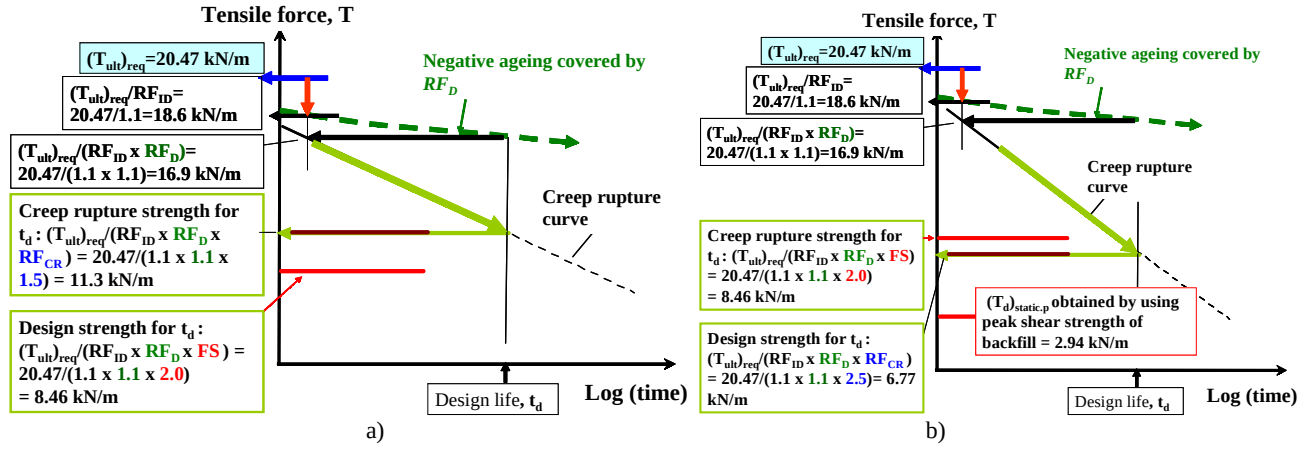

Fig. 4-7 Newly proposed design method; a)RF_{CR} = 1.5; and b) RF_{CR} = 2.5

anticipated working shear stress) obtained by dividing the shear strength evaluated for a specified strain rate with an overall safety factor is well below the creep failure shear strength evaluated for a given design life. It is usual the case with ordinary permanent geotechnical structures allowing a limited amount of residual deformation. It is particularly the case when relevant seismic design is employed. On the other hand, the shear strength of soil may increase with time due to positive ageing effects. This factor is ignored in usual geotechnical design. The authors cannot see any reason for not using the above-mentioned design procedure in the design of GRS structures.

4.3 *Tentatively proposed method*

The following method could be tentatively proposed as a new procedure to obtain the design strength of geosynthetic reinforcement to be used in the limit equilibrium-based stability analysis of GRS structure, which is consistent with the ordinary geotechnical design procedure:

1) The ultimate strength, T_{ult}, for a given design strain rate of a given type of geosynthetic reinforcement is obtained by performing relevant tensile loading tests. If this value is obtained for another strain rate (1 %/min., 20 %/min or so), the measured value is corrected to the specified design strain rate at failure. The design strain rate at failure under static and dynamic loading conditions should be different (i.e., the design strain rate under static loading conditions should be lower).
2) The design strength, $(T_d)_{static}$, that is necessary to obtain a safety factor equal to unity against given design static loading conditions is obtained by relevant stability analysis (e.g., the two-wedge method). The design seismic strength, $(T_d)_{seismic}$, is obtained in a similar way for given design seismic loading conditions. For conservatism, the residual angle of friction is used as the design shear strength of backfill for static loading conditions For seismic loading conditions, the peak shear strength is used to obtain the locations of critical failure planes, while the limit equilibrium along the thus-obtained critical failure planes is evaluated by using the residual shear strength. This method was proposed by Tatsuoka et al. (1998) for the seismic design of GRS retaining walls referring to the seismic design method for retaining walls with unreinforced backfill (Koseki et al., 1997). Leshchinsky (2001) detailed this method for the stability analysis of reinforced soil structures.
3) The value of T_{ult} (the ultimate, or yield, tensile strength based on minimum average role value) is determined to satisfy:

$$(T_d)_{static} = (T_{ult})_{static} / \{RF_D \cdot RF_{ID} \cdot (F_s)_{overall.static}\}; \quad \text{(4-1); and}$$

$$(T_d)_{seismic} = (T_{ult})_{seismic} / \{RF_D \cdot RF_{ID} \cdot (F_s)_{overall.seismic}\} \quad \text{(4-2)}$$

Then, the larger value of $(T_{ult})_{static}$ and $(T_{ult})_{seismic}$ (defined for the same strain rate) should be chosen, which is denoted as $(T_{ult})_{req}$ (defined for a certain strain rate). The value of $(T_{ult})_{req}$ tends to be determined by the value of $(T_{ult})_{seismic}$ to a more extent with an increase in the design seismic load.

4) Confirm whether the creep rupture strength, $(T_{ult})_{req} / \{RF_{CR} \cdot RF_D \cdot RF_{ID}\}$, is equal to, or larger than, the design static load, $(T_{ult})_{static}$.
   a) In highly seismic zones, the above requirement is usually satisfied. **Fig. 4-3** illustrates this case.
   b) If not, the value of $(T_{ult})_{req}$ should be increased to satisfy:

$$(T_{ult})_{req} = (T_d)_{static} \cdot \{RF_{CR} \cdot RF_D \cdot RF_{ID}\}. \quad \text{(4-3)}$$

Fig. 4-4 illustrates this case. That is, when the creep failure is considered, the overall safety factor is not introduced considering that an ample margin for failure is already considered by using the residual shear strength of backfill and by ignoring possible effects of load relaxation on the geogrid tensile force. However, it should be confirmed that the static design load obtained by using the residual shear strength of backfill, $(T_d)_{static}$ (= $(T_{ult})_{req} / \{RF_{CR} \cdot RF_D \cdot RF_{ID}\}$), be well larger, say by a factor of 1.5, than the static design load obtained by using the peak shear strength of backfill, $(T_d)_{static.p}$. This condition could be easily satisfied when relevant soil type is used while the backfill is well compacted as with ordinary GRS retaining walls.

4.4 *Working examples*

To demonstrate the difference between the conventional design procedure based the creep rupture curve and the newly proposed method for a given type of geosynthetic reinforcement, the following working example was prepared.

Basic design conditions: The wall has a height of 5 m (**Fig. 4-5**). The backfill has a unit weight of 18 kN/m^3 and an angle of internal friction equal to ϕ_{res} = 30 degrees (residual) and ϕ_{peak} = 45 degrees (peak) with zero cohesion intersect. The surcharge is equal to 10 kN/m^2. The ultimate rupture strength of geogrid that can satisfy the specified design conditions are obtained below by following the conventional design procedure and the newly proposed procedure (refer to **Fig. 4-6**).

(A) Conventional design procedure (**Figs. 4-6a** & **b**):

1) *Calculation of design strength of geogrid, T_d*:
   a) The design strength, $(T_d)_{static}$, required to obtain the safety factor for sliding failure under static loading conditions equal to unity is 8.46 kN/m. This design strength was obtained by the two-wedge method using ϕ_{res} = 30 degrees.
   b) The design strength, $(T_d)_{seismic}$, required to obtain the safety factor for sliding failure under seismic loading conditions equal to unity is 19.5 kN/m. This design strength was obtained by the two-wedge method using a horizontal seismic coefficient equal to 0.2 and the residual shear strength of the backfill, ϕ_{res} = 30 degrees.
2) Calculation of required ultimate strength of geogrid, $(T_{ult})_{req}$:
   a) The design strength, $(T_d)_{seismic}$, which is much larger than $(T_d)_{static}$, is converted to the value at the strain rate at which the value of $(T_{ult})_{req}$ is defined for static loading conditions as follows:
      (1) It is assumed that the strain rate at rupture under seismic loading conditions is 100 %/min, which is faster by a factor of 1,000 than the value under static loading conditions (= 0.1 %/min).
      (2) Based on the results presented in Fig. 5.4, it is assumed that the strength of PET geogrid decreases by a factor of 0.75 with a decrease in the strain rate at rupture by a factor of 1,000.
      (3) The converted design strength for seismic loading conditions, $(T_d)_{seismic.c}$, becomes 19.5 $\times$0.75 = 14.63 kN/m.
   b) The required ultimate strength, $(T_{ult})_{req}$, defined at a strain rate equal to 0.1 %/min. is obtained:
      (1) It is assumed that $RF_D = RF_{ID}$ = 1.1.
      (2) The following values of T_{ult} are then obtained using different safety factors for static and seismic loading conditions:
      $(T_{ult})_{static}$ = $(T_d)_{static} \times RF_{CR} \times RF_D \times RF_{ID} \times (F_S)_{static}$ = 8.46$\times RF_{CR} \times$1.1$\times$1.1$\times$2.0 = 20.47 kN/m$\times RF_{CR}$

$(T_{ult})_{seismic.c} = (T_d)_{seismic} \times RF_{CR} \times RF_D \times RF_{ID} \times (F_S)_{seismic} = 14.63 \times RF_{CR} \times 1.1 \times 1.1 \times 1.25$
$= 22.13$ kN/m$\times RF_{CR}$

Then, $(T_{ult})_{req} = 22.13$ kN/m$\times RF_{CR}$ is obtained.

(3) The creep reduction factor, RF_{CR}, is assumed to be 1.5 and 2.5, equally for static and seismic loading conditions.

Then, $(T_{ult})_{req} = 22.13$ kN/m$\times RF_{CR}$ (= 1.5 and 2.5)= 33.2 and 55.3 kN/m are obtained.

(B) Newly proposed design procedure (**Figs. 4-7a** & **b**):

1) *Calculation of design strength of geogrid, T_d*:

a) The design strength, $(T_d)_{static}$, is 8.46 kN/m. This design strength was obtained by the two-wedge method using $\phi_{res} = 30$ degrees. The design strength, $(T_d)_{static.p}$, obtained by using the peak strength, $\phi_{peak} = 45$ degrees, is equal to 2.94 kN/m.

b) The design strength, $(T_d)_{seismic}$, is 14.4 kN/m. This design strength was obtained by the two-wedge method using a horizontal seismic coefficient equal to 0.2 and the residual and peak shear strengths of the backfill, $\phi_{res} = 30$ degrees and $\phi_{peak} = 45$ degrees.

2) Calculation of required ultimate strength of geogrid, $(T_{ult})_{req}$:

a) The design strength, $(T_d)_{seismic}$, is converted to the value at the strain rate at which the value of $(T_{ult})_{req}$ is defined for static loading conditions as $(T_d)_{seismic.c} = 0.75 \times 14.4 = 10.8$ kN/m.

b) The required ultimate strength, $(T_{ult})_{req}$, defined at a strain rate equal to 0.1 %/min. is obtained:

(1) It is assumed that $RF_D = RF_{ID} = 1.1$.

(2) The following values of T_{ult} are then obtained:

$(T_{ult})_{static} = (T_d)_{static} \times RF_D \times RF_{ID} \times (F_S)_{static} = 8.46 \times 1.1 \times 1.1 \times 2.0 = 20.47$ kN/m

$(T_{ult})_{seismic.c} = (T_d)_{seismic.c} \times RF_D \times RF_{ID} \times (F_S)_{seismic} = 10.8 \times 1.1 \times 1.1 \times 1.25 = 16.34$ kN/m

Then, $(T_{ult})_{req} = 20.47$ kN/m is obtained.

3) *Comparison of static design strength with creep rupture strength*:

a) The creep reduction factor, RF_{CR}, is assumed to be 1.5 and 2.5.

b) When $RF_{CR} = 1.5$, we obtain: $(T_{ult})_{req}/(RF_{CR} \times RF_D \times RF_{ID}) = 20.47/(1.5 \times 1.1 \times 1.1) = 11.28$ kN/m, which is larger than $(T_d)_{static}$. Therefore, $(T_{ult})_{req} = 20.47$ kN/m, obtained not using the creep reduction factor, is the strength to be prepared to satisfy the specified design conditions.

c) When $RF_{CR} = 2.5$, we obtain $(T_{ult})_{req}/(RF_{CR} \times RF_D \times RF_{ID}) = 20.47/(2.5 \times 1.1 \times 1.1) = 6.77$ kN/m, which is smaller than $(T_d)_{static}$. However, the creep rupture strength, $(T_{ult})_{req} / (RF_{CR} \times RF_D \times RF_{ID}) = 6.77$ kN/m is still larger than 1.5 times "$(T_d)_{static.p}$ obtained by using the peak strength, $\phi_{peak} = 45$ degrees (= 2.94 kN/m)". Therefore, $(T_{ult})_{req} = 20.47$ kN/m is the strength to be prepared to satisfy the specified design conditions.

For $RF_{CR} = 1.5$, the required ultimate strength, $(T_{ult})_{req}$, obtained by following the newly proposed procedure, equal to 20.47 kN/m, which is much smaller than the value obtained by following the current design procedure, equal to 33.2 kN/m. For $RF_{CR} = 2.5$, the difference increases, $(T_{ult})_{req} = 20.47$ kN/m by the newly proposed procedure versus 55.3 kN/m by the conventional procedure.

5 EXPERIMENTAL DATA

5.1 *Introduction*

As discussed in Chapter 3, to examine the relevance of a given theoretical concept or design procedure with respect to time effects (i.e., viscous and ageing effects), special material tests employing various loading histories should be performed. This is particularly because typical loading histories with GRS structures are neither simple ML at a constant strain rate nor sustained loading at a constant load. Despite the above, most of the previous tests reported in the literature are those performed using these two conventional loading histories. Described herein are experimental data from special tensile loading tests performed to evaluate the viscous properties of geosynthetic reinforcement under arbitrary loading histories.

5.2 *Test materials and testing method*

Hirakawa et al. (2002, 2004) and Kongkitkul et al. (2003, 2004) performed a series of tensile loading tests using fresh (unused) samples of six different types of polymer geogrid reinforcement, which are typical of those widely used in Japan, and aged samples of one type of geogrid. Among them, only reinforcement 7 is a geocomposite, consisting of a planar needle-punched non-woven geotextile made of continuous polypropylene (PP) filament and high-strength polyester (PET) yarns in the longitudinal direction. The centre-to-centre spacing between two parallel adjacent yarns is about 5 mm. The non-woven geotextile sheet, having a negligible tensile strength when compared with the one of the PET yarns, is designed only for a drainage function. The following loading histories were employed:

a) Continuous ML was performed at different constant strain rates toward rupture.
b) The strain rate was changed stepwise several times and sustained loading and load relaxation tests were performed during otherwise ML at a constant strain continuing towards rupture.
c) Sustained loading tests were performed during otherwise primary ML continuing towards rupture as well as during a cycle of unloading and reloading with a large load amplitude.

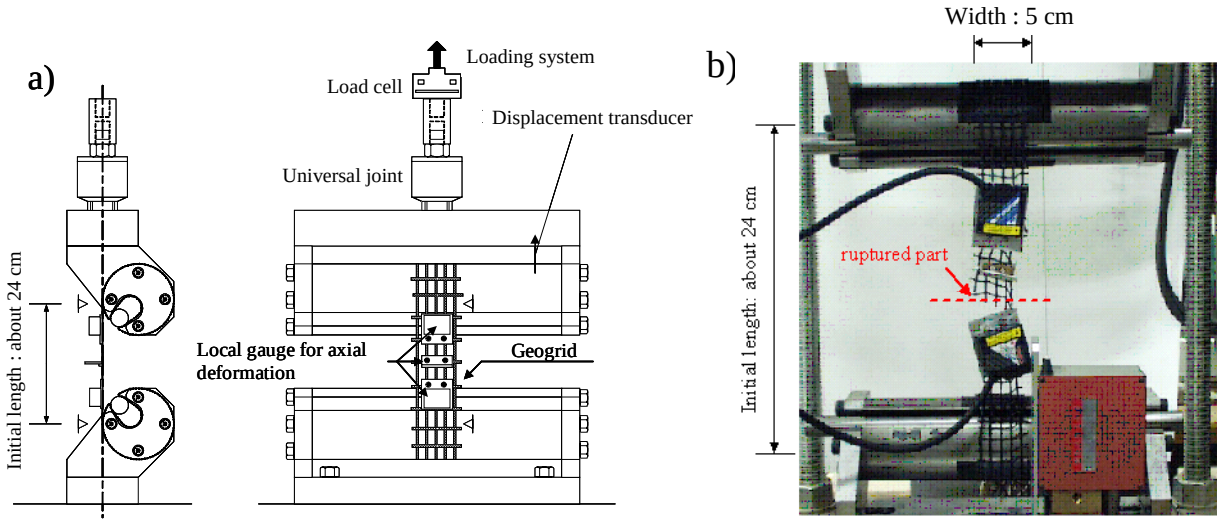

Fig. 5-1 a) Gripping device A with a specimen; and b) a typical ruptured specimen, reinforcement 1 (PET).

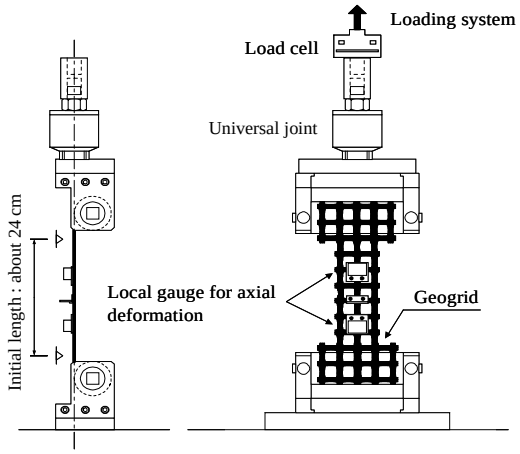

Fig. 5-2 Gripping device B for reinforcement 4 (Aramid).

d) A number of small-amplitude unload/reload cycles with a double amplitude strain on the order of 0.05 % were applied during otherwise ML continuing towards rupture.

The following two types of gripping devices, ***A*** and ***B*** shown in **Figs. 5-1a** and **5-2**, were used:

Gripping device ***A***, which consists of a steel cylinder, on which a specimen is wrapped-around, and a small-diameter steel bar, by which the end of the specimen is fixed to a groove made in the steel cylinder. This device was used in the tests on reinforcements 1, 2, 3, 5, 6 and 7. **Fig. 5-1b** shows a typical ruptured specimen of reinforcement 1.

Gripping device ***B***, which was used only for reinforcement 4 (Aramid geogrid).

The initial total specimen length was about 90 cm, while the initial ungripped length was 24 cm. An initial gauge length at the central part of specimen for local axial strain measurements by using a pair of laser displacement sensors was 5 or 6 cm.

A tensile loading apparatus having a capacity of 50 kN was used. It consists of a precise gear system with practically zero backlash upon load reversal and a computer-controlled servo-motor (Tatsuoka et al., 1994; Santucci de Magistris et al., 1999). By controlling the displacement to an accuracy of less than 1 μm in an automated way, it is possible: a) to smoothly switch between displacement and load control loading phases and between a sustained loading or load relaxation stage and a constant strain rate loading or unloading phase; b) to change the strain rate stepwise or gradually by a factor of up to 3,000; and c) to apply very small amplitude unload/reload cycles to evaluate the elastic properties of test material during otherwise constant strain rate loading.

Table 5-1 lists the geosynthetic reinforcement types, produced in Japan, of which the strength and deformation characteristics obtained from tensile loading tests using loading histories a) through d) listed above are reported in this paper. Shinoda and Bathurst (2004a, b) performed similar tests on Polypropylene (PP), Polyester (PET) and High-Density Polyethylene (HDPE) geogrids produced in the North America using loading histories a) and b) listed above.

5.3 *Test results and discussions*

Fig. 5-3 show the relationships between the tensile load per unit width (T) and the local axial tensile strain (ε) obtained from ML tests performed on reinforcement 1 (PET geogrid) at constant strain rates that were different by a factor of up to 2,000. **Fig. 5-4a** shows a summary of the tensile strengths from tests having different loading histories, as explained above, of reinforcement 1 (PET geogrid) including those described in Fig. 5-3, plotted against the logarithm of the strain rate at rupture (n.b., the actual strain rate at rupture was somehow different from the respective nominal value). The nominal strength provided by the respective manufacture is also presented. **Fig. 5-4b**

Table 5-1 Geosynthetic reinforcements tested by Hirakawa et al. (2002, 2004) and Kongkitkul et al. (2003, 2004).

No.	1)	2)	3)	4)
Fibre material	Polyester	Polyarylate	Polyvinyl alcohol	Aramid
Abbreviated name	PET	-	PVA	-
Coating material	Polyvinyl chloride resin	Polyvinyl chloride resin	Polyvinyl chloride resin	High density polyethylene
Vmax, nominal (kN/m) at strain rate	39.2* 1 %/min	88.0 1 %/min	60.8* 1 %/min	56.0* 1 %/min
Creep reduction factor used in current routine design**	-	0.60	0.65	0.60
Specimen conditions	Virgin	Virgin	Virgin	Virgin
Specimen width/strands	5 cm/ 5 strands	5 cm/ 3 strands	5 cm/ 3 strands	5 cm/ 3 strands
Loading histories***	a, b, c and d	a, b, c and d	a, b, c and d	b

5)	6)	7)
High density polyethylene	Polyvinyl alcohol	Polyester yarn
HDPE	PVA	PET yarn
High density polyethylene	High density polyethylene	-
50.0* 1 %/min	59.0* 1 %/min	157.0* 1 %/min
0.60	0.60	-
Virgin	Aged for 8 years	Virgin
8 cm/ 3 strands	5 cm/ 3 strands	1.5 cm/ 1 strand
b	a and b	a, b, c and d

Note: * and ** are the values provided by the manufacturers.

*** a) continuous monotonic loading (ML); b) ML with step changes in the strain rate; sustained loading and stress relaxation; c) ML with sustained loading during primary loading and global unloading and reloading; and d) a number of unloading/reloading cycles with a small amplitude.

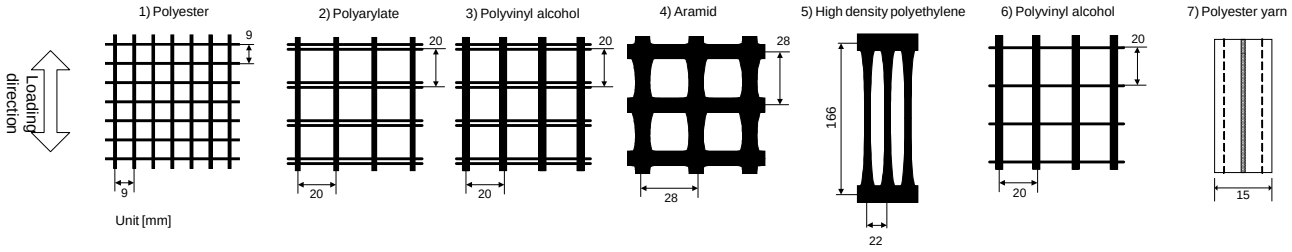

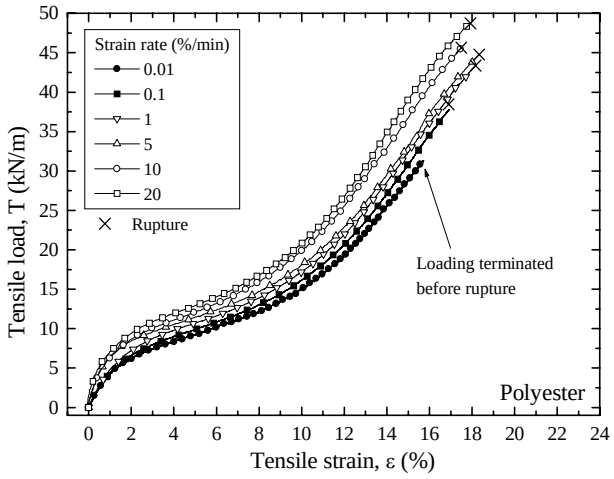

Fig. 5-3 Dependency of tensile load-elongation property on strain rate, reinforcement 1 (PET geogrid) (Hirakawa et al., 2004).

shows a summary for reinforcement 2 (Polyarylate geogrid), similar to Fig. 5-4a. **Fig. 5-5** shows test results of HDPE geogrid similar to Fig.5-3, while **Fig. 5-6** shows the results of HDPE, PET and PP geogrids similar to Figs. 5-4a and b (Shinoda and Bathurst, 2004a, b). The following trends of behaviour may be seen from these figures:

1) The rupture strength increases proportionally with the logarithm of the strain rate at rupture, showing that the rupture strength is basically a unique function of the strain rate at rupture, independent of loading history before rupture while not controlled by the elapsed time from the start of loading until rupture. Christensen (1981) also showed the above. It is obvious that the isochronous concept cannot explain this fact.
2) For reinforcement type 1 (PET geogrid; Fig. 5-3) and reinforcement 2 (Polyarylate geogrid), the strain at rupture is practically independent of strain rate, despite that the strain at rupture somehow scatters among different specimens. On the other hand, with HDPE geogrid (Fig. 5-5), the strain at failure increases with a decrease in the strain rate. A reason (or reasons) for these different trends of behaviour is (are) not known.

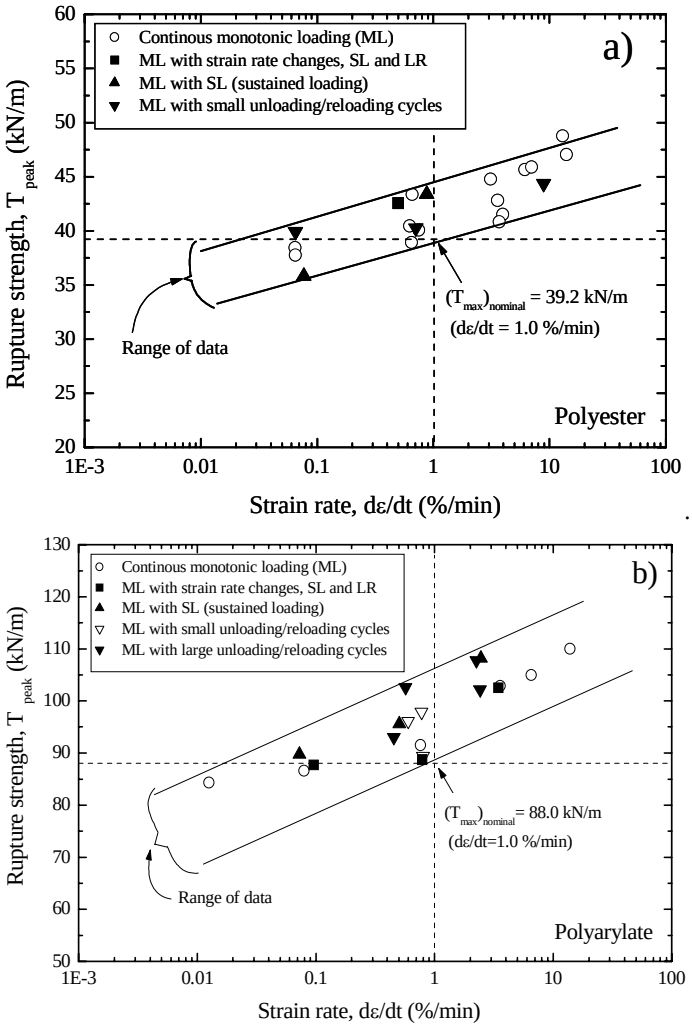

Fig. 5-4 Dependency of rupture strength on the strain rate at rupture: a) reinforcement 1 (PET); and b) reinforcement 2 (Polyarylate geogrid) (ML: monotonic loading; SL: sustained loading; and LR: load relaxation) (Hirakawa et al., 2004).

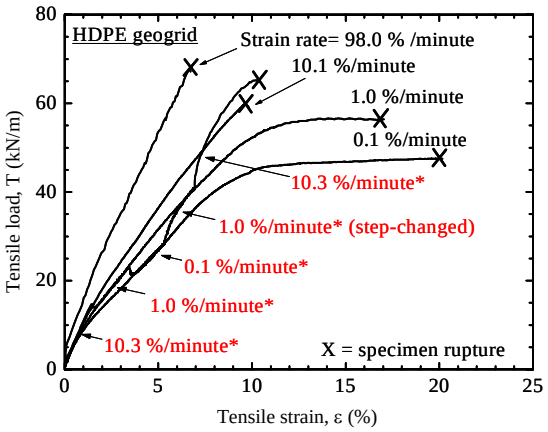

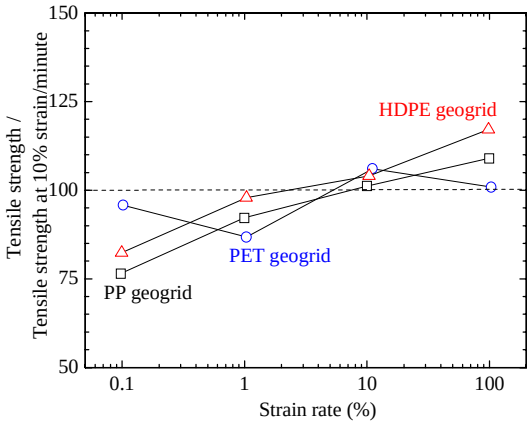

Fig. 5-5 (left) Dependency of tensile load-elongation property on strain rate, HDPE geogrid produced in the North America (Shinoda and Bathurst, 2004a, b).

Fig. 5-6 (right) Dependency of rupture strength on the strain rate at rupture, PET, HDPE and PP geogrids produced in the North America (Shinoda and Bathurst, 2004a, b).

Figs. 5-7a and **5-8** show the results for reinforcements 1 and 3 (PET and PVA geogrids) from the tests using loading history b). A similar result for the HDPE geogrid produced in the North America is presented in Fig. 5-5. The following trends of behaviour may be noted from these figures.

1) Noticeable creep deformation and load relaxation took place.
2) All the tested geosynthetic reinforcements showed a very high stiffness, close to the elastic one:
   a) when ML was restarted at a constant strain rate following a sustained loading or load relaxation stage; and

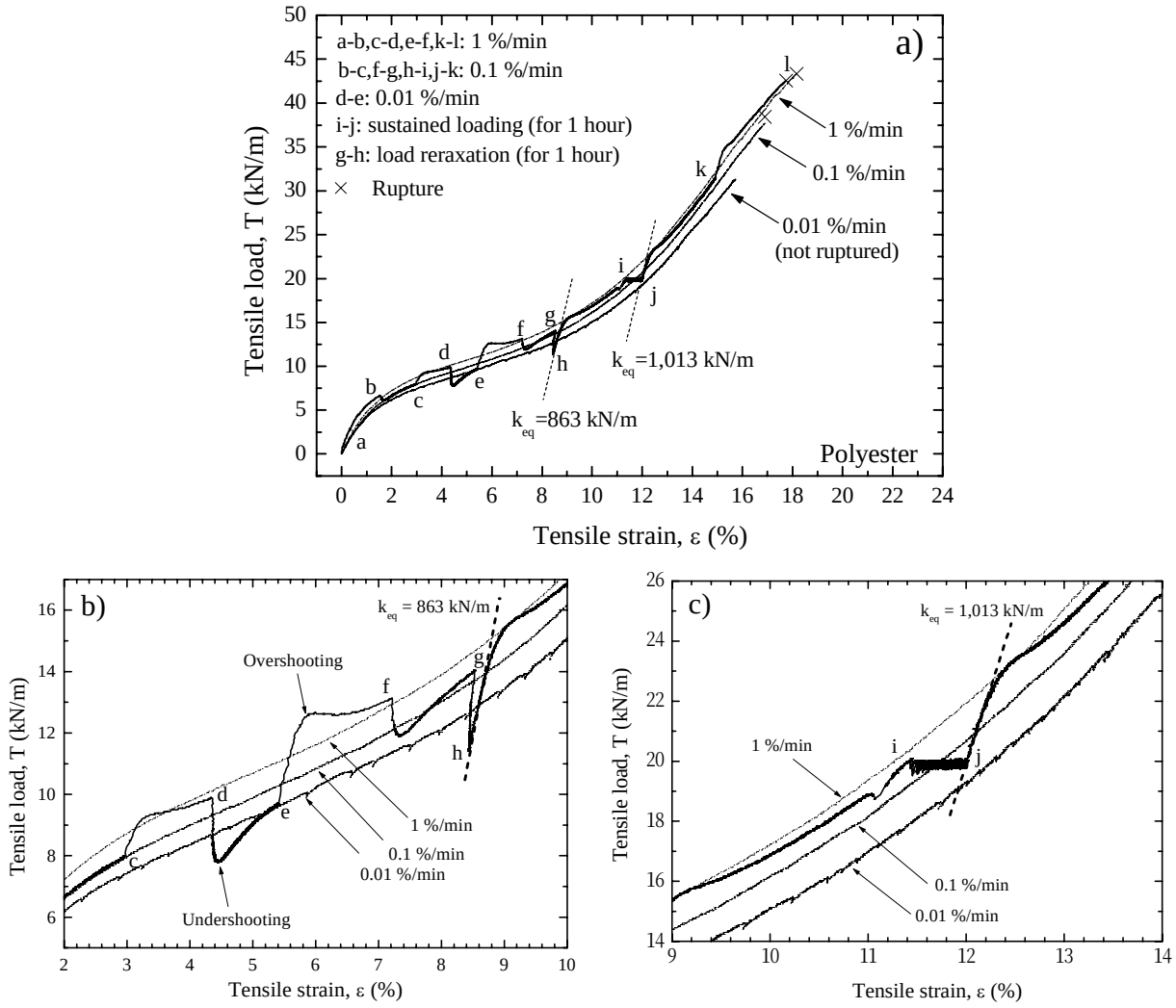

Fig. 5-7 Loading rate effects on load-strain relation, reinforcement 1 (PET geogrid) (Hirakawa et al., 2004).

b) immediately after a step increase in the strain rate during otherwise ML at a constant strain rate.

Then, the load-strain relationship exhibited clear yielding and subsequently the load-strain curve tended to rejoin the original one that would be obtained by continuous ML at the constant strain rate after the restart of loading.

3) The behaviour that was opposite to the above took place immediately after the strain rate was decreased stepwise during otherwise ML at a constant strain rate.

4) With reinforcement 1 (PET geogrid, Fig. 5-7), the load-strain curve exhibited a noticeable load over-shooting when the strain rate was increased stepwise during otherwise ML or when ML at a constant strain rate was restarted after a sustained loading or load relaxation stage. A phenomenon of load-undershooting took place upon a step decrease in the strain rate during otherwise ML at a constant strain rate. With the other types of reinforcement (Figs. 5-5 and 5-8), such load-overshooting and undershooting did not take place while the load is always a unique function of instantaneous strain and strain rate (or more rigorously a function of instantaneous irreversible strain and its rate). This viscous property has been called the isotach viscosity (Tatsuoka et al., 2001), as explained in Chapter 6. It is not known to the authors why only reinforcement 1 (PET geogrid), among those listed in Table 5-1 and the HDPE produced in the North America, exhibits this trend of behaviour. This fact is taken into account when developing the constitutive models later in this paper.

The trend of viscous properties (i.e., the isotach viscosity) can also be seen from results from tensile loading tests on reinforcement 5 (HDPE geogrid) in which the load rate was controlled using a loading history similar to c) (**Figs. 5-9a** and **b**; Kongkitkul et al., 2004). Note that reinforcement 5 (HDPE geogrid) exhibited the largest creep strain rate among those referred to in this report. It is obvious that these trends of behaviour described above are attributed to the viscous properties of the tested reinforcements and therefore cannot be properly described by the isochronous concept.

Hirakawa et al. (2004) also performed similar tensile loading tests on aged reinforcement 6 (PVA geogrid), which had been used to reinforce the backfill of well-graded gravel for three GRS bridge abutments supporting one of the busiest rapid transits in Tokyo (Seibu Railway) for about eight years (from 1993 to 2001) (Tatsuoka et al., 1997; **Figs. 5-10a** and **b**). A full-height RC rigid facing was cast-in-place directly on the face of GRS walls that had been constructed with a help of gravel-filled gabions placed on the shoulder of each soil layer and wrapped-around with the geogrid reinforcement. When the structures were demolished in 2001, a number of geogrid samples were retrieved from the inside of the structures. According to the manufacturer, the rupture strength obtained by tensile loading tests on

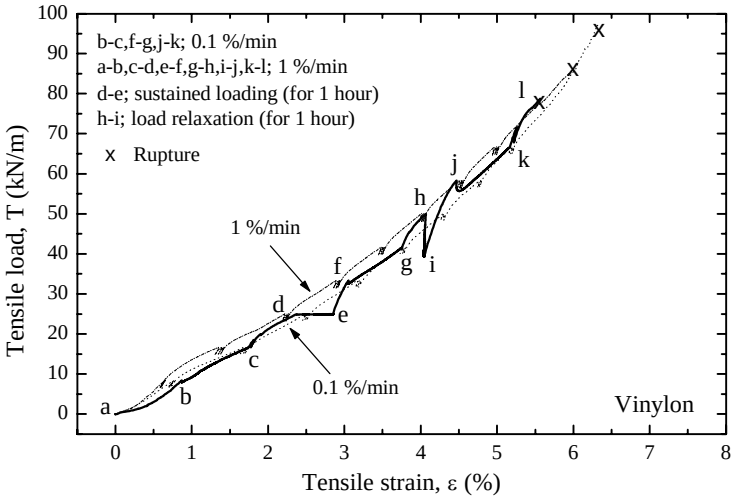

Fig. 5-8 Loading rate effects on the load-strain relations from load controlled tests: a) reinforcement 4 (HDPE geogrid); b) reinforcement 3 (PVA geogrid) (Kongkitkul et al., 2004).

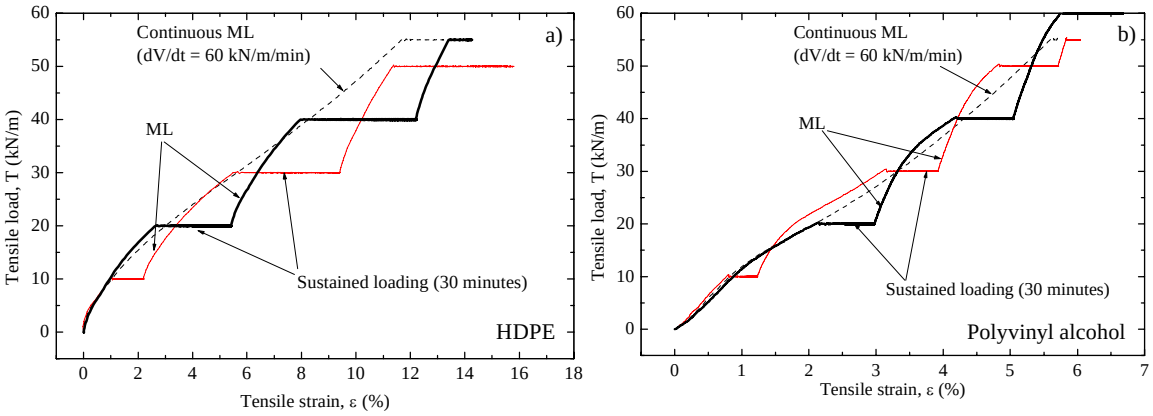

Fig. 5-9 Loading rate effects on the load-strain relations from load controlled tests: a) reinforcement 4 (HDPE geogrid); b) reinforcement 3 (PVA geogrid) (Kongkitkul et al., 2004).

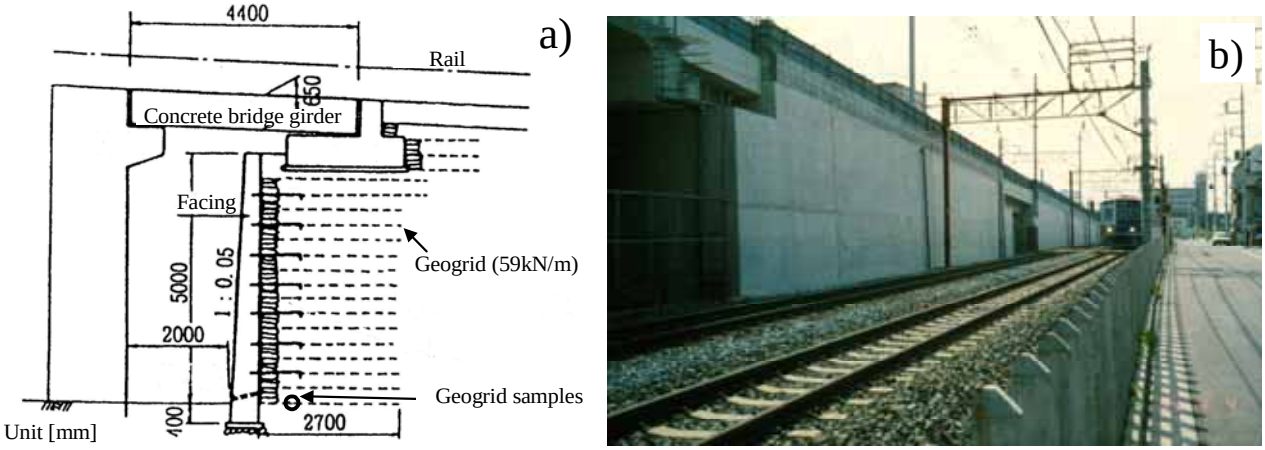

Fig. 5-10 a) Cross-section of one of the GRS bridge abutments; and b) GRS bridge abutments for Seibu Line, Tokyo (Tatsuoka et al., 1997).

fresh 20 cm-wide specimens at a strain rate of 1 %/min performed before the construction of the structures was 59.0 kN/m at a rupture strain of 10 %. Loading histories a) and b) were applied to this type of reinforcement.

Fig. 5-11 summaries the tensile strengths, plotted against the strain rate at rupture, of the aged samples of reinforcement 6 (PVA geogrid) together with the nominal strength of two fresh samples (a different lot from reinforcement 3). **Fig. 5-12** shows the results from a ML test using loading history b) and two continuous ML tests, all using aged samples of reinforcement 6. The following trends of behaviour may be seen from these figures:

1) Negative ageing effects on the pre-peak load-strain behaviour and peak strength of the tested aged sample of reinforcement 6 are insignificant, if any.

2) The peak strength of the aged samples is also a function of strain rate at rupture, independent of sustained loading and load relaxation histories applied at pre-peak intermediate stages.
3) The trend of viscous behaviour seen with the aged samples is essentially the same as the one of reinforcement 3 (i.e., fresh PVA geogrid: Fig. 5-8).

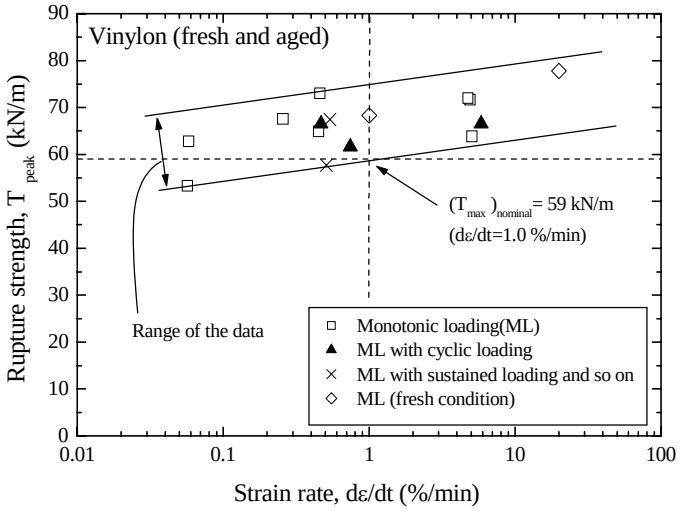

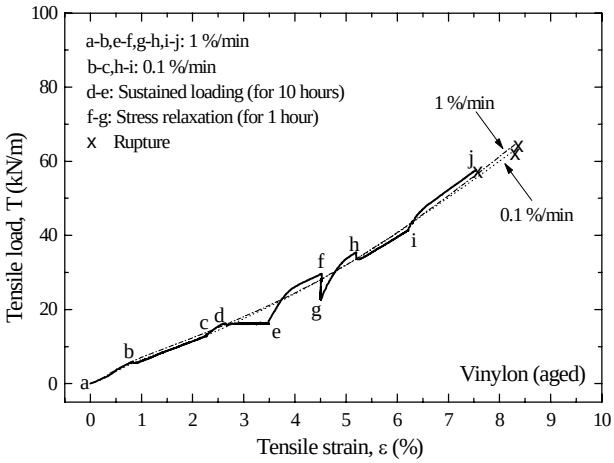

Fig. 5-11 (left) Dependency of rupture strength on strain rate, reinforcement 6 (aged PVA geogrid) and corresponding fresh samples (two data points) (Hirakawa et al., 2004).
Fig. 5-12 (right) Viscous effects on load-strain relation, reinforcement 6 (aged PVA geogrid) (Hirakawa et al., 2004).

5.4 *Quantification of viscous properties*

Fig. 5-13a summarises the ratios of "the jump in the tensile load per unit width, ΔT , taking place by a step change in the irreversible tensile strain rate (defined in **Fig. 5-13b**)" to "the tensile load, T, when the respective step change in the strain rate was made", obtained from the tests described in Figs. 5-7, 5-8 and 5-12 and other similar ones. The load ratios, $\Delta T / T$, are plotted against the logarithm of the ratio of the irreversible strain rates after and before the respective step change, $(\dot{\varepsilon}^{ir})_{after}$ and $(\dot{\varepsilon}^{ir})_{before}$. The following trends of behaviour may be seen from Fig. 5-13a:

1) For the respective reinforcement type, the ratio $\Delta T / T$ is essentially independent of the value of T, which means that the value of ΔT is always proportional to the instantaneous value of T.
2) The ratio $\Delta T / T$ increases in a broad sense linearly with an increase in the logarithm of the ratio of irreversible strain rates after and before a step change. This fact means that the viscous load component changes by changes in the strain rate in a non-linear manner, unlike the Newtonian viscosity.
3) The slope of respective linear relation represents the characteristics of viscous property. The slopes of the different types of reinforcement are not very different. The solid line represents the average relation.
4) More rigorously, the slope β depends on the geosynthetic reinforcement type, as listed in Fig. 5-13a.

The relationships presented in Fig. 5-13a correspond to those in Fig. 5-4. However, their rigorous relationship is somehow complicated. This is firstly because the strain at rupture scatters among different specimens tested at different strain rates of the same reinforcement type, resulting in a scatter in the viscous effects at rupture. Secondly, with reinforcement 1 (PET geogrid), the viscous effects decay with an increase in the irreversible strain as shown above.

In several previous studies found in the literature, continuous ML were performed at different strain rates on several different types of polymer geosynthetic reinforcement. The values of β were obtained assuming the isotach viscosity from the data found in the literature as listed in **Table 5-2**. In so doing, the load values for different strain rates at several same strains were read from the load-strain curves from ML tests at different strain rates. For the same material type, the β values from different researches are similar in a broad sense. In a rigorous sense, however, the values obtained by different researchers using different lots are noticeably different as typically shown in **Fig. 5-14**. Despite the above, in all the cases found in the literature, the quantification of the viscous properties in terms of β is relevant.

5.5 *Summary of Chapter 5*

The experimental results presented in this Chapter show the following:

1) With all the referred geogrid reinforcement types, the stiffness immediately after monotonic loading (ML) was restarted at a constant strain rate following a sustained loading stage was very high. After exhibiting clear yielding, with or without a noticeable overshooting in the load, the load-strain relation tended to rejoin the original one that would have been obtained by continuous ML without an interruption of sustained loading.
2) The ultimate strength of the reinforcement was essentially a unique function of strain rate at rupture, not affected by pre-peak loading histories including sustained loading and load relaxation stages.

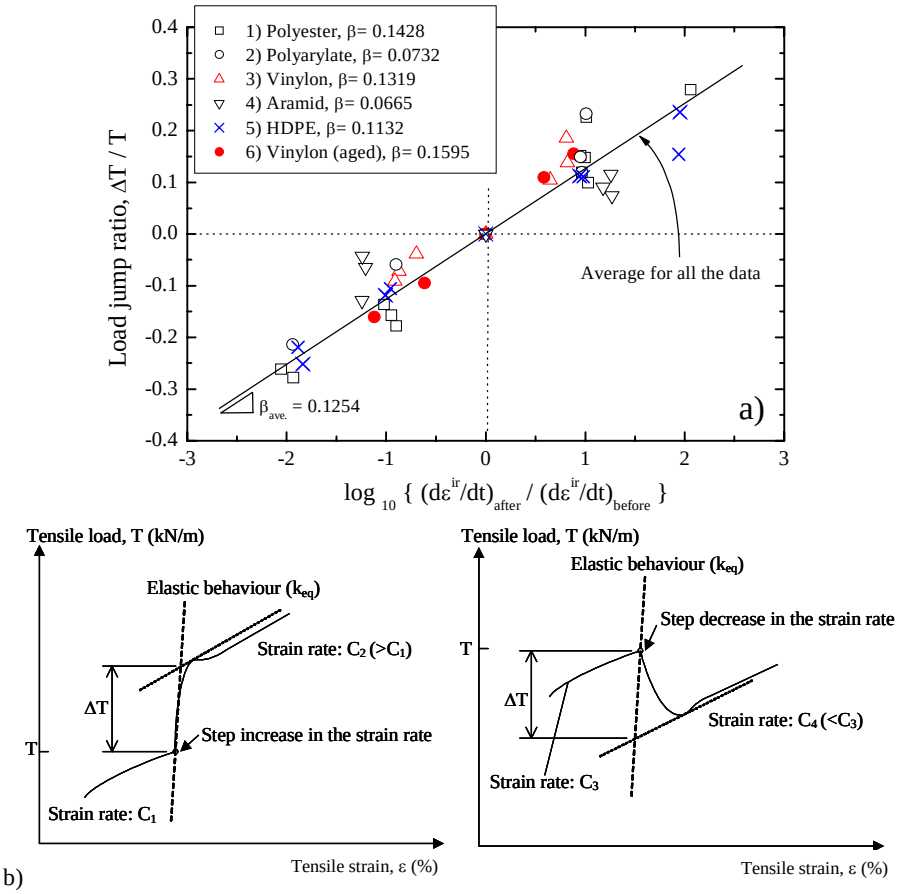

Fig. 5-13 a) Summary of measured results of load jump ratio; and b) definition of load jump (Hirakawa et al., 2004).

Table 5-2 List of β values of geogrids obtained from the literature

Reinforcement type	Range of strain rate (%/min)	Viscosity: β	References
HDPE	0.2 – 20 (0.2, 1, 10, 20)	0.2256	Hirai & Yatsu (2000)
HDPE	1 – 300 (1, 10, 60, 300)	0.3336	Bathurst et al.(1994)
HDPE	0.1 – 98.1 (0.1, 1, 10.1, 98.1)	0.2524	Shinoda et al. (2002)
PET	1 – 125 (1, 10, 125)	0.1272	Bathurst et al.(1994)
PP	0.1 – 99.3 (0.1, 1, 10, 99.3)	0.2326	Shinoda et al. (2002)

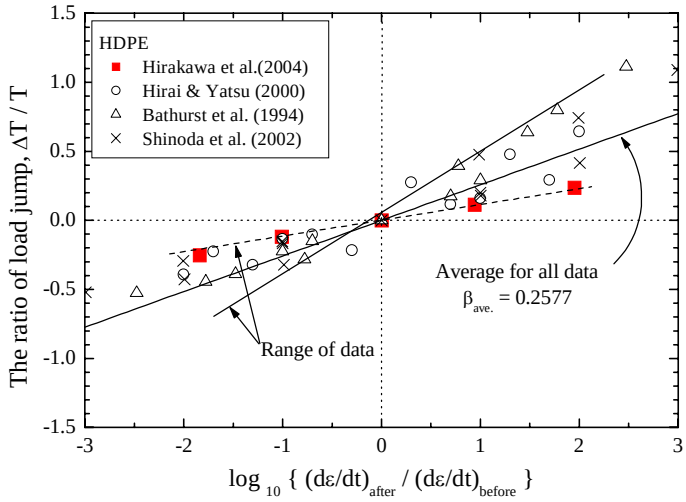

Fig. 5-14 Viscous properties of HDPE geogrid (different lots) from the literature (see Table 5-2)

The two facts above indicate that 'the general time' could not be the basic variable that controls the viscous aspects of the deformation and strength characteristics of geogrid reinforcement, showing that the isochronous concept is not relevant. That is, creep is a viscous response of the material, but it is not a degrading phenomenon due to negative ageing effects.

6 THEORETICAL FRAMEWORK FOR VISCOUS PROPERTIES

6.1 *Introduction*

A relevant constitutive model (or models) is (are) necessary for consistent understanding and description of the viscous properties of geosynthetic reinforcement, which may be subjected to arbitrary loading histories. Note that the tensile force activated in reinforcement arranged in the backfill subjected to constant external load may not be constant with time. Therefore, in a rigorous sense, results from sustained loading tests at constant load cannot be used directly to predict the residual deformation of GRS structures subjected to constant working load during a long-term service period without the test results being incorporated into a relevant constitutive model. The load-deformation-time behaviour of a GRS structure can be analysed by the FEM incorporating such a constitutive model.

Several different constitutive models describing the viscous properties of geosynthetic reinforcement have been proposed (i.e., Onaran and Findley, 1965; Helwany and Wu, 1992; Soong and Koerner, 1998; Soong and Lord, 1998; Perkins, 2000; Li and Rowe, 2001). It appears however that, to explain the whole experimental results presented in Chapter 5, a more comprehensive model is necessary.

On the other hand, based on the results from a comprehensive series of triaxial and plane strain compression tests on different types of geomaterial (i.e., soft and stiff clays, sands, gravels, sedimentary soft rocks and cement-mixed clays, sands and gravels), Di Benedetto et al. (2002) and Tatsuoka et al. (2002) showed that the viscous properties of geomaterial can be properly modelled by a non-linear three-component rheology model (**Fig. 6-1a**). This model is herein applied to geosynthetic reinforcement.

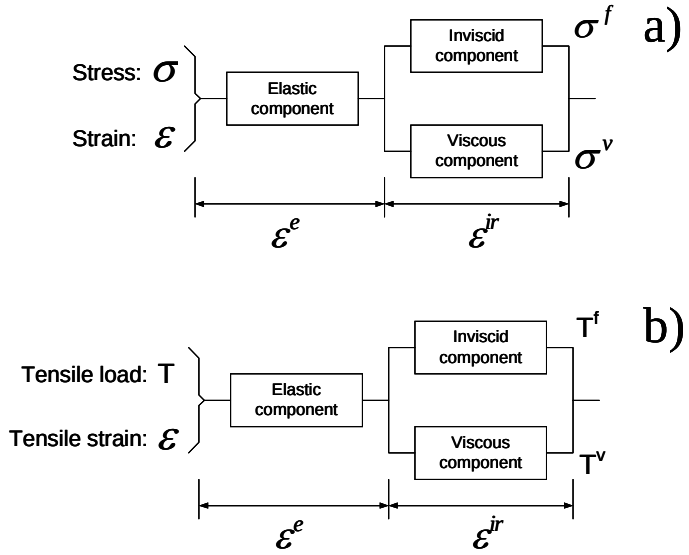

Fig. 6-1 a) Non-linear three-component rheology model developed for geomaterial (Di Benedetto et al., 2002; Tatsuoka et al., 2002); and b) three-component model modified for geosynthetic reinforcement (Hirakawa et al., 2004).

6.2 *Three-component model for geosynthetic reinforcement*

Fig. 6-1b shows the non-linear three-component model, for which the stress, σ, in Fig. 6-1a is replaced with the tensile load per unit width, *T*. The model has the following features:

1) A given strain rate, $\dot{\varepsilon}$, is decomposed into the elastic and irreversible components, $\dot{\varepsilon}^e$ and $\dot{\varepsilon}^{ir}$, as:

$$\dot{\varepsilon} = \dot{\varepsilon}^e + \dot{\varepsilon}^{ir} \qquad (6\text{-}1)$$

Loading and unloading are defined by the occurrence of positive and negative values of $\dot{\varepsilon}^{ir}$, not of load rate, $\dot{T}$. Then, even when $\dot{T}$ is negative, for example immediately after a step decrease in the strain rate or at a load relaxation stage (as shown in Figs. 5-5, 5-7, 5-8 and 5-12), the geosynthetic reinforcement is under loading conditions as long as $\dot{\varepsilon}^{ir}$ is positive.

2) The elastic strain rate, $\dot{\varepsilon}^e$, is obtained by the hypo-elastic model having the elastic modulus, $k_{eq}(T)$, that is a function of instantaneous tensile load, *T* (Hoque and Tatsuoka, 1998; Tatsuoka et al., 1999).

$$\dot{\varepsilon}^e = \dot{T} / k_{eq}(T) \qquad (6\text{-}2)$$

3) A given tensile load, *T*, is decomposed into the inviscid and viscous components, T^f and T^v, as:

$$T = T^f(\varepsilon^{ir}) + T^v(\varepsilon^{ir}, \dot{\varepsilon}^{ir}, h_s) \qquad (6\text{-}3)$$

4) The inviscid load component, $T^f(\varepsilon^{ir})$, is a unique function of irreversible strain, ε^{ir}, in the case of monotonic loading (ML). The viscous load component, $T^v(\varepsilon^{ir}, \dot{\varepsilon}^{ir}, h_s)$, is a function of ε^{ir} and $\dot{\varepsilon}^{ir}$ for the isotach viscosity. It is also a function of the strain history parameter, h_s, when the component, T^v, has decay properties (explained below). The $T^f - \varepsilon^{ir}$ relation is called the reference load-strain

relation, which becomes hysteretic under cyclic loading conditions (Tatsuoka et al., 2003; Kongkitkul et al., 2004). In the simulation shown below, the reference stress-strain relation is modelled in the same way as the conventional elasto-plastic constitutive models for geomaterial.

5) The basic variable for the viscous stress T^v is not "the general time, *t*", for which it is not possible to define the origin in the objective way (as discussed in Chapters 2 and 3). For all the geosynthetic reinforcement types having the isotach viscosity, other than reinforcement 1 (PET geogrid) listed in Table 5-1, T^v is a unique function of the instantaneous value of ε^{ir} and its rate $\dot{\varepsilon}^{ir}$ in the ML case. With reinforcement 1 and poorly graded sands, the viscous load/stress component decays with an increase in ε^{ir}, so the current viscous load/stress is controlled not only by the instantaneous values of ε^{ir} and $\dot{\varepsilon}^{ir}$ but also by recent strain history. This type of viscous property is called the TESRA type (n.b., TESRA stands for "Temporary Effects of Strain Rate and strain Acceleration") (Di Benedetto et al., 2002).

Isotach viscosity: In the ML case, the viscous load component, T^v, is obtained as:

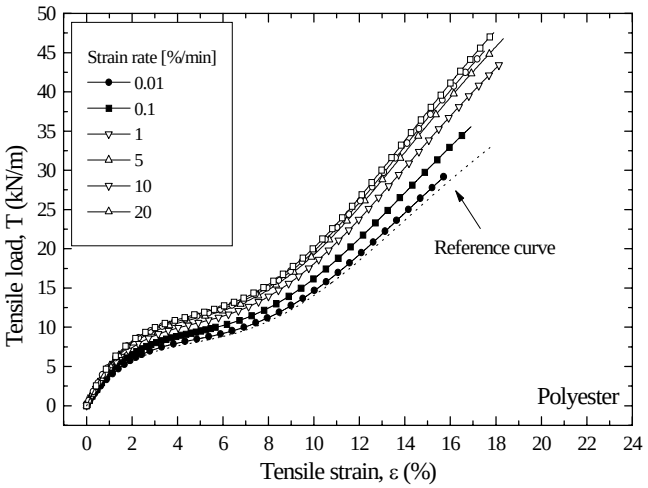

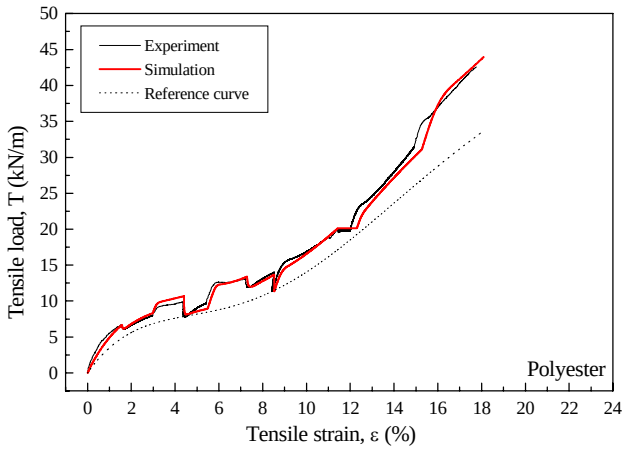

Fig. 6-2 (left) Simulation of behaviour in continuous ML presented in Fig. 5-3 by the three-component model with the combined viscosity, reinforcement 1 (PET geogrid) (Hirakawa et al., 2004).

Fig. 6-3 (right) Simulation of behaviour in ML with step changes in the strain rate and sustained loading & load relaxation presented in Fig. 5-7 by the three-component model with the combined viscosity, reinforcement 1 (PET geogrid) (Hirakawa et al., 2004).

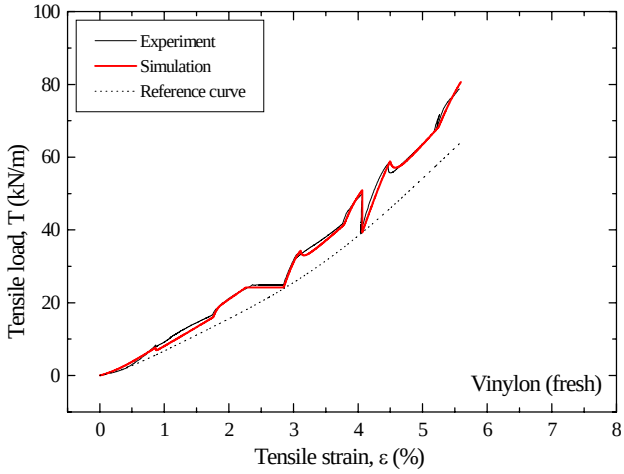

Fig. 6-4 Simulation of behaviour in ML with step changes in the strain rate and sustained loading & load relaxation presented in Fig. 5-8 by the three-component model with the isotach viscosity, reinforcement 3 (PVA geogrid) (Hirakawa et al., 2004).

$$T^v = T^v{}_{iso}\left(\varepsilon^{ir}, \dot{\varepsilon}^{ir}\right) \qquad (6\text{-}4)$$

Based on the fact that the load jump upon a step change in the strain rate, ΔT, is always proportional to the instantaneous value of T (Fig. 5-13a), Eq. 6-4 can be rewritten as:

$$T^v = T^f\left(\varepsilon^{ir}\right) \cdot g_v\left(\dot{\varepsilon}^{ir}\right) \qquad (6\text{-}5)$$

In case T^v is described in the framework of the Newtonian viscosity, we obtain:

$$T^v = \eta^*\left(\varepsilon^{ir}, \dot{\varepsilon}^{ir}\right)\cdot\dot{\varepsilon}^{ir} \quad ; \quad \eta^*\left(\varepsilon^{ir}, \dot{\varepsilon}^{ir}\right) = \frac{T^f\left(\varepsilon^{ir}\right)\cdot g_v\left(\dot{\varepsilon}^{ir}\right)}{\dot{\varepsilon}^{ir}} \quad \text{(6-6)}$$

With geosynthetic reinforcement (as with geomaterial), the parameter $\eta^*\left(\varepsilon^{ir}, \dot{\varepsilon}^{ir}\right)$ is not a constant, unlike the Newtonian viscosity.

By substituting Eq. 6-5 into Eq. 6-3, we obtain:

$$T = T^f\left(\varepsilon^{ir}\right)\cdot\left\{1 + g_v\left(\dot{\varepsilon}^{ir}\right)\right\} \quad \text{(6-7)}$$

where $g_v\left(\dot{\varepsilon}^{ir}\right)$ is the viscosity function, for which the following has been proposed for geomaterial (Di Benedetto et al., 2002: Tatsuoka et al., 2002):

$$g_v(\dot{\varepsilon}^{ir}) = \alpha\cdot[1-\exp\{1-(\frac{\left|\dot{\varepsilon}^{ir}\right|}{\dot{\varepsilon}_r^{ir}}+1)^m\}] \ (\geq 0) \quad \text{(6-8)}$$

where $\left|\dot{\varepsilon}^{ir}\right|$ is the absolute value of $\dot{\varepsilon}^{ir}$; α , m and $\dot{\varepsilon}_r^{ir}$ are the positive parameters. The viscous load component, T^v, increases with an increase in the parameter α and with a decrease in the parameter $\dot{\varepsilon}_r^{ir}$ under otherwise the same conditions. The change, ΔT^v, for a given ratio between the irreversible strain rates after and before a step change increases with an increase in the parameter *m*.

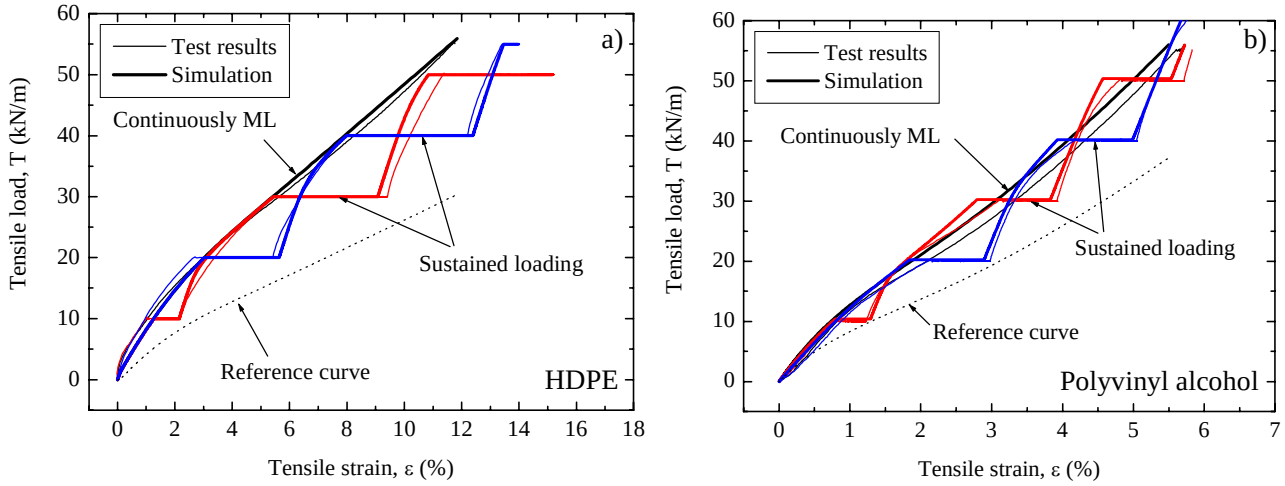

Fig. 6-5 Simulation of behaviour in load-controlled ML with sustained loading presented in a) Fig. 5-9a); and b) Fig. 5-9b) by the three-component model with the isotach viscosity, reinforcement 5 (HDPE geogrid) (Kongkitkul et al., 2004).

TESRA viscosity: As seen from Fig. 5-7, with reinforcement 1 (PET geogrid), upon the restart of ML at a constant strain rate following a sustained loading stage or upon a step increase in the strain rate during ML, the viscous component, T^v, firstly sharply increases and then decays with an increase in the strain after having shown clear yielding. Di Benedetto et al. (2002) and Tatsuoka et al. (2001, 2002) showed that such a decay of the viscous load component as described above could be accurately represented by the following TESRA viscosity component:

$$T^v = T^v{}_{TESRA}\left(\varepsilon^{ir}, \dot{\varepsilon}^{ir}, h_s\right) = \int_{\tau=\varepsilon_1^{ir}}^{\varepsilon^{ir}}\left[dT_{iso}^V\right]_{(\tau)}\cdot r_1^{\left(\varepsilon^{ir}-\tau\right)} \quad \text{(6-9)}$$

where ε^{ir} is the current irreversible strain; ε_1^{ir} is the irreversible strain at the start of loading where the viscous effect is zero ($\varepsilon_1^{ir} = 0$ in the present case); T_{iso}^v is the isotach viscosity load component obtained from Eq. 6-4; and τ is the irreversible strain when the viscous load increment, $[dT_v^{iso}]_{(\tau)}$, takes place. The function $r_1^{\left(\varepsilon^{ir}-\tau\right)}$ is called the decay function. As r_1 is a positive constant lower than unity, $r_1^{\left(\varepsilon^{ir}-\tau\right)}$ decreases with an increase in the strain difference, $\varepsilon^{ir}-\tau$. In this way, the current value of T_{TESRA}^v (when $\varepsilon^{ir} = \varepsilon^{ir}$) becomes dependent of the history of ε^{ir}. When r_1 = 1.0, T_{TESRA}^v (Eq. 6-9), becomes the same as T_{iso}^v (Eq. 6-4).

The test results presented in Fig. 5-7 indicate that, with reinforcement 1 (PET geogrid), the rate of load decay increases with an increase in the strain. To simulate this trend of viscous property, the following expression, which is more general than Eq. 6-9, becomes necessary:

$$T^v = T^v{}_{TESRA}\left(\varepsilon^{ir}, \dot{\varepsilon}^{ir}, h_s\right) = \int_{\tau=\varepsilon_1^{ir}}^{\varepsilon^{ir}}\left[dT_{iso}^v\right]_{(\tau)}\cdot\left\{r\left(\varepsilon^{ir}\right)\right\}^{\left(\varepsilon^{ir}-\tau\right)} \quad \text{(6-10)}$$

where $\left\{r\left(\varepsilon^{ir}\right)\right\}^{\left(\varepsilon^{ir}-\tau\right)}$ is the decay function and $r\left(\varepsilon^{ir}\right)$ is the parameter that decreases with an increase in ε^{ir} as:

$r(\varepsilon^{ir}) = r_i$ (positive and equal to or smaller than unity) at $\varepsilon^{ir} = 0$ (6-11a)

$$r(\varepsilon^{ir}) = \frac{r_i + r_f}{2} + \frac{r_i - r_f}{2}\cdot\cos\left\{\pi\cdot\left(\frac{\varepsilon^{ir}}{c}\right)^n\right\} \quad \text{for } 0 \leq \varepsilon^{ir} \leq c \quad \text{(6-11b)}$$

$r(\varepsilon^{ir}) = r_f$ (positive and smaller than r_i) for $\varepsilon^{ir} \geq c$ (6-11c)

The viscous property represented by Eq. 6-10 will herein be called the general TESRA property. When $r(\varepsilon^{ir}) \equiv r_i \equiv r_f$ is constant and lower than unity, Eq. 6-10 becomes Eq. 6-9.

Combined viscosity: It may be seen from Figs. 5-3 and 5-7 that reinforcement 1 (PET geogrid) exhibits the load-strain relationships that are separated from each other in continuous ML tests at constant but different strain rates and the separation becomes larger with an increase in the strain. On the other hand, reinforcement 1 has also the feature of the general TESRA viscosity described above. To combine these two features of viscosity, isotach and general TESRA, the following more general expression becomes necessary:

$$T^v(\varepsilon^{ir},\dot{\varepsilon}^{ir},h_s) = \lambda^v \cdot T^v_{iso}(\varepsilon^{ir},\dot{\varepsilon}^{ir}) + (1-\lambda^v)\cdot T^v_{TESRA}(\varepsilon^{ir},\dot{\varepsilon}^{ir},h_s) \qquad (6\text{-}12)$$

where λ^v is the material constant between zero and unity. When λ^v is equal to 1.0 and 0.0, Eq. 6-12 returns respectively to Eq. 6-4 (the isotach viscosity) and Eq. 6-10 (the general TESRA viscosity). By using a value of λ^v between 0.0 and 1.0, Eq. 6-12 can explain the trends of behaviour of reinforcement 1, as shown in the next section.

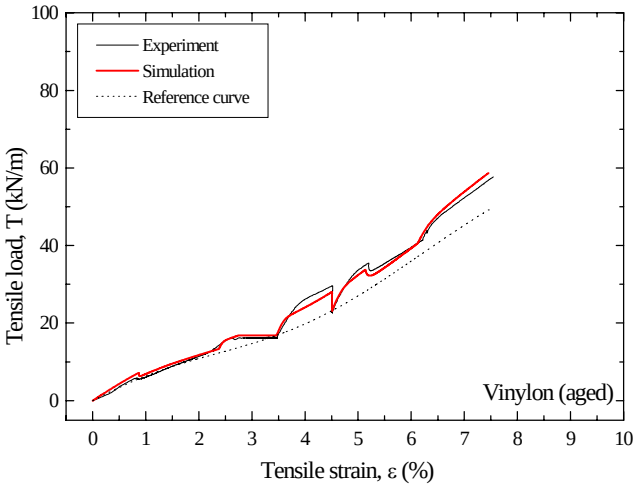

Fig. 6-6 Simulation of behaviour in ML with step changes in the strain rate and sustained loading & load relaxation presented in Fig. 5-12 by the three-component model with the isotach viscosity, reinforcement 6 (aged PVA geogrid) (Hirakawa et al., 2004).

6.3 *Simulation*

The model parameters used in the simulation were determined as follows (more details are reported in Hirakawa et al., 2004):

Elastic property: The elastic strain rate is obtained based on Eq. 6-2.

Inviscid load component: The following polynomial equation was employed to express the $T^f - \varepsilon^{ir}$ relationship (i.e., the reference relation):

$$T^f = \sum_{i=1}^{10} a_i \cdot \left(\varepsilon^{ir}\right)^{i-1} \qquad (6\text{-}13)$$

where a_i is the coefficient for term *i*, determined so that Eq. 6-13 could best fit the respective inferred load-strain relationship in ML at zero strain rates while taking into account that the load and strain state ultimately reaches at the infinite time the reference relationship during sustained loading in the case of the isotach viscosity.

Viscous load component: The respective linear relation presented in Fig. 5-13 is represented by:

$$\frac{\Delta T}{T} = \beta \cdot \log_{10}\left(\frac{\dot{\varepsilon}^{ir}_{after}}{\dot{\varepsilon}^{ir}_{before}}\right) = b \cdot \ln\left(\frac{\dot{\varepsilon}^{ir}_{after}}{\dot{\varepsilon}^{ir}_{before}}\right) \qquad (\beta = b \cdot \ln 10) \qquad (6\text{-}14)$$

As ΔT in Eq. 6-14 is equal to $(\partial T/\partial \dot{\varepsilon}^{ir})_{d\varepsilon^{ir}=0} \cdot \Delta\dot{\varepsilon}^{ir} = \Delta T^v$ for the isotach viscosity, Eq. 6-14 can be approximated by the following differential equation by referring to Eq. 6-7:

$$\frac{\Delta T}{T} \approx \frac{\Delta T^v}{T} \approx \frac{dT^v}{T} = \frac{T^f \cdot d\{g_v(\dot{\varepsilon}^{ir})\}}{T^f(\varepsilon^{ir})\cdot\{1+g_v(\dot{\varepsilon}^{ir})\}} = \frac{d\{g_v(\dot{\varepsilon}^{ir})\}}{1+g_v(\dot{\varepsilon}^{ir})} = d[\ln(\dot{\varepsilon}^{ir})^b] \qquad (6\text{-}15a)$$

$$d\left[\ln\{1+g_v(\dot{\varepsilon}^{ir})\}\right] = d\left[\ln(\dot{\varepsilon}^{ir})^b\right] \qquad (6\text{-}15b)$$

By integrating Eq. 6-15b with respect to $\dot{\varepsilon}^{ir}$, we obtain:

$$1+g_v(\dot{\varepsilon}^{ir}) = c_v \cdot (\dot{\varepsilon}^{ir})^b \qquad (6\text{-}16)$$

where c_v is a constant; and $b = \beta/\ln 10$. Eq. 6-16 is essentially valid also for the TESRA viscosity and the combined viscosity. Referring to Eq. 6-16, the parameters of the viscosity function $g_v(\dot{\varepsilon}^{ir})$ for the respective reinforcement type can be determined so that the term "$1+g_v(\dot{\varepsilon}^{ir})$" is proportional to $(\dot{\varepsilon}^{ir})^b$ for the range of $\dot{\varepsilon}^{ir}$ examined in the concerned tests.

Figs. 6-2 through **6-6** compare the simulated and measured load-strain relations for the results presented in Figs. 5-3, 5-7, 5-8, 5-9 and 5-12. The respective inferred reference curve is also presented. It may be seen that the details of viscous behaviour observed in the experiment are accurately simulated. **Fig. 6-7** compares the measured and simulated ratios of the load jump to the instantaneous load, $\Delta T/T$ (see Fig. 5-13a). A good agreement between the simulated and measured values indicates that the determined parameters of the model are relevant. **Fig. 6-8** compares the simulated and measured creep strains for the test results presented in Figs. 5-9a & b and other

similar ones (Kongkitkul et al., 2004). It may be seen that the creep behaviour for different types of geosynthetic reinforcement subjected to sustained loading at different load conditions are all well simulated.

It may be seen from the above that the proposed model can simulate rather accurately all the observed viscous aspects. It is to be particularly noted that the creep behaviour is well simulated using the parameters that were determined from the load-strain behaviour upon step changes in the strain rate. This means that, when the model parameters for a given type of geosynthetic reinforcement can be determined by relevant tests (such as ML tests with several step changes in the strain rate), the model is able to predict the load-strain-time behaviour for any other arbitrary loading histories, including long-term sustained loading. This is one of the most important features for a constitutive model that is to be incorporated into a FE analysis of the deformation and stability of GRS structure.

Among several different sub-models of the three-component model developed to describe the viscous property, introduced in the present paper, the combined type (Eq. 6-12) is most sophisticated while having a highest flexibility to represent a wide variety of viscous properties of geosynthetic reinforcement. It should be admitted, however, that the advantage described above is penalized by a high complexity in determining the model parameters. In practical applications, therefore, the isotach viscosity, the simplest one, could be used for the first approximation also for reinforcement 1 (PET geogrid), for which the model parameters could be determined rather simply.

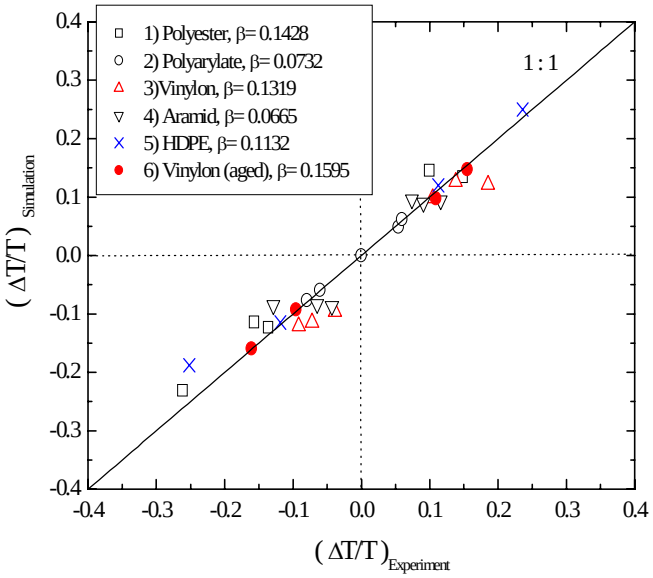

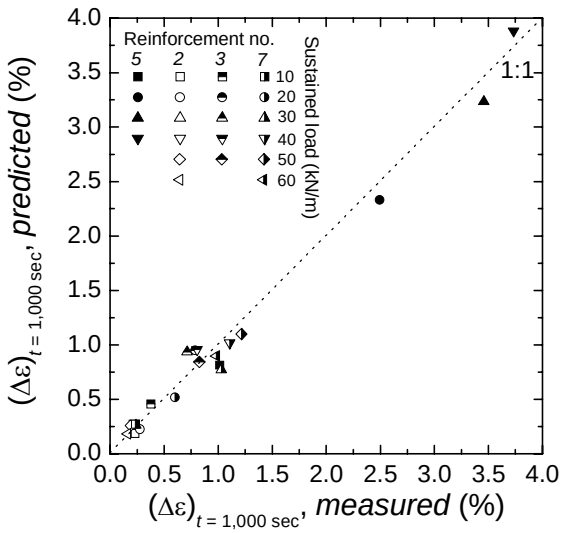

Fig. 6-7 (left) Comparison between measured and simulated load jump ratios (Hirakawa et al., 2004).
Fig. 6-8 (right) Comparison between measured and simulated creep strains (Kongkitkul et al., 2004).

6.4 Summary of Chapter 6

With most of the geogrid reinforcement types referred to in this paper, the current load is basically a function of instantaneous irreversible strain and its rate under monotonic loading condition. Only with PET geogrid, it is also a function of recent strain history. The results from the theoretical analysis described in this chapter show that the non-linear three-component rheology model that has been developed for geomaterial is also relevant to polymer geogrid, as validated by a successful simulation of the obtained test results.

7 VISCOUS BEHAVIOUR OF REINFORCED SAND

7.1 *Introduction*

For the prediction of the residual deformation during service of a GRS structure, which is often of paramount importance, it is first necessary to evaluate the viscous properties of geosynthetic reinforcement and backfill (usually sandy soil), as discussed in the preceding chapters. Tatsuoka & Yamauchi (1986), Kotake et al. (1999) and Peng et al. (2000) studied the effects of the stiffness, surface roughness and covering ratio (CR) of geogrid on the deformation and strength characteristics of reinforced sand by performing plane strain compression tests on geogrid-reinforced sand specimens and their numerical simulation by FEM. However, the viscous aspects of the load-strain behaviour of geogrid-reinforced sand mass, which would exhibit a very complicated viscous structural response reflecting an interaction between the viscous properties of these two components, have been investigated only to a very limited extent. In this chapter, the viscous properties of reinforced sand are analysed based on results from PSC tests on reinforced sand and their numerical simulation including FEM analysis. It is shown that the tensile force in geogrid reinforcement arranged in the backfill subjected to constant sustained load could decrease with time.

7.2 *Test results and analysis*

Kongkitkul and Tatsuoka (2004) performed a set of special PSC tests to evaluate the viscous properties of air-dried Toyoura sand (D_{50} = 0.2 mm) that were either unreinforced or reinforced. The specimens, 96 mm [W] x 62 mm [D] x 120 mm [H], were prepared by air-pluviation to a relative density equal to 84 – 88 %, **Fig. 7-1**. The geogrid-reinforced sand specimens had the same dimensions as the unreinforced ones, in which two sheets of PET (reinforcement 1 in Table 5-1) were arranged, each having six and ten strands in the longitudinal and transverse directions. The σ_1 and σ_2 ends of the PSC specimens were well lubricated. In all the PSC tests, the measured friction on the σ_2 surfaces was very small, which was taken into account when obtaining the average stresses acting to the specimen. Confining pressure of 30 kPa was applied by partial vacuuming. The vertical strain was measured by using both a LVDT and a pair of LDTs, while the horizontal strain was measured by using three pairs of proximity transducers. A number of pictures of the σ_2 surface, on which a number of markers had been printed on the 0.3 mm-thick specimen membrane of latex rubber (**Fig. 7-2**), were taken through the Acrylic confining platen to obtain strain fields of the specimen during each test.

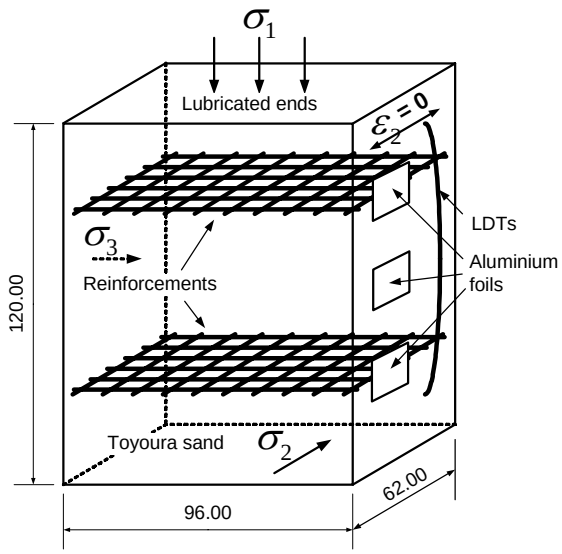

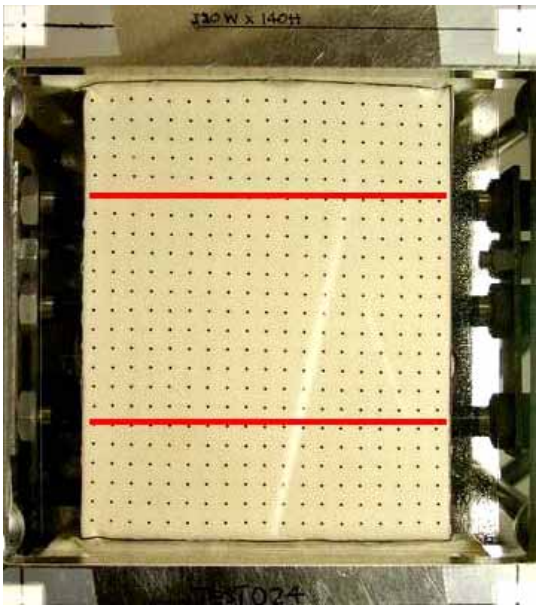

Fig. 7-1 (left) Geogrid-reinforced sand specimen in PSC (Kongkitkul & Tatsuoka, 2004).
Fig. 7-2 (right) σ_2 surface with printed markers of reinforced sand through an Acrylic platen (Kongkitkul & Tatsuoka, 2004).

7.3 *Test results and discussions*

Fig. 7-3 shows a typical test result for unreinforced sand. A global unloading and reloading cycle including several sustained loading stages at the intermediate stages was applied. The material viscosity of unreinforced Toyoura sand was quantified in terms of the slope β of the relation between "the ratio of the principal stress ratio jump, ΔR, to the current stress ratio, $R = \sigma_1/\sigma_3$" and "the logarithm of the ratio of the irreversible axial strain rates after/before a stepwise change", **Fig. 7-4a**. The β value of Toyoura sand is 0.023, which is much lower than the value of reinforcement 1 (PET geogrid) , about 0.143 (**Fig. 7-4b)**. However, the general trends of viscous behaviour of these two very different materials are surprisingly very similar and their viscous properties can be quantified in the same way, in terms of the β parameter. Fig. 7-3 also shows the simulation of the experimental result by the three-component model incorporating the TESRA viscosity (explained in Chapter 6). The parameters for the viscosity function of the three-component model were determined based on the measured β value presented in Fig. 7-4a.

Fig. 7-5 shows typical test results for reinforced sand. The stress values shown in Fig. 7-5 (and other similar figures for reinforced sand) are the average values at the specimen boundary, while the strain values are those for the whole specimen. It may be seen by comparing Figs. 7-3 and 7-5 that the strength of sand increased by a factor of about three by reinforcing, while the axial strain at peak increased by a factor of about 2.5. The reinforced sand also exhibited noticeable trends of viscous behaviour, which should be due to the viscous properties of sand and geogrid described above. The general trend of viscous behaviour of reinforced sand is very similar to those of sand and geogrid. Moreover, the β value from the average R – average ε_1 relation of the reinforced sand is very similar to that of unreinforced sand. This would be because the viscous property of the geogrid is reflected in the ε_1 values of the reinforced sand only indirectly.

On the other hand, the following obviously different trends of viscous behaviour can be seen between the two materials (geogrid and sand) and the reinforced sand. That is, with reinforcement 1 (PET geogrid; Fig. 5-7) and Toyoura sand (Fig. 7-3), when ML is restarted after a sustained loading or load/stress relaxation stage, the $T - \varepsilon$ relation and the R - ε_1 relation first slightly overshoots and then rejoins the primary relation that would be obtained from continuous ML. In contrast, immediately after the restart of ML from a sustained loading or load/stress relaxation stage, the average R – average ε_1 relation of the reinforced sand exhibits yielding at a stress level much lower than the primary loading relation (see a figure inset in Fig. 7-5). The development of viscous tensile strain component of the geogrid arranged in sand subjected to constant sustained load is controlled by the three factors illustrated in Fig. 4-1. When the effects of factors b) and c) overwhelm the effects of factor a), the tensile force in the geogrid could decrease with time. The data presented in Fig. 7-5 suggests that,

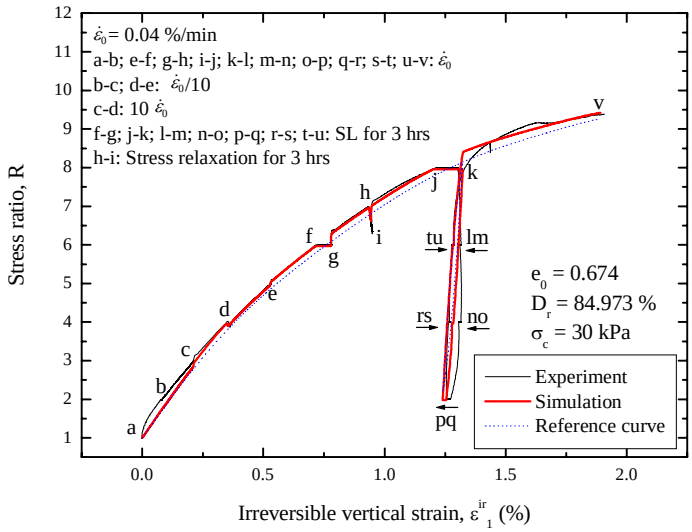

Fig. 7-3 Stress ratio, R= σ_1/σ_3 –irreversible vertical strain, ε^{ir}_1, relation of Toyoura sand obtained from a PSC test and its numerical simulation based on the TESRA model (Kongkitkul & Tatsuoka, 2004).

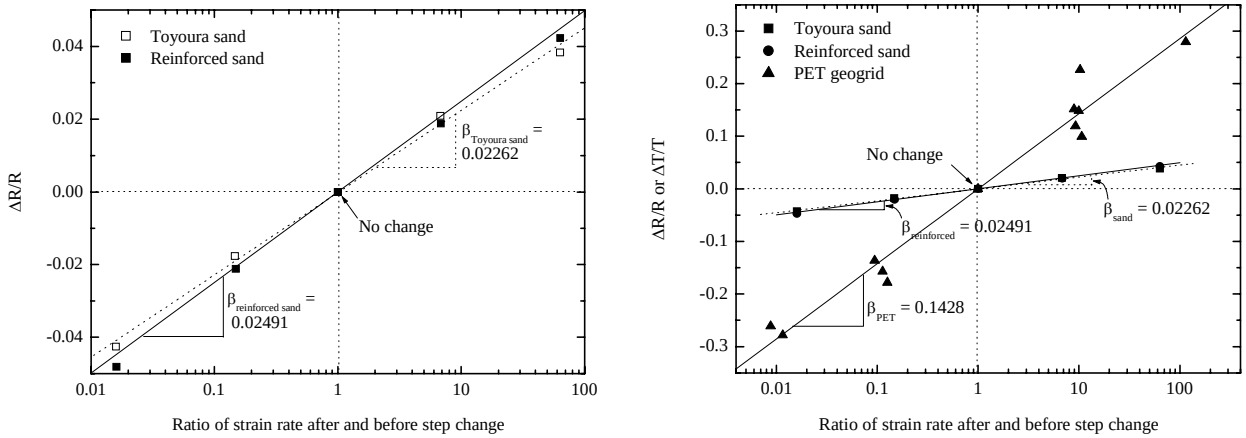

a) b)

Fig. 7-4 a) β values plots for unreinforced and reinforced Toyoura sand; and b) comparison of β values between sand and PET geogrid (Kongkitkul & Tatsuoka, 2004).

during the sustained loading, the tensile force in the geogrid arranged in sand decreased with time, which resulted in a decrease in the yield stress of reinforced sand.

To confirm this infer, another ML PSC test was performed on reinforced sand at the same nominal strain rate as the test described in Fig. 7-5 (**Fig. 7-6**). In this test, several sustained loading tests were performed during otherwise primary ML. **Figs. 7-7a** & **b** show the lateral strain fields at the start and the end (after an elapsed time of 180 minutes) of sustained loading at a stress level R = 22, obtained by the photogrametric analysis of the pictures of the specimen. The strains are defined zero at the start of PSC loading. It may be seen that the local lateral strains around the geogrid layers are noticeably smaller than the average strains of the whole specimen due to the restraining effects of the geogrid layers. The tensile strains of the geogrid (averaged for the whole length) were evaluated by assuming that the horizontal strains in the zone including the geogrid layers are the same as those of the geogrid layers. The time history of the tensile strain of the geogrid thus obtained is presented in **Fig. 7-8**.

Fig. 7-9 illustrates possible different load–strain curves (*2* through *6*) of a geogrid layer arranged in sand during sustained loading of reinforced sand, starting from a state during continuous ML at a constant strain rate. The curve *1* represents the load-strain relation of geogrid during ML at a constant strain rate of the reinforced sand. Curve *2*) represents the load-strain relation when the load applied to the geogrid is kept constant (i.e., sustained loading of geogrid), as assumed in the conventional design procedure (Chapter 2). Curve *3*) represents the relation when the strain rate is kept constant at a value lower than the one for curve *1)*. Curve *4*) represents the relation when the tensile load decreases with time. Curve *5*) represents the relation when the tensile load relaxes at a constant strain. Curve *6*) represents the relation when the tensile load decreases at a negative total tensile strain rate. It is shown below that curve *4*) is relevant to the sustained loading stage at R = 22 in the PSC test on reinforced sand presented in Fig. 7-6.

It is shown in Chapter 6 and above in this chapter that the three-component model (Fig. 6-1) can simulate very well the viscous behaviour of both geogrid and sand. **Fig. 7-10** shows the results from the simulation by the three-component model of the load-strain relationship of the PET geogrid alone that is subjected to continuous ML at a tensile strain rate of 0.047 %/minute. This strain rate is the value obtained from the tensile strain increment between R = 18 and 22 during continuous ML of the reinforced sand, evaluated by the

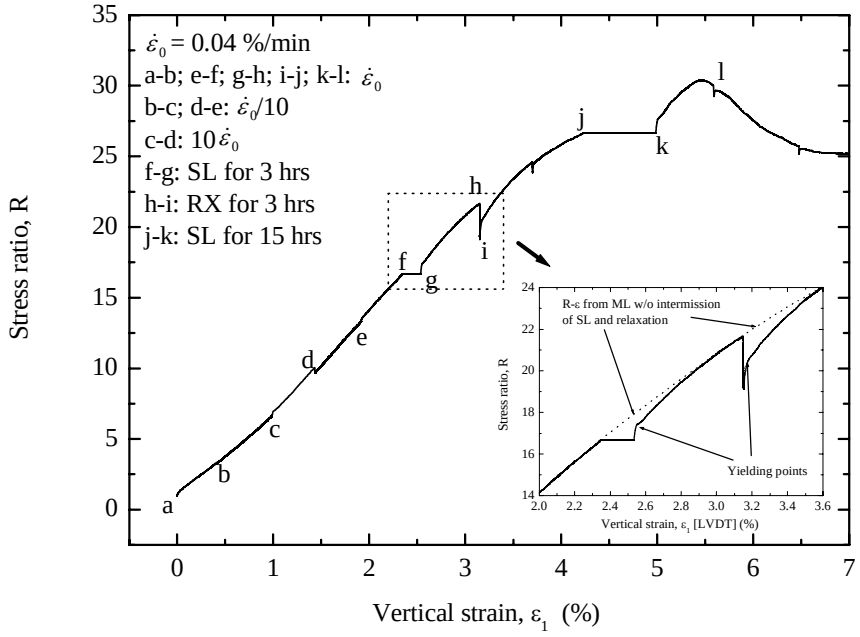

Fig. 7-5 Stress ratio, R= σ_1/σ_3 -vertical strain, ε_1, relation obtained from a PSC test of reinforced Toyoura sand (Kongkitkul & Tatsuoka, 2004).

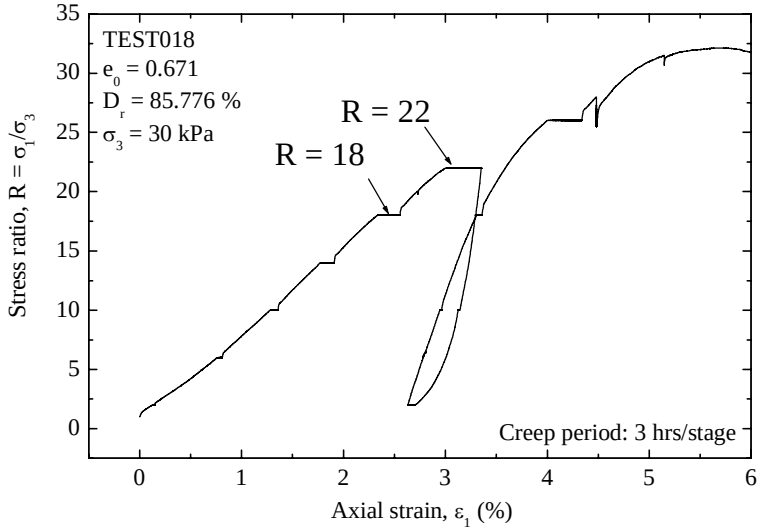

Fig. 7-6 R-ε_1 relation from a PSC test on reinforced sand with multiple sustained loading stages (Kongkitkul & Tatsuoka, 2004).

photogrametric method. It was assumed that the strain rate in the geogrid arranged in sand was kept constant at this strain rate during continuous ML of reinforced sand. Then, the load-strain-time behaviours during sustained loading at a constant load and load relaxation at a constant strain starting from point ***A*** (indicated in Fig. 7-10) were obtained by the numerical simulation. At point ***A***, the average *R* value of the reinforced sand is equal to 22. The time history of geogrid strain during the sustained loading stage (at a constant load of geogrid) is plotted in Fig. 7-8 and compared with the measured time history of geogrid strain during the sustained loading of the reinforced sand. It may be seen that the measured tensile strain increment of geogrid during the sustained loading of the reinforced sand is much smaller than the simulated creep strain increment during the sustained loading of the geogrid at a constant load. This comparison shows that the tensile force in the PET geogrid reinforcement arranged in Toyoura sand decreased with time during the sustained loading of the reinforced sand specimen.

Then, the load-strain-time relation of PET geogrid during the sustained loading of the reinforced sand was inferred as shown in **Fig. 7-11**. In this figure, the load-strain-time relations of PET geogrid during the sustained loading and load relaxation tests of PET geogrid, starting from point *A*, are depicted. The contours at elapsed times equal to 10 minutes; 1 hour; 2 hours; and 3 hours are shown in Fig. 7-11, which were obtained by assuming for the first approximation that the contours are straight. Then, the load-strain relation of the PET geogrid arranged in sand during the sustained loading of reinforced soil was obtained by substituting the strain values of PET geogrid measured at these different elapsed times into the contours. This analysis also shows that the tensile force in PET geogrid arranged in Toyoura sand decreased with time during the sustained loading of the reinforced sand specimen.

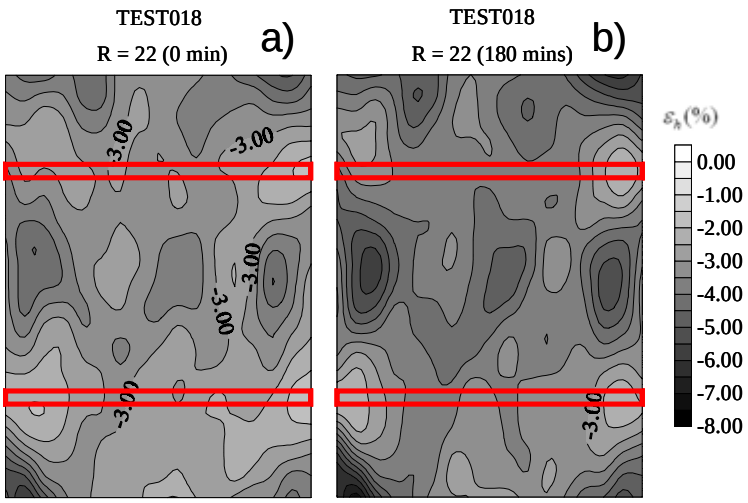

Fig. 7-7 Horizontal strain contours (Kongkitkul & Tatsuoka, 2004).

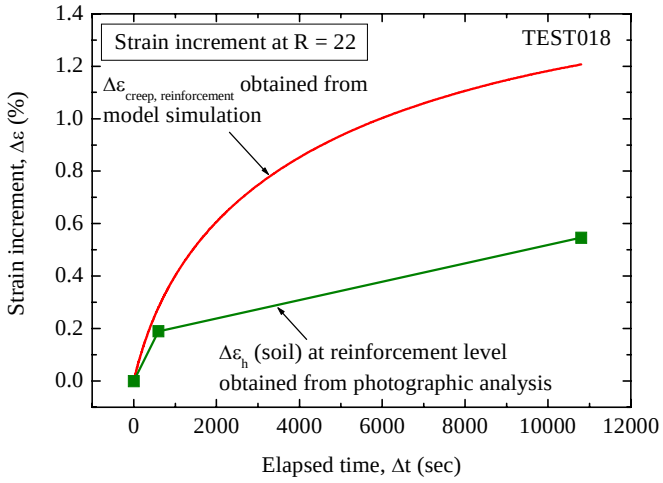

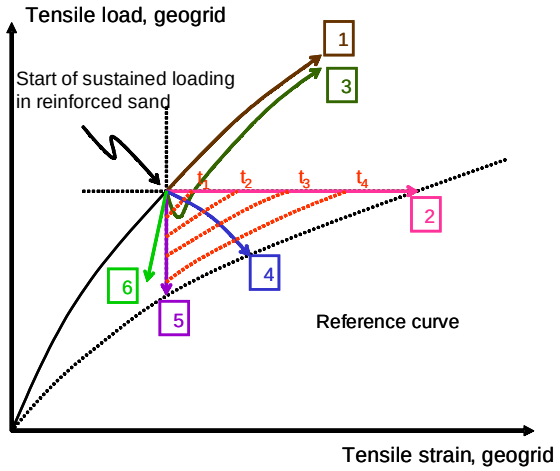

Fig. 7-8 (left) Time histories of strain of geogrid arranged in Toyoura sand during sustained loading (Kongkitkul & Tatsuoka, 2004).
Fig. 7-9 (right) Possible tensile load-strain relations of geogrid arranged in sand subjected to sustained loading (Kongkitkul & Tatsuoka, 2004).

The results shown above suggest that the tensile force of reinforcement arranged in the backfill of a prototype GRS structure (e.g., a retaining wall) having a sufficiently large structural safety factor against ultimate failure would decrease with time during service at constant working load. In that case, the possibility for creep rupture of geogrid is very low.

7.4 *FEM analysis*

Kotake et al. (1999) and Villard et al. (2002) and Peng et al. (2000) showed that the average stress and average strain behaviour of sand reinforced with a geogrid subjected to plane strain compression can be simulated by the FEM when appropriately taking into account the fact that the stress-strain properties of sand is highly non-linear with respect to strain and pressure while anisotropic exhibiting post-peak strain-softening associated with strain localisation into a shear band (or bands) having a thickness that is 10 – 20 times as large as the mean diameter of sand. For example, **Fig. 7-12** shows the large PSC specimen of air-dried Toyoura sand reinforced with a geogrid of polyvinyl alcohol (PVA, reinforcement 3 in Table 5-1). The specimens were reinforced with the geogrid layers having different structures with different rigidities and covering ratios (**Fig. 7-13**). **Fig. 7-14** shows the results from a set of drained PSC tests performed to evaluate the effects of covering ratio (CR) for the same total rigidity of geogrid (with the total rigidity ratio larger by a factor of four than the original one, type a; see Fig. 7-13). As seen from this figure, the experimental data were simulated by the FEM, in which the different covering ratios were represented by different angles of friction at the boundary between the geogrid and the adjacent sand. It may be seen that the experimental results are well simulated by the non-linear elasto-plastic FEM analysis. However, the effects of material viscosity, as discussed above, were not taken into account in this analysis.

Siddiquee et al. (2003) incorporated the three-component model (Fig. 6-1) in the code used in the FE analysis described above to simulate the viscous behaviours of sand, geosynthetic reinforcement and geogrid-reinforced sand. Kongkitkul (2004) analysed the data presented in Fig. 5-7 (from a special tensile test on the PET geogrid) and those presented in Fig. 7-5 (from a special PSC on the Toyoura sand reinforced with the PET geogrid). Fig. 7-15 shows the result from the FEM analysis incorporating the three-component model with the combined type viscosity (Chapter 6) of the tensile test, compared with the experimental data. It may be seen that the whole details of the

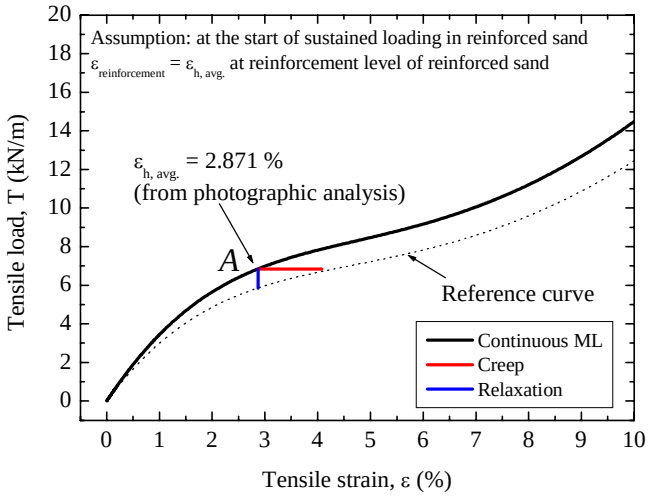

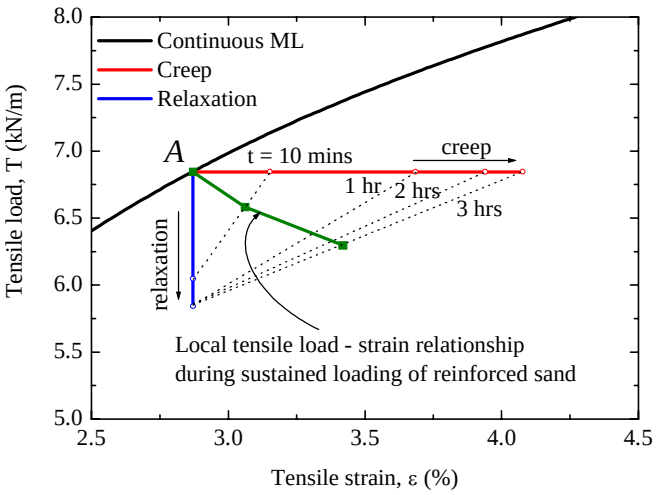

Fig. 7-10 (left) Generated tensile load-strain relations of PET geogrid subjected to three specified loading histories (Kongkitkul & Tatsuoka, 2004).

Fig. 7-11 (right) Tensile load-strain relation of geogrid during SL of reinforced sand.

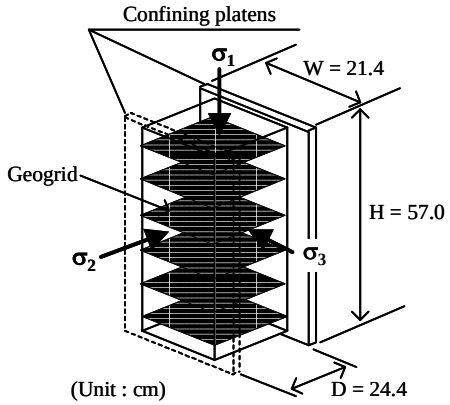

Fig. 7-12 Large PSC specimen of air-dried Toyoura sand reinforced with geogrid (Peng et al., 2000).

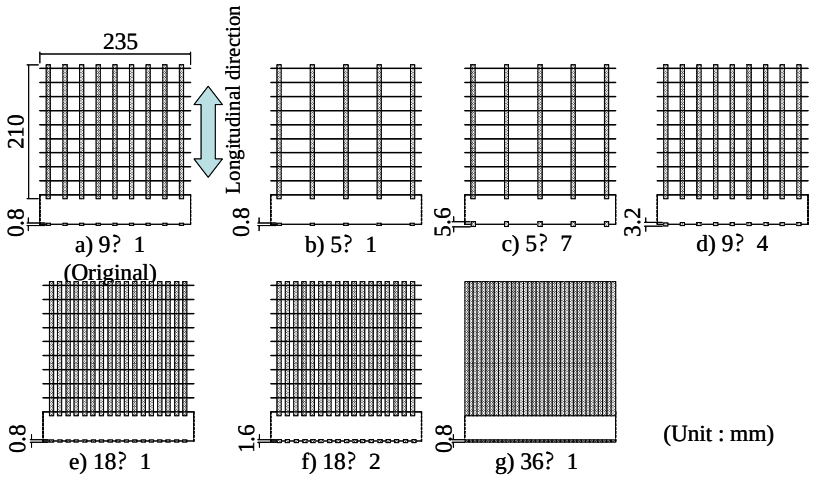

Fig. 7-13 Geogrid reinforcements used to reinforce large PSC Toyoura sand specimens (see Fig. 7-12, Peng et al., 2000).

viscous behaviour of the PET geogrid is well simulated by the FEM. Siddiquee et al. (2003) shows that the same FEM code is able to simulate very well the trends of viscous behaviour of Toyoura sand in PSC, as shown in Fig. 7-3.

After the preliminary analysis presented above, the FE analysis of the behaviour of reinforced sand was performed. The whole specimen was modelled in the FE simulation. **Fig. 7-16** shows only a part the FE model (see Fig. 7-1). The angle of internal friction of the sand elements in contact with the geogrid was made weaker by a factor of 0.857 compared with the original value of Toyoura sand following the method to simulate the conditions at the interface between the sand and the geogrid proposed by Kotake et al. (1999). That is, the average shear strength along the interface increases with an increase in the covering ratio of the geogrid under otherwise the same conditions.

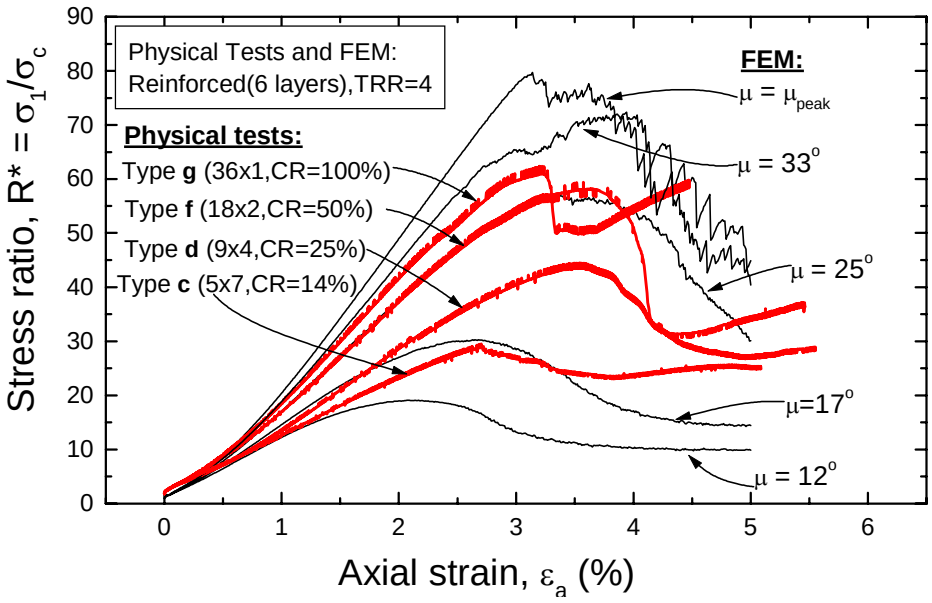

Fig. 7-14 Comparison of measured and simulated stress-strain relations of air-dried Toyoura sand specimens reinforced with geogrids having different covering ratios, plane strain compression tests at confining pressure equal to 19.6 kPa (Peng et al., 2000).

Based on the results presented in Fig. 7-14 and others, Peng et al. (2000) obtained an empirical relation between the covering ratio of the PVA geogrid in the physical experiment and the frictional angle in the boundary sand layer in the FE analysis, which was referred to in the analysis introduced here.

Fig. 7-17 shows the simulated average stress-average strain relation, compared with the measured one. It may be seen that the overall stress-strain behaviour is well simulated. Moreover, the simulated result exhibits noticeable trends of viscous behaviour with stress jumps upon step changes in the strain rate, creep deformation at sustained loading and stress relaxation that are similar to those observed in the experiment. Yet, some difference can be seen between the simulated and measured relation. More research will be required to improve the FEM analysis.

Figs. 7-18a and **b** show the local behaviours of geogrid elements 589 and 598 at the center and near the edge (see Fig. 7-16 for the locations of the elements). The following trends of behaviour may be seen:

1) The trends of viscous behaviour of the geogrid are obvious.
2) The tensile force in element 589 (near the centre) is much larger than the one in element 598 (near the edge), which is a natural consequence of the fact that shear stresses act in the outward direction along the boundary between the geogrid and the sand.
3) At stress relaxation stage 4-5, the tensile force in the geogrid decreases with time.
4) At the sustained loading stage 1-2, the tensile force in the geogrid decreases with time despite that the boundary stresses are kept constant. This trend of behaviour is the same as the one predicted by the direct numerical analysis of the PSC test result by the three-component model, as presented in Fig.7-11. This result indicates that the possibility of creep rupture of geogrid is very low even if sustained loading continues for a long period.

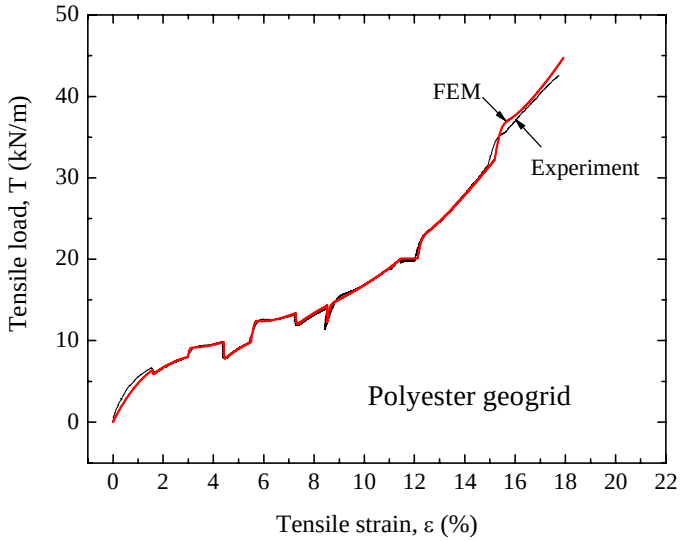

Fig. 7-15 FE simulation of the PET geogrid reinforced (Kongkitkul, 2004).

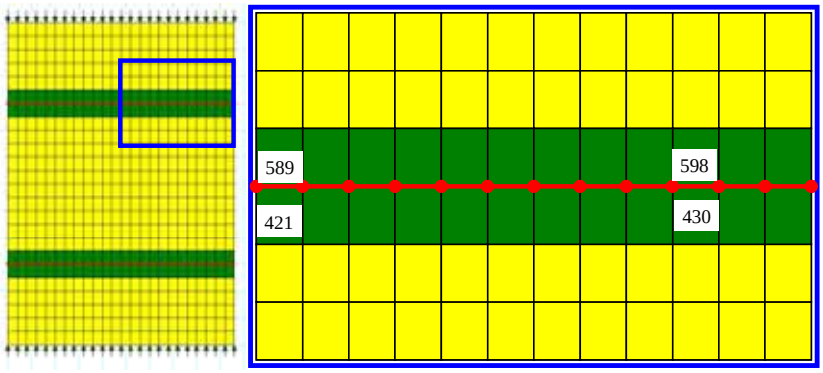

Fig. 7-16 FE model for the geo-grid reinforced Toyoura sand presented in Fig. 7-6 (Kongkitkul, 2004).

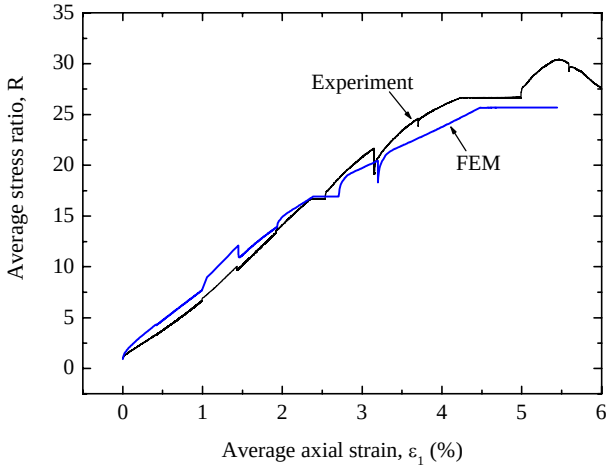

Fig. 7-17 Simulation of the average stress and average axial strain relation of geo-grid reinforced Toyoura sand in PSC presented in Figs. 7-1 & 7-5 (Kongkitkul, 2004).

Figs. 7-19a and **b** show the relationships between the vertical and horizontal normal stresses in the sand elements 421 and 430, adjacent to the geogrid elements described above (see Fig. 7-16 for the locations of the elements). Note that, due to the presence of shear stresses along the interface between the geogrid and the sand, the vertical and horizontal stresses are not equal to the major and minor principal stresses. **Figs. 7-20a** and **b** show the corresponding principal stress ratio (R) and shear strain (γ) relations. The following trends of behaviour may be seen:

1) The trends of viscous beheaviour of Toyoura sand are obvious.
2) The stress level in the element 421 (close to the centre) is much higher than that in the element 430 (close to the side boundary), corresponding to the distribution of tensile force in the geogrid.
3) At the stress relaxation stage 4-5, the local stress in sand decreases with time.
4) At sustained loading stage1-2, the horizontal stress in the central element (421) decreases with time, corresponding to the viscous behaviour of the geogrid. Because of the above, the local stress ratio (R) slightly increases with time.

7.6 *Summary of Chapter 7*

The results from experiment and numerical analysis presented in this chapter indicate that geogrid-reinforced sand can exhibit a significant trend of viscous behaviour due to the viscous properties of not only geogrid but also sand and. So, any analysis of the residual deformation by sustained loading of a GRS structure not taking into account the viscous properties of backfill, including the current design procedure based on the creep rupture curve of geosynthetic, is not relevant. The numerical analysis of the PSC test results based on the non-linear three-component model indicates that, due to an interaction between the viscous behaviours of geogrid and sand, the tensile force in the geogrid arranged in the sand specimen decreases with time during sustained loading at a constant load of the specimen. This result suggests that it could be too conservative to assume that the tensile force in the geogrid reinforcement arranged in the full-scale backfill is maintained constant during service at constant working load.

The elasto-visco-plastic FE analysis described in this chapter needs to be improved more. In particular, more researches and efforts will be necessary to apply this analysis method to full-scale GRS structures. Despite the above, it is true that it is necessary for any FE analysis to incorporate a relevant constitutive model, such as the non-linear three-component model described in Chapter 6, describing the viscous properties of both backfill and geosynthetic reinforcement so that the simulation of the residual deformation of GRS structures by the FE analysis be realistic.

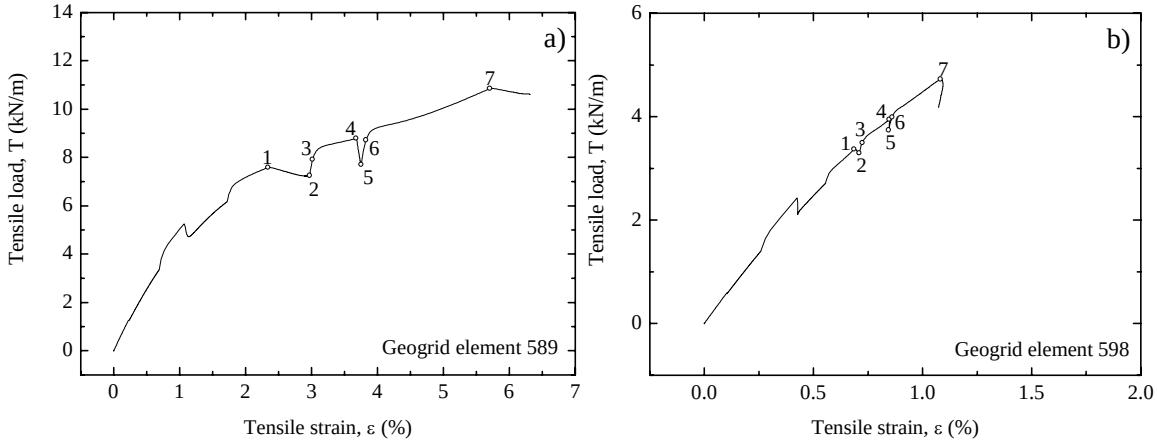

Fig. 7-18 Local force and strain relations of geogrid in element: a) 589; and b) 598 (see Fig. 7-16 for the element locations) (Kongkitkul, 2004).

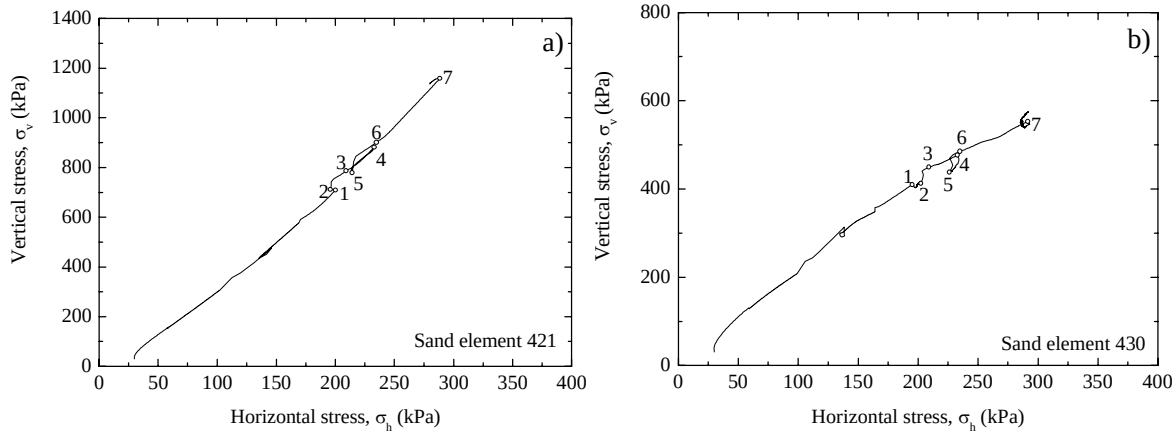

Fig. 7-19 Relationships between local vertical and horizontal stresses of sand elements: a) 421; and b) 430 (see Fig. 7-16 for the element locations) (Kongkitkul, 2004).

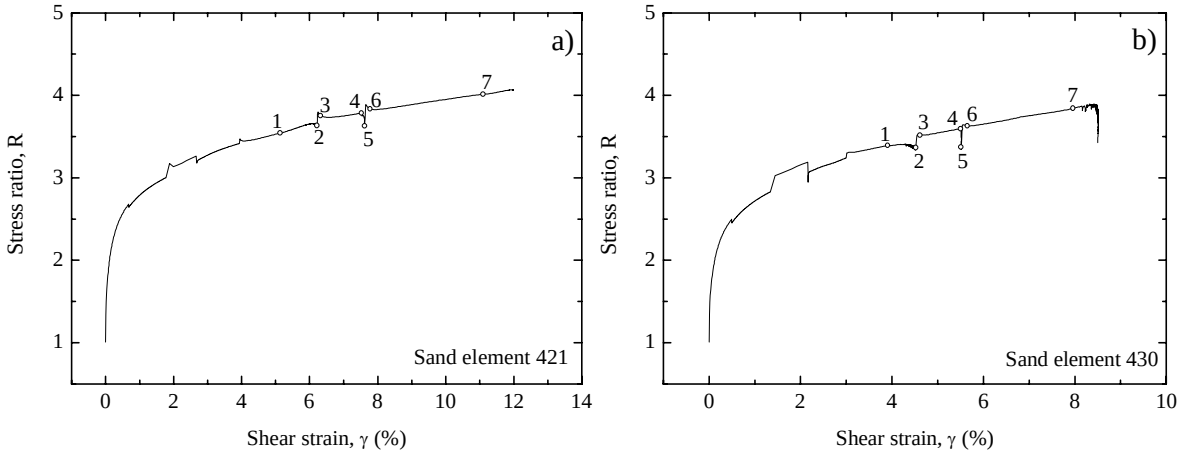

Fig. 7-20 Local R–γ relations of sand elements: a) 421; and b) 430 (see Fig. 7-16 for the element locations) (Kongkitkul, 2004).

8 BEHAVIOUR OF GEOSYNTHETIC DURING CYCLIC LOADING

8.1 *Introduction*

GRS structures could be subjected to not only sustained load resulting from the self-weight of structure and external dead load but also long-term cyclic load from traffic as well as short-term severe seismic load. Generally, the following three factors are considered to be causes for the development of residual strain in geosynthetic reinforcement subjected to cyclic loading:

I. *Rate-independent yielding due to an increase in the load level*: The maximum load level usually increases when subjected to a cyclic loading history. Unless the material behaviour is elastic, when the load level increases, residual strain increments develop by rate-independent yielding.

II. *Viscous deformation*: As shown in Chapter 5, the tensile rupture strength of geosynthetic reinforcement is basically a function of strain rate at rupture irrespective of different pre-failure loading histories, which may include sustained loading. Moreover, as shown in Chapter 6, a non-linear three-component rheology model could rather accurately simulate the load-strain-time relation of a given type of geosynthetic reinforcement subjected to a wide variety of loading history under loading conditions in the sense that the irreversible strain rate is always positive.

III. *Rate-independent effects of cyclic loading*: When this factor is relevant while the viscous effect is negligible, residual strains that develop during a given cyclic loading history are a function of cyclic loading conditions (i.e., cyclic load amplitude and the number of loading cycles and so on), while not controlled by the total period of cyclic loading. More specifically, they are not controlled by the loading frequency for a given number of loading cycle in the case of uniform cyclic loading.

The previous studies on the behaviour of geosynthetic reinforcement under cyclic loading conditions are rather limited (e.g., Bathurst & Cai, 1994; Moraci & Montanelli, 1997; Ling et al., 1998). In the following, results from some typical load-controlled cyclic and sustained loading tests performed during otherwise monotonic tensile loading at a constant load rate performed on different geosynthetic reinforcement types, including those listed in Table 5-1, are presented (Kongkitkul et al., 2004). It is shown that the residual strain that develops during a given cyclic loading history is due essentially to the intrinsic viscous properties. It is also shown that the non-linear three-component rheology model, which can simulate the viscous effects on the load-strain-time behaviour of geosynthetic reinforcement under various loading conditions, can also simulate very well results from cyclic loading tests.

8.2 *Test results and discussions*

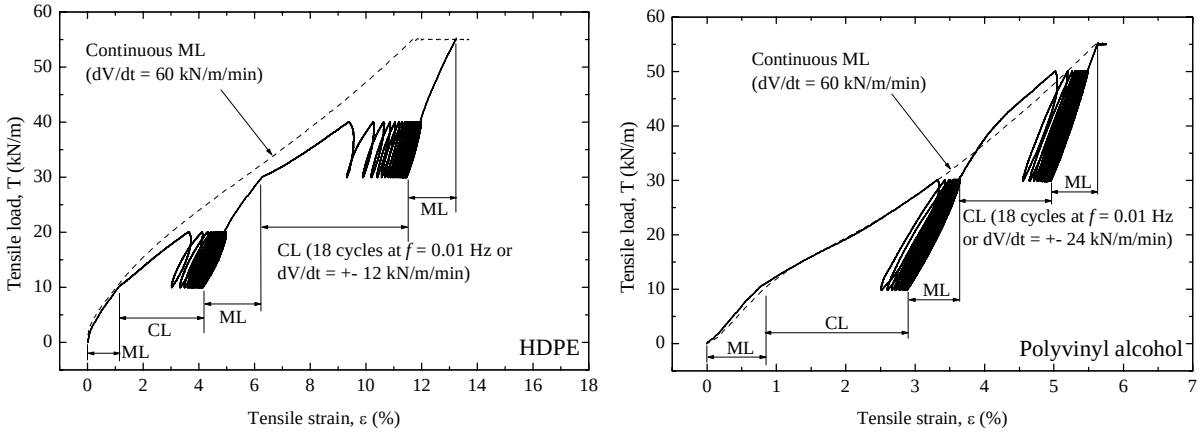

Fig. 8-1 (left) Tensile load-strain relationships from ML tests at a load rate *dV*/*dt* equal to 60 kN/m/min with and without cyclic loading (CL) at f = 0.01 Hz with 10 kN/m cyclic amplitude, reinforcement 5 (HDPE geogrid) (Kongkitkul et al., 2004).

Fig. 8-2 (right) Tensile load-strain relationships from ML tests at a load rate *dV*/*dt* equal to 60 kN/m/min with and without cyclic loading (CL) at f = 0.01 Hz with 20 kN/m cyclic amplitude, reinforcement 3 (PVA geogrid) (Kongkitkul et al., 2004).

Figs. 8-1 and **8-2** show the results from a continuous ML test and two other tests including cyclic loading (CL) stages with a load amplitude of 10 kN/m at f = 0.01 Hz on reinforcement 5 (HDPE geogrid) and with an load amplitude of 20 kN/m on reinforcement 3 (PVA geogrid). It may be seen from these figures that, when ML was restarted from the end of each CL stage, the tensile load - strain relation showed a very high tangent stiffness compared with the one observed at the same load level during continuous ML. Then, the respective curve tended to rejoin the curve during continuous ML without showing any significant effects of previous CL history on the subsequent load-strain relation at higher load levels. This trend of behaviour is essentially the same as the one observed immediately after the restart of ML from the end of sustained loading, as shown in Figs. 5-9a & b. This fact indicates that such cyclic loading histories as shown above have no deteriorating effects on the subsequent deformation characteristics and rupture strength of geosynthetic reinforcement as in the case of sustained loading (see Figs. 5-4 & 5-11).

It may also be seen that, during the respective cyclic loading history, the development of residual strain was largest during the first half cycle, which was due to the occurrence of large irreversible strain by rate-independent yielding associated with an increase in the load level exceeding the previous maximum value (factor I). The development of residual strain during the subsequent cyclic loading stage was due essentially to the viscous properties (factor II), while contributions of the rate-independent cyclic loading effects (factor III) appear very low, as shown below. **Fig. 8-3** shows the result from a special test in which a cyclic loading history was given after a sustained loading was applied for 20 minutes at the base load for the subsequent cyclic loading history (reinforcement 3, PVA geogrid). The development of residual strain during cyclic loading with and without precedent sustained loading as presented in Figs. 8-1, 8-2 and 8-3 (and others) can be simulated by a single three-component model without taking into account the rate-independent cyclic loading effects, as shown below.

In the analysis shown below, the origin for elapsed time is defined at the start of respective CL history (point ***A*** in **Fig. 8-4**). **Fig. 8-5** is a schematic diagram showing the relationship between the residual tensile strains at an elapsed time equal to 1,000 seconds, $(\Delta\varepsilon)_{t=1,000\,\mathrm{sec}}$, and those at a number of loading cycles equal to 10, $(\Delta\varepsilon)_{N_c=10}$, which would be obtained from a set of CL tests performed at different loading frequencies under otherwise the same test conditions. Note that 1,000 seconds is the loading duration of 10 cycles at f = 0.01 Hz. The following two extreme cases are illustrated in this figure:

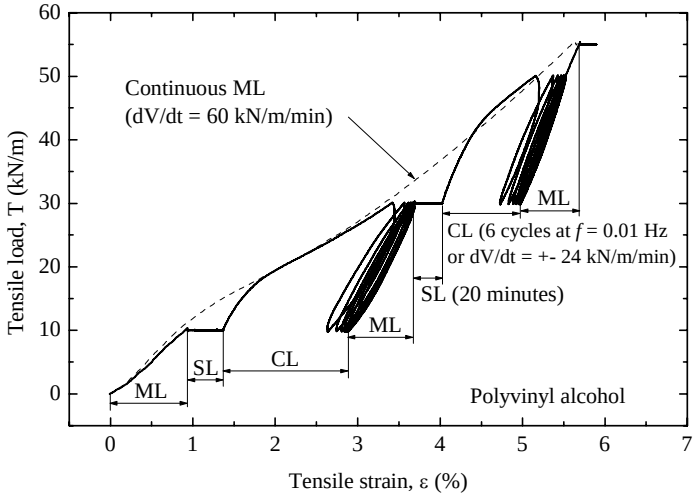

Fig. 8-3 Tensile load-strain relationships from ML tests at a load rate *dV/dt* equal to 60 kN/m/min with and without initial sustained loading (SL) & cyclic loading (CL) at f = 0.01 Hz with 20 kN/m cyclic amplitude: reinforcement 3 (PVA geogrid) (Kongkitkul et al., 2004).

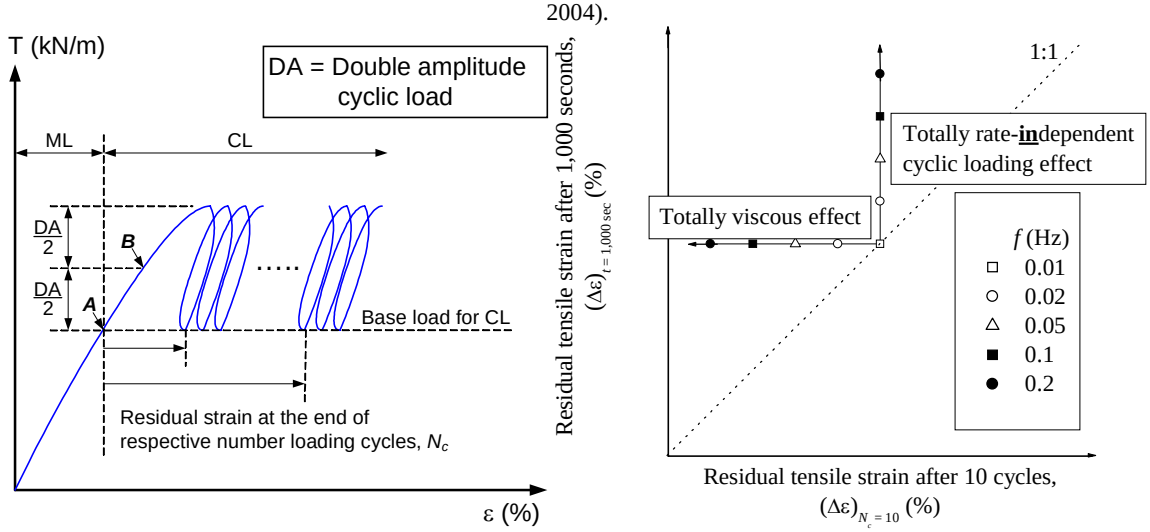

Fig. 8-4 (left) Definition of residual strain during cyclic loading and its origin (Kongkitkul et al., 2004).
Fig. 8-5 (right) Schematic diagram to illustrate the difference in the residual strain during cyclic loading between when the behaviour is totally viscous (horizontal line) and when it is due totally to rate-independent cyclic loading effect (vertical line).

a) The development of residual tensile strain during a given cyclic loading history is due solely to the viscous properties (factor II). In this case, the values of $(\Delta\varepsilon)_{t=1,000\,\mathrm{sec}}$ for different loading frequencies become essentially the same. On the other hand, the loading duration that is necessary for ten loading cycles decreases with an increase in the loading frequency. Therefore, the value of $(\Delta\varepsilon)_{N_c=10}$ decreases with an increase in the loading frequency.
b) The development of residual tensile strain during a given cyclic loading history is due solely to the rate-independent effect of cyclic loading (factor III). In this case, the values of $(\Delta\varepsilon)_{N_c=10}$ for different loading frequencies are the same, independent of the time that elapses by the end of the tenth cycles. On the other hand, the total number of loading cycles for a fixed loading duration equal to 1,000 seconds increases with an increase in the loading frequency. Therefore, the value of $(\Delta\varepsilon)_{t=1,000\,\mathrm{sec}}$ increases with an increase in the loading frequency.

Figs. 8-6 and **8-7** summarise such relationships described above from experiments for cyclic load ranges of 30 – 40 kN/m and 30 – 50 kN/m. It may be seen from these figures that, although some scatter can be observed, case *a)* above is relevant to all the tests.

8.3 *Simulation*

As shown in Figs. 6-5a & b, the results from the tests in which sustained loading tests were performed during otherwise ML at a constant load rate can be simulated very well by the three-component model using the parameters for the viscous property determined by the behaviour upon step changes in the strain rate. By using the same model parameters while not accounting for rate-independent cyclic loading effects, the results presented in Figs. 8-1 and 8-2 (and others) can also be simulated very well by the model (**Figs. 8-8a & b**). For the simulation of cyclic loading test results, a proportional rule was used to derive the inviscid hysteretic load-strain relations from the inviscid load-strain relation for ML, while the viscous load component was obtained by introducing another type of proportional rule to the inviscid load component (Kongkitkul et al., 2004).

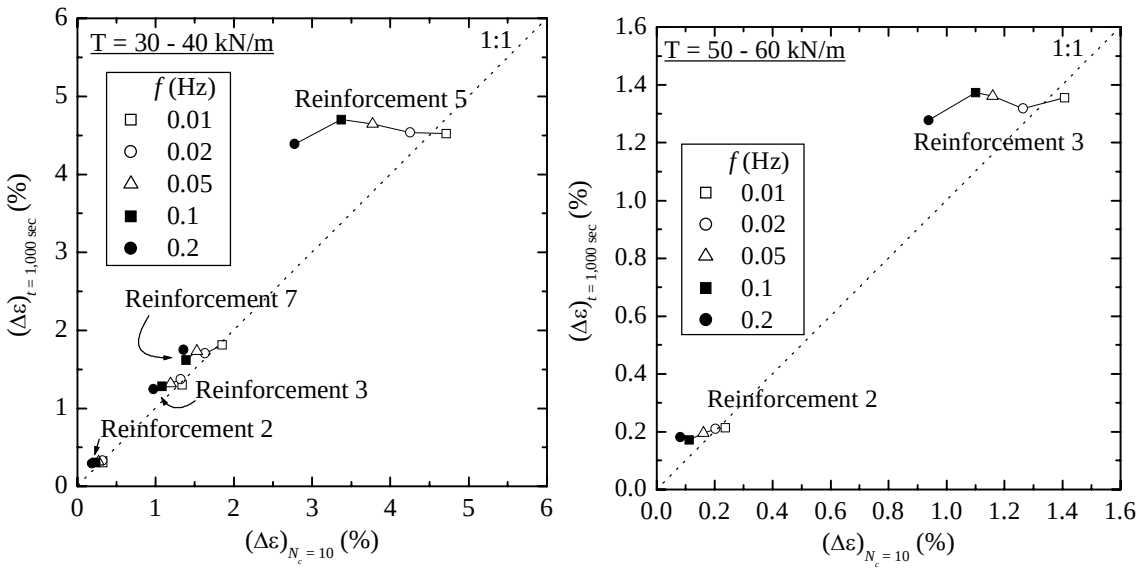

Fig. 8-6 (left) Relationship between residual tensile strains at an elapsed time equal to 1,000 seconds and at a number of cycles equal to 10 from cyclic loading tests at different loading frequencies on four types of geosynthetic reinforcement, T = 30 – 40 kN/m (Kongkitkul et al., 2004).

Fig. 8-7 (right) Relationship between residual tensile strains at an elapsed time equal to 1,000 seconds and at a number of cycles equal to 10 from cyclic loading tests at different loading frequencies on two types of geosynthetic reinforcement, reinforcements 2 & 3 (Polyarylate & PVA geogrids), T = 30 – 50 kN/m (Kongkitkul et al., 2004).

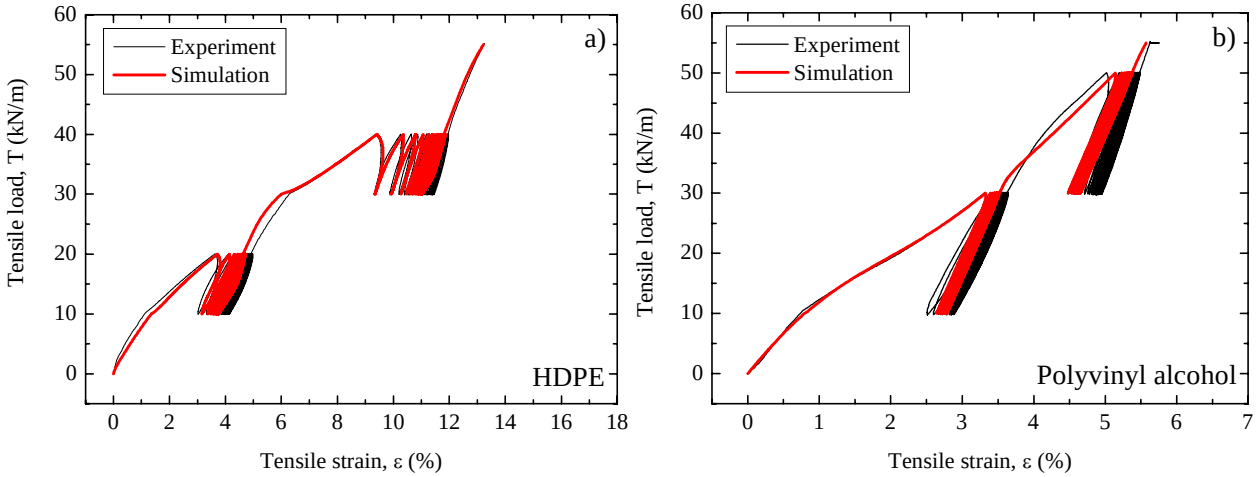

Fig. 8-8 Simulation of cyclic loading tests presented in Figs. 8-1 and 8-2: a) reinforcement 5 (HDPE geogrid); and b) reinforcement 3 (PVA geogrid) (Kongkitkul et al., 2004).

Fig. 8-9 compares the measured residual strains from the cyclic loading tests (the load amplitude is 10 kN/m, and the total loading period was 1,000 seconds) and their simulations by the non-linear three-component model. A similar comparison of the load-strain behaviour for load amplitude equal to 20 kN/m (as shown in Fig. 8-2) is presented in **Fig. 8-10**. It may be seen from these figures that the proposed model can simulate rather accurately the whole details of the viscous effects on the load-strain-time behaviour observed not only during ML but also at sustained and cyclic loading stages for all the tested types of geosynthetic reinforcements. It is to be noted that any rate-independent effects of cyclic loading (factor III) were ***not*** taken into account in these model simulations. Finally, the test results presented in Fig. 8-3 were simulated by the three-component model (**Fig. 8-11**). It may be seen from this figure that the model can simulate very well the viscous effects seen during such consecutive sustained and cyclic loading histories following monotonic loading.

It is to be noted that the same parameters with respect to the viscous properties were used to simulate results of the same type of geosynthetic reinforcement from tests using different loading histories (i.e., displacement- versus load-controlled, monotonic versus cyclic and sustained versus cyclic). The results shown above indicate again that the development of residual strain during a given cyclic loading history is due essentially to the viscous properties of polymer geosynthetic reinforcement (factor II) in addition to the development of irreversible strain increments by an increase in the inviscid load associated with cyclic loading (factor I).

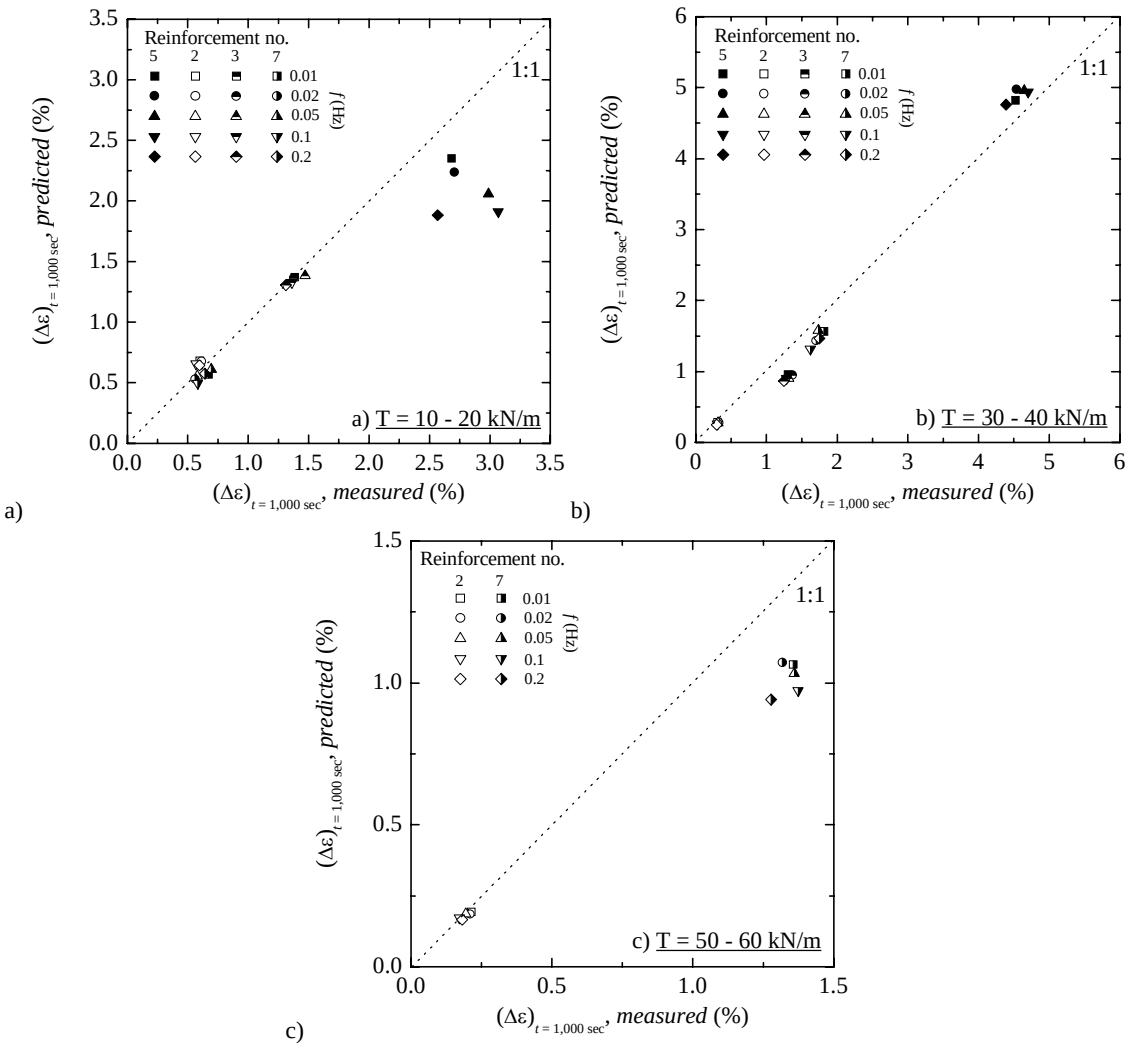

Fig. 8-9 Comparison of the predicted and measured cyclic residual strains at an elapsed time equal to 1,000 seconds: a) T = 10 – 20 kN/m; b) T = 30 – 40 kN/m; and c) T = 50 - 60 kN/m (Kongkitkul et al., 2004).

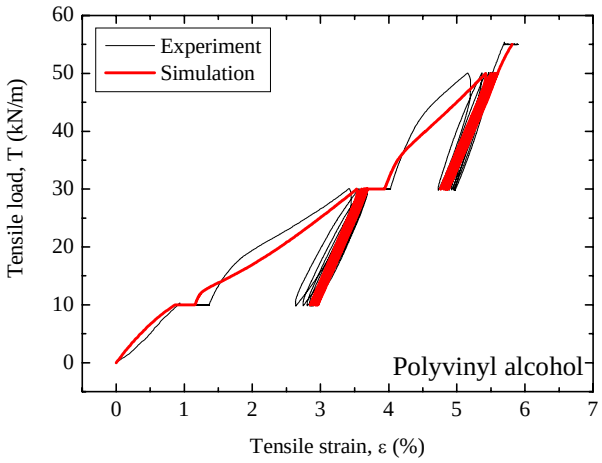

Fig. 8-11 Simulation of cyclic loading tests with initial sustained loading presented in Fig. 8-3, reinforcement 3 (PVA geogrid) (Kongkitkul et al., 2004).

8.4 *Summary of Chapter 8*

The results from experiments and simulations presented above show the followings:

1) The effects of previous sustained and cyclic loading histories disappear after having been loaded to higher load levels. This fact shows that the developments of creep strain as well as residual strain during cyclic loading are not a degradation phenomenon.

2) The development of residual strains during cyclic loading is due essentially to the material viscous properties in addition to the development of irreversible strain increments by an increase in the inviscid load associated with cyclic loading, while the rate-independent effect of cyclic loading is negligible, if any.
3) The non-linear three-component rheology model that has been validated for the load-strain-time behaviour of geosynthetic reinforcement under loading conditions with and without including intermediate sustained loading and load relaxation stages could also simulate very well all the test results obtained from cyclic loading tests.

9 EFFECTS OF PRELOADING AND PRESTRESSING

9.1 *Introduction*

The potential of creep deformation of unreinforced sand decreases by applying a relevant preloading history. This trend of behavior can be seen typically from **Fig. 9-1**, which was obtained from the PSC test on Toyoura sand described in Fig. 7-3. In this test, sustained loading tests were performed during otherwise monotonic loading, unloading and reloading at a constant strain rate. In particular, the creep strain rate became negative at sustained loading stage *l-m*, reached after relatively large unloading. **Fig. 9-2** shows results from a special tensile loading test on reinforcement 1 (PET geogrid), in which a similar loading history as above was applied. The same effects of preloading on the development of creep strain as with Toyoura sand may be seen. It is seen therefore that the possibility of creep rupture of geosynthetic reinforcement arranged in the backfill can be eliminated by applying a relevant preloading history to the reinforced soil structure.

9.2 *Effects of preloading and prestressing on the residual deformation of reinforced sand*

The effects of preloading seen with sand and geogrid reinforcement should be observed also with reinforced soil. A typical result showing the above is presented in **Fig. 9-3**, which shows the time histories of creep strain from the PSC test on geogrid-reinforced Toyoura sand described in Fig. 7-6.

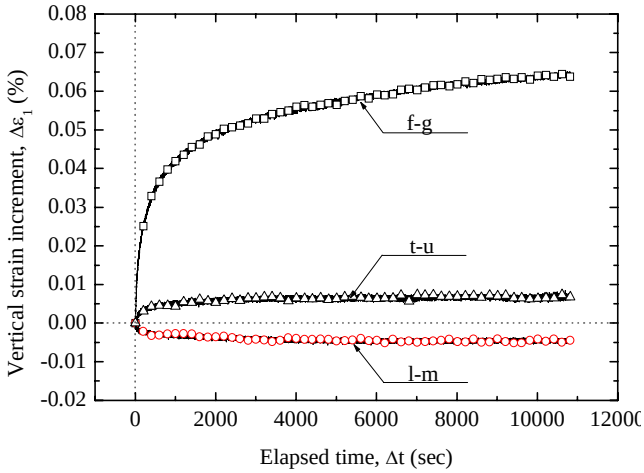

Fig. 9-1 Time of histories of axial strain at sustained loading stages f-g, l-m, and t-u, respectively, during otherwise monotonic loading, unloading and reloading, unreinforced Toyoura sand in drained PSC (see Fig. 7-3) (Kongkitkul & Tatsuoka, 2004).

Similar effects of preloading were observed on the development residual strain during a cyclic loading history in a series of model tests of reinforced-soil pier structure (**Fig. 9-4**; Shinoda et al., 2003). The backfill of the model was Toyoura sand, which was reinforced with layers of model grid reinforcement made of phosphor bronze strips. As seen from **Fig. 9-5a**, the development of residual axial strain during a given cyclic loading history decreases drastically by applying sufficiently large preload. However, a much smaller residual strain is obtained when the preload is partially unloaded before applying a cyclic loading history (**Fig. 9-5b**). This is because, before being subjected to a cyclic loading history under fully unloaded conditions, the stiffness of the backfill has become very low by a decrease in the confining pressure as well as a large swelling of the backfill taking place by full unloading, resulting in larger shear strains in the backfill during cyclic loading.. Moreover, due to the tensile force remaining in the reinforcement even when the applied vertical load becomes zero, the direction of the principal stresses in some part of the backfill may rotates by 90 degrees during cyclic loading, which could disturb largely the micro-structure of sand. These factors could result into larger residual strains. On the other hand, the effects of these factors become insignificant when subjected to cyclic loading under pre-stressed conditions. When subjected to cyclic loading with no unloading, the development of residual strain becomes large because the viscous stress, σ^v, in the backfill has not been made smaller by unloading. Similar effects of preloading and prestressing on the development of residual strain by sustained loading are reported in Uchimura et al. (2004).

A high effectiveness of preloading and prestressing in reducing the development of residual strain when subjected to long-term sustained and cyclic loading has been validated by a well-recorded full-scale behaviour of the geosynthetic-reinforced soil pier shown in **Fig. 9-6** (Uchimura et al., 2003; 2004). The bridge pier was 6.4 m x 4.4 m in cross-section and 2.7 m in height (**Fig. 9-7a**). The design dead load by the girder weight and live load by train including impact load were 196 kN and 1,280 kN. Before constructing the pier, a sub-soil layer

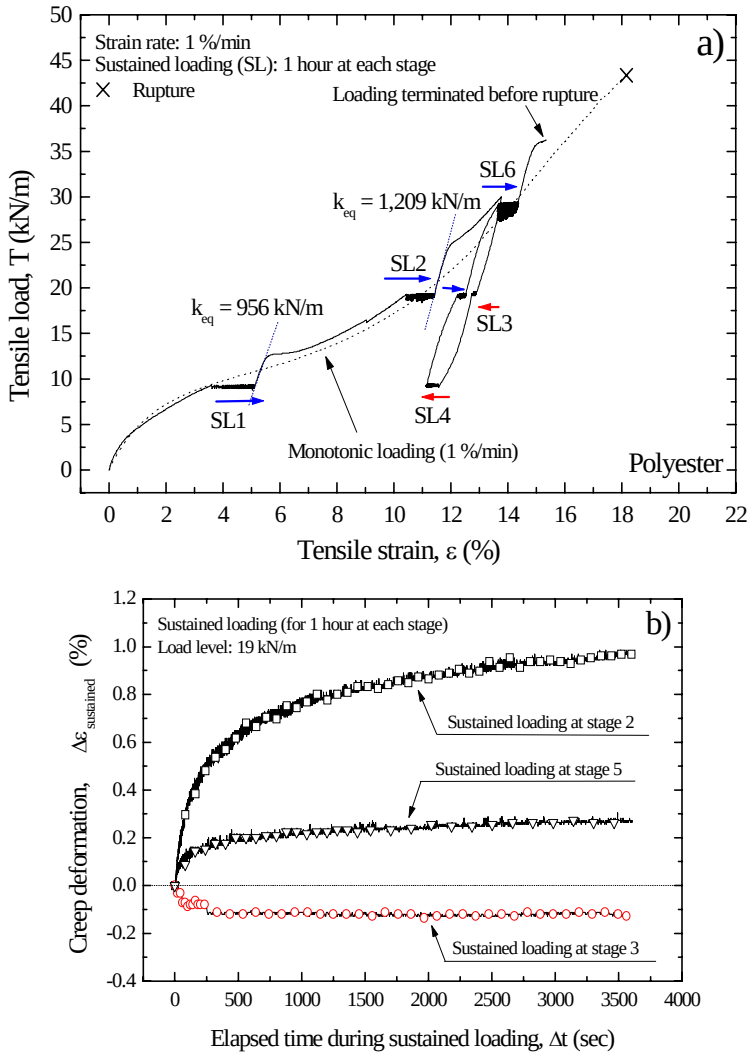

Fig. 9-2 a) Overall load-strain relation of reinforcement 1 (PET geogrid) from a tensile loading tests with sustained loading during otherwise monotonic loading, unloading and reloading; and b) time histories of tensile strains relation during sustained loading at stages 2, 3 and 5 at the same load reloading (Hirakawa et al., 2004)

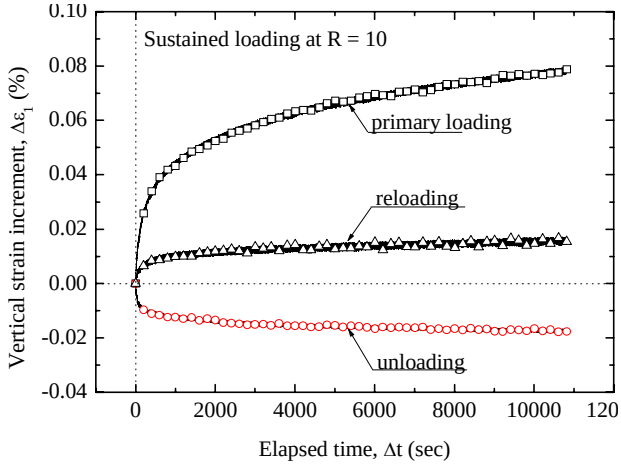

Fig. 9-3 Time of histories of axial strain at sustained loading stages (R = 10) under otherwise monotonic loading, unloading and re-loading, geogrid-reinforced Toyoura sand in drained PSC (see Fig. 7-6) (Kongkitkul & Tatsuoka, 2004).

of about 9 m-thick very soft clay was improved by producing 0.8 m-in-diameter cement-mixed-in-place soil columns. One m-thick surface clay layer below the pier was improved for the whole cross-section by cement-mixing-in-place to spread the vertical load from the backfill. The lower ends of the four steel tie rods were anchored into the cement-mixed soil columns for a length of 4 m. The nominal yield tensile force of the tie rod was 1,034 kN. Then the backfill was constructed with a help of gravel-filled bags stacked along the periphery of each

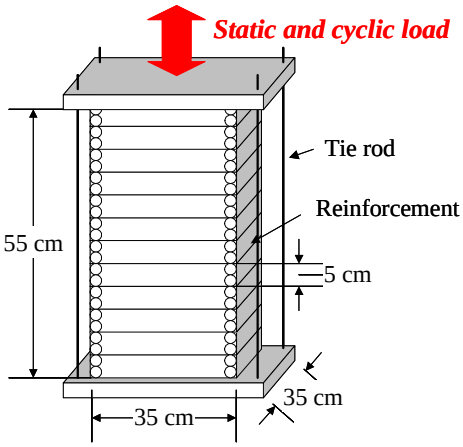

Fig. 9-4 General view of the loading system with a scaled model of reinforced soil pier structure (with four tie rods) set for loading tests (Shinoda et al., 2003a).

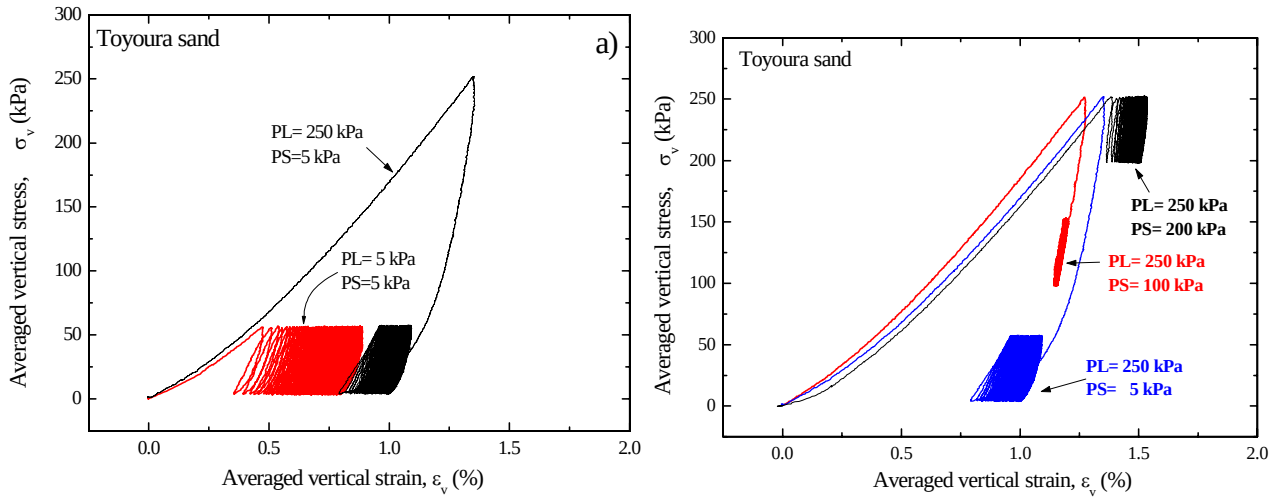

Fig. 9-5 a) Effects of preloading on residual deformation of backfill by cyclic loading (Toyoura sand without and with preloading, not using tie rods; and b) effects of prestressing on residual deformation of backfill by cyclic loading (Toyoura sand with the same preload unloaded to different stress level, not using tie rods (Shinoda et al., 2003a).

gravel layer, while the bags were wrapped around with the reinforcement. A well-graded quarry gravel of crushed sandstone (D_{max}= 30 mm, D_{50}= 0.9 mm, U_c= 16.5) was used for the backfill. The dry density of the backfill measured when demolished ranged from 1.91 to 2.17 g/cm^3, which is equivalent to 80 - 91 % of the maximum dry density (2.38 g/cm^3) obtained at the optimum water content (3.7 %) by using compaction energy of 3x10^6 m-N/m^3. The angle of internal friction, $\phi = \arcsin\{(\sigma_1 - \sigma_3)/(\sigma_1 + \sigma_3)\}_{max}$, at a confining pressure of 49 kPa was evaluated by drained triaxial compression tests on specimens (23 cm x 23 cm in cross-section times 57 cm-high) having an initial dry density of 1.95 g/cm^3 was 60°. A geogrid of polyvinyl alcohol (PVA) coated with polyvinyl chloride (PVC) was used, whose nominal rupture strength was 73.5 kN/m and the nominal stiffness was 1,050 kN/m at strains less than 1 percent. The reinforcement layers were arranged in the following very conservative way. The pier was treated as a geogrid-reinforced soil retaining wall (GRS-RW) having a full-height rigid facing at one side of the structure while having the same height as the actual pier. It was assumed that the structure would behave under plane strain conditions despite a rectangular prismatic shape of the actual pier. The vertical spacing of the reinforcement determined eventually was equal to 30 cm. The pier had two pairs of wall faces in two orthogonal directions. The two elevation sections, respectively having one pair of wall face, were designed independently. By overlapping the two sections, the actual average vertical spacing of reinforcement layers became 15 cm.

Preloading started ten days after casting-in-place a top reaction RC block (5 m-long, 2.4 m-wide and 0.8 m-high) and before casting-in-place RC facing around the backfill. A vertical preload of 2,400 kN, equivalent to an average vertical pressure of 200 kPa, was applied to the backfill of the pier through the top reaction block by using four hydraulic jacks arranged at the top of the tie rods. Then, the load was reduced to 970 kN and the top ends of the tie rods were fixed to the top RC block to maintain the compressive stress (i.e., prestress) in the backfill. Finally, full-height lightly steel-reinforced facing was cast-in-place around the backfill.

The abutment, denoted as A2 in Fig. 9-6, is a geogrid-reinforced soil retaining wall (GRS-RW) (**Fig. 9-7b**), which was constructed as one of the two abutments of the bridge. The abutment was constructed by the same method as the pier, except that it had only one nearly vertical wall face and the vertical spacing of the reinforcement layers was 30 cm. The dry density of the gravel backfill measured when demolished ranged 2.08 - 2.19 g/cm^3, which were slightly higher than that of the backfill of the pier. Both lateral sides of the backfill of the abutment were exposed slopes (1.5H:1.0V) without a facing.

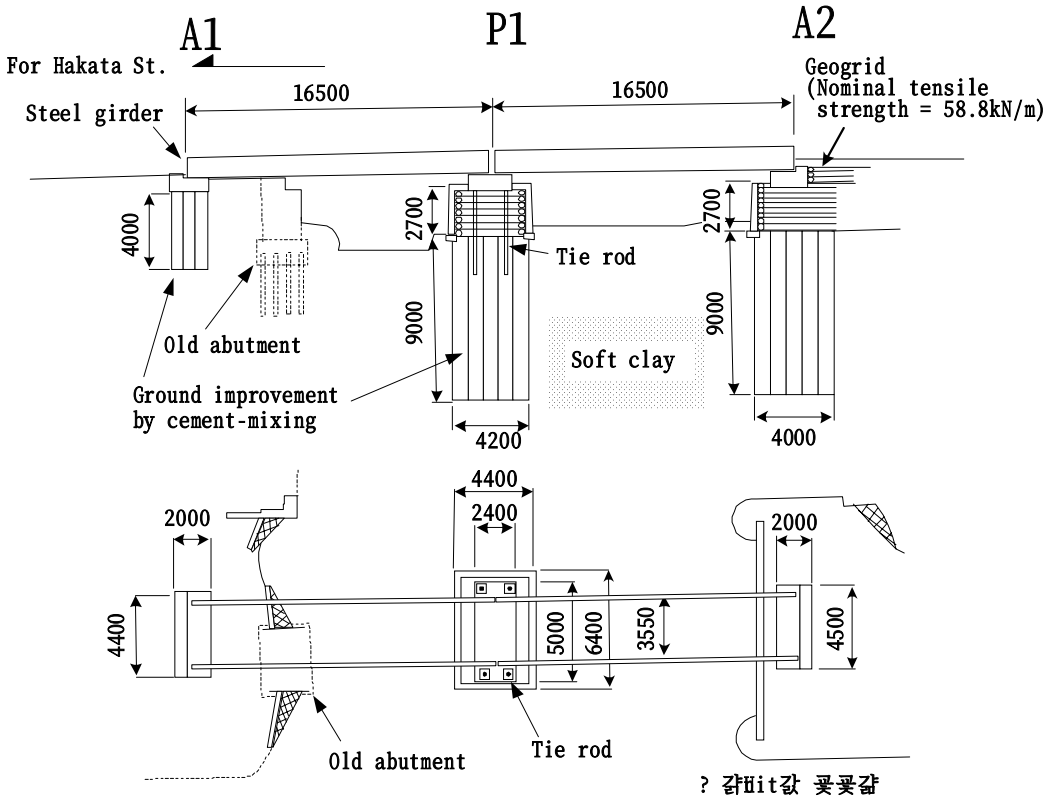

Fig. 9-6 Maidashi bridge with a PLPS GRS pier and a GRS abutment (Uchimura et al., 2003).

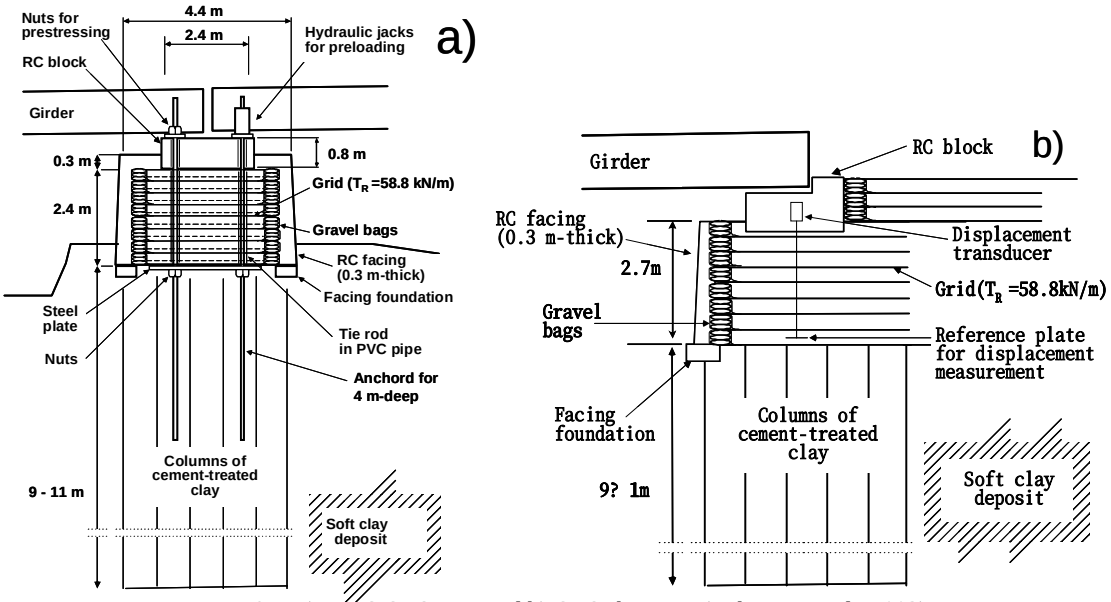

Fig. 9-7 a) PLPS GRS pier; and b) GRS abutment (Uchimura et al., 2003).

After the completion of pier P1 and abutment A2, the steel girders were placed and the bridge was left for around one year before opening to service in August of 1997. The behaviours of the pier and the abutment while the bridge was in service were continuously observed for around 3.5 years until the spring of 2001.

Fig. 9-8 shows the relationship between the tie rod tension and the vertical compression of the backfill during the preloading procedure, during service and during full-scale loading tests performed after the end of service. The tie rod tension is equal to the average vertical load applied to the top of the backfill. It may be seen from Fig. 9-8 that the behaviour during an unload/reload cycle applied between stages **17** and **18** was rather elastic while showing a compression of as small as 0.5 mm. The stiffness became substantially higher than the value during the primary loading (before stage 1) by the effect of preloading. The quasi-elastic component of the vertical compression is also shown in Fig. 9-8, which was obtained based on the results of triaxial compression tests on the backfill gravel obtained from the site. An empirical relationship for the quasi-elastic Young's modulus E_{eq}; E_{eq}= 610(σ'_a/σ'_0)$^{0.63}$, where σ'_a is the vertical compressive stress and σ'_0 is a constant equal to 100 kPa, was obtained based on the results from small amplitude cyclic loading tests performed at several

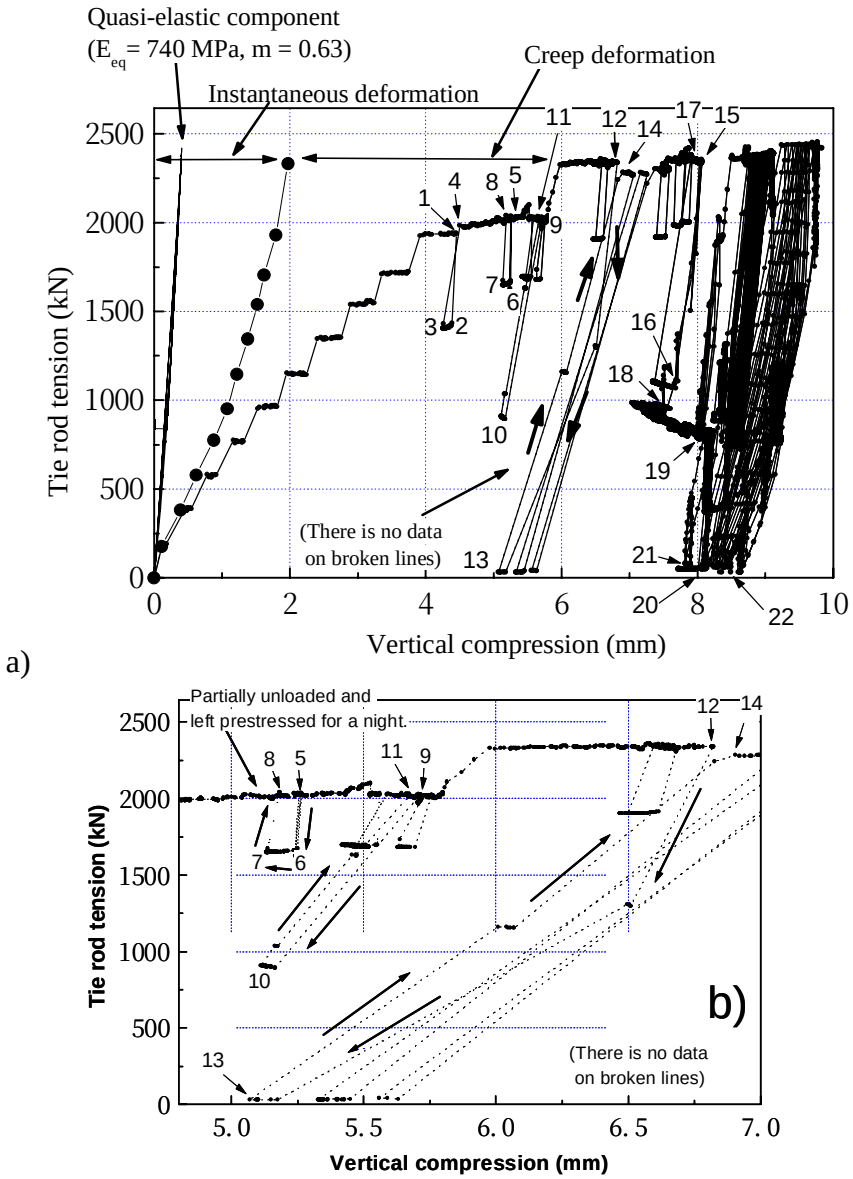

Fig. 9-8. a) Relationship between tie rod tension and compression of the pier; and b) its magnified figure (the numerals presented in this figure correspond those presented in Fig. 9-8a).

stress levels. The estimated relationship between the applied load and the quasi-elastic deformation has a similar stiffness to that of the measured curve between stages 17 and 18. The curve with solid-circle symbols presented in Fig. 9-8a denotes the relationship between the applied load and the integrated instantaneous compressive strain that occurred during the primary loading. It may be seen that most of the instantaneous strain was irreversible. The difference between the total compressive strain and the instantaneous compressive strain was also irreversible. Then, it is seen that the major part of the irreversible strain that took place until the moment when the load first became the largest value was the creep deformation that took place at constant load and the ratio of the creep strain to the total irreversible strain increased with an increase in the load level. In addition, large residual strains took place during the subsequent cyclic loading scheme. 85 % of the total strain at stage **15** was the strain that took place during the sustained and cyclic loading schemes. These facts indicate the importance of accurate evaluation of creep deformation and residual deformation by cyclic loading, which are both irreversible and time-dependent, even when estimating the deformation of well-compacted well-graded gravel. The results from the small model tests simulating this full-scale behaviour described above indicate that the residual strain that took place during the cyclic loading scheme was essentially due to the viscous property of the backfill material, not by the rate-independent effects of cyclic loading (Hirakawa et al. 2003).

Fig. 9-9 shows the full time histories of the vertical compression and the tie rod tension of the pier P1 as well as the compression of the backfill of abutment A2 by the end of service as well as those during the subsequent full-scale loading tests. Compared to a compression of 8 mm for the first 10 days at the preloading stage, the PLPS pier exhibited a compression rate of as small as about 0.25 mm/year under the prestressed condition at nearly the same rate before and after having opened to service. Correspondingly, the tie rod tension decreased only very slowly (51 kN/year). These very low rates of the compression of the backfill and the change in the tie rod tension were more

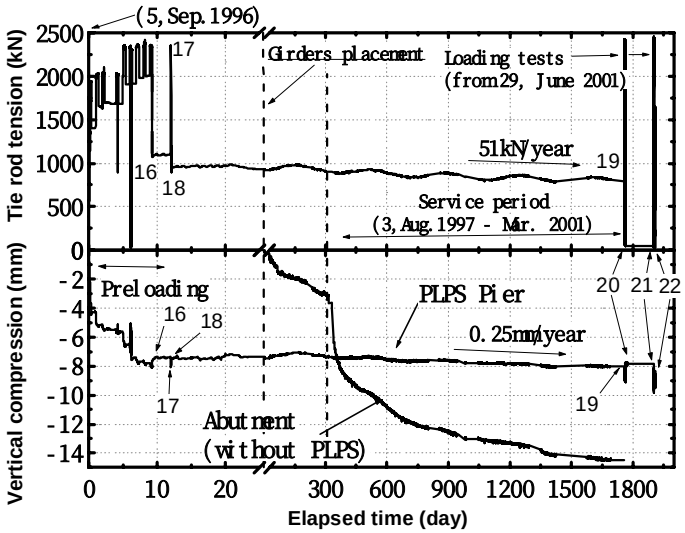

Fig. 9-9. Long-term time histories of total tie rod tension in the pier and vertical compression of the pier and abutment (the numerals presented in this figure correspond those presented in Fig. 9-8a) (Uchimura et al., 2003).

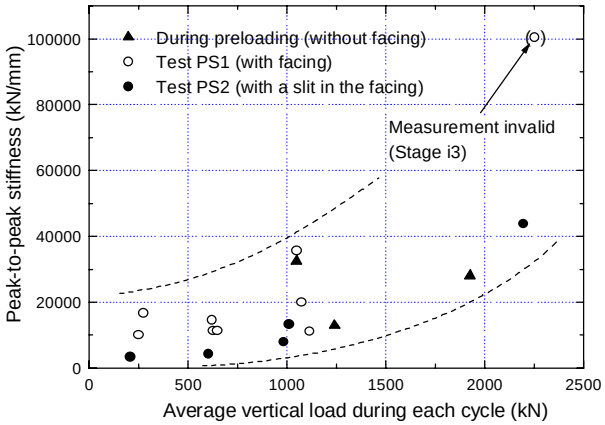

Fig.9-10 Stiffness of the pier backfill from small amplitude (400 kN) cyclic loading tests during preloading and loading tests SP1 and SP2 (Uchimura et al., 2003).

than sufficient for temporary use for about 3.5 years. On the other hand, the geogrid-reinforced backfill of abutment A2, which was not preloaded and prestressed, exhibited a substantially larger compression of about 3 mm by its own weight and the weight of the girder for 10 months after construction. Then the compression rate increased very largely upon opening to service and the compression continued for the subsequent even more than three years. These two substantially different behaviours indicate that the preloading and prestressing procedure was very effective to keep very small the vertical compression of the reinforced backfill subjected to more than 10^5 cycles of train passing.

Fig. 9-10 shows the relationships between the average stiffness and the load level of the reinforced soil pier obtained from 120 cycles of small unloading and reloading with an amplitude of 400 kN performed at several stages during otherwise global unloading and reloading in field full-scale loading tests PS1 and PS2 performed after the end of service. Despite a large scatter in the data, a general trend of decrease in the stiffness of the backfill with a decrease in the vertical stress is clear. This result confirms the paramount importance of prestressing to maintain a high stiffness of the backfill under working loading conditions.

9.3 *Summary of Chapter 9*

From the results from laboratory experiments and field full-scale behaviour, the following conclusions with respect to the residual deformation characteristics of geogrid, backfill and geogrid-reinforced backfill can be derived:

1) The development of residual strain by sustained and cyclic loading decreases substantially by applying a relevant preloading procedure.
2) The developing rate of residual deformation of backfill and reinforced backfill becomes much smaller when subjected to sustained and cyclic loading under prestressed conditions.

10 CONCLUSIONS

The following conclusions can be derived from the results from experimental studies, theoretical considerations and numerical simulations presented above:

1. Creep is not a degrading phenomenon with both geosynthetic and backfill, but it is a viscous response of a material. As with the shear strength of ordinary type backfill, the rupture strength of geosynthetic is a function of strain rate at rupture whether or not subjected to sustained loading at pre-peak intermediate stages.
2. Corresponding to the above, it is not possible to properly describe and predict the load/stress-strain-time behaviour of backfill and geosynthetic subjected to arbitrary loading histories based on the isochronous concept.
3. The design rupture strength of a given type of geosynthetic obtained by the current design procedure using a relatively large creep reduction factor determined based on the conventional creep rupture curve could be overly conservative. An alternative new procedure, which is consistent with the ordinary geotechnical design procedure, is tentatively proposed.
4. The non-linear three-component rheology model described in this paper is relevant to describe the viscous properties of backfill and geosynthetic. The constitutive model can be incorporated in an usual elasto-plastic FEM code to introduce the material viscous properties.
5. Geosynthetic reinforcement that is arranged in the backfill subjected to sustained load could decrease with time in ordinary full-scale cases, where the safety factor against ultimate failure of structure is sufficiently high.
6. The creep deformation rate can be substantially reduced, therefore, the possibility of creep rupture of geosynthetic reinforcement can be eliminated, by applying a relevant preloading history.

ACKNOWLEDGMENTS

This study was supported by the Ministry of Education, Science, Culture and Sports (a science Grant-in-Aid for Scientific Research No. 13852011). The cooperation of the previous and present colleagues of the authors is highly appreciated.

REFERENCES

Abu-Hejleh,N., Zornberg,J.G., Wang,T. & Watcharamonthein,J. 2002. Monitored displacements of unique geosynthetic-reinforced soil bridge abutments, *Geosynthetics International* 9(1): 71-95.

Allen,T.M. & Bathurst,R.J. 2002. Observed long-term performance of geosynthetic walls, and implication for design, *Geosynthetics International* 9(5-6): 567-606.

Allen,T.M., Christopher,B.R. & Holtz,R.D. 1992. Performance of a 12.6 m high geotextile wall in Seattle, Washington, *Proceedings of the International Symposium on Geosynthetic-Reinforced Soil Retaining Walls (Wu,J.T.H. eds)*: 81-100, Balkema.

Bathurst,R.J. & Cai,Z. 1994. In-isolation cyclic load-extension behavior of two geogrids, *Geosynthetics International* 1(1): 3-17.

Carrubba,P., Moraci,N. & Montanelli,F. 1999. Instrumented soil reinforced retaining wall: Analysis of measurements, *Proceedings of Geosynthetics'99* 2: 921-934.

Christensen,R.M. 1981. Residual-strength determination in polymeric materials, *Journal of Rheology* 25(4): 529-536.

Di Benedetto,H., Tatsuoka,F. & Ishihara,M. 2002. Time-dependent shear deformation characteristics of sand and their constitutive modelling, *Soils and Foundations* 42(2): 1-22.

Elias,V. & Christopher,B.R. 1996. Mechanically stabilized earth walls and reinforced soil slopes, Design and Construction Guidelines, *Publication No.FHWA-SA-96-071*. FHWA, US Department of Transportation.

FHWA. 2001. Mechanically stabilized earth walls and reinforced soil slopes design and construction guidelines, *Federal Highway Administration (FHWA), NHI Course No. 132042, (Elias,V., Christopher,B.R. and Berg,R.R.)*: 73, 114-116. Washington DC., USA.

Greenwood,J.H., Jones,C.J.F.P. & Tatsuoka,F. 2001. Residual strength and its application to design of reinforced soil in seismic areas, *Proc. of IS Kyushu (Ochia et al. eds.)* 1: 37-42. Balkema.

GRI GG1. *GRI test method GG1-87: Geogrid Rib Tensile Strength*, Geosynthetic Research Institute, Drexel University, Philadelphia, Pennsylvania, USA.

GRI GG3. *GRI GG3 Test Method (b): Tension Creep Testing of Flexible Geogrids*, Geosynthetic Research Institute, Drexel University, Philadelphia, Pennsylvania, USA.

Hayano,K., Matsumoto,M., Tatsuoka,F. & Koseki,J. 2001. Evaluation of time-dependent deformation property of sedimentary soft rock and its constitutive modeling, *Soils and Foundations* 41(2): 21-38.

Helwany,B. & Wu,J.T.H. 1992. A generalized creep model for geosynthetics, *Proc. of the International Symposium on Earth Reinforcement (Ochiai et al., eds)* 1: 79-84, Balkema.

Hirai.T. & Yatsu,A. 2000. Evaluation method about tensile strength of geogrid to use for dynamic design, *Proc. 15th Geosynthetics Symposium (Japan Chapter of IGS)*: 205-214 (in Japanese).

Hirakawa,D., Uchimura,T., Shibata,Y. & Tatsuoka,F. 2002. Time-dependant deformation of geosynthetics and geosynthetic-reinforced soil structures, *Proc. of 7th International Conference on Geosynthetics* 4: 1427-1430, Nice.

Hirakawa,D., Kongkitkul,W., Tatsuoka,F. & Uchimura,T. 2004. Time-dependent stress-strain behaviour due to viscous property of geosynthetic reinforcement, *Geosynthetics International* 10(6).

Hirakawa,D., Shibata,Y., Uchimura,T. & Tatsuoka,F. 2003. Residual deformations by creep and cyclic loading of reinforced-gravel backfill and their relation, *Proc. 3rd Int. Symp. on Deformation Characteristics of Geomaterials*. IS Lyon 03 (Di Benedetto et al. eds.), Balkema.

Hoque,E. & Tatsuoka,F. 1998. Anisotropy in the elastic deformation of materials, *Soils and Foundations* 38(1): 163-179.

Kongkitkul,W., Hirakawa,D., Tatsuoka,F. & Uchimura, T. 2003. Simulation of cyclic loading tests on geosynthetic reinforcement *Proc. 18th Geosynthetics Symposium (Japan Chapter of IGS)*: 183-190.

Kongkitkul,W. 2004. Effects of material viscous properties on time-dependent deformation of geosynthetic-reinforced sand, *PhD. Thesis*, The University of Tokyo, Japan (in progress).

Kongkitkul,W., Hirakawa,D., Tatsuoka,F. & Uchimura,T. 2004. Viscous deformation of geosynthetic reinforcement under cyclic loading conditions, *Geosynthetics International*. (accepted).

Kongkitkul,W. & Tatsuoka,F. 2004. Load-strain-time behaviour of geogrid arranged in sand subjected to sustained loading, *Proc. 39th Japan National Conf. on Geotechnical Engineering, JGS (Niigata)* (submitted).

Koseki,J., Tatsuoka,F., Munaf,Y., Tateyama,M. & Kojima,K. 1997. A modified procedure to evaluate active earth pressure at high seismic loads, *Soils and Foundations, Special Issue*: 209-216.

Kotake,N., Tatsuoka,F., Tanaka,T., Siddiquee,M.S.A. & Yamauchi,H. 1999. An insight into the failure of reinforced sand in plane strain compression by FEM simulation, *Soils and Foundations* 39(5): 103-130.

Ladd, C.C. 1991. Stability evaluation during staged construction: 22nd Terzaghi Lecture, *Journal of Geotechnical Engineering, ASCE* 117(4): 537-615.

Leshchinsky,D. 2001. Design dilemma: Use of peak to residual strength of soil, *Geotextiles and Geomembranes* 19(2): 111-125.

Li,A.L. & Rowe,R.K. 2001. Influence of creep and stress-relaxation of geosynthetic reinforcement on embankment behaviour, *Geosynthetics International* 8(3): 233-270.

Ling,H.I., Mohri,Y. & Kawabata,T. 1998. Tensile properties of geogrids under cyclic loadings, *Journal of Geotechnical and Geoenvironmental Engineering, ASCE* 124(8): 782-787.

Moraci,N. & Montanelli,F. 1997. Behavior of geogrids under cyclic loads, *Proc. Geosynthetic'97 Conf.*: 996-976.

NCMA, 1998. *Segmental Retaining Walls - Seismic Design Manual (NCMA)*, National Concrete Masonry Association (NCMA).

Onaran,K. & Findley,W.N. 1965. Combined stress creep experiments on a nonlinear visco-elastic material to determine the Kernel functions for a multiple integral representation of creep, *Trans. of the Society of Rheology* 9(2): 299-327.

Peng,F.L., Kotake,N., Tatsuoka,F., Hirakawa,D. & Tanaka,T. 2000. Plane strain compression behaviour of geogrid-reinforced sand and its numerical analysis, *Soils and Foundations* 40(3): 55-74.

Perkins,S.W. 2000. Constitutive modeling of geosynthetics, *Geotextiles and Geomembranes* 18: 273-292.

PWRI. 2000. *Design and Construction Manual for Reinforced Soil Structures using Geotextiles*, Public Works Research Institute (PWRI) (in Japanese).

RTRI. 2000. *Design Standard for Railway Earth Structures*, Railway Technical Research Institute (RTRI), Maruzen (in Japanese).

Santucci de Magistris,F., Koseki,J., Amaya,M., Hamaya,S., Sato,T. & Tatsuoka,F. 1999. A triaxial testing system to evaluate stress-strain behaviour of soils for wide range of strain and strain rate, *Geotechnical Testing Journal, ASTM* 22(1): 44-60.

Shinoda,M & Bathurst,R.J. 2004a. Strain measurement of geogrids using a video-extensometer, *Geotechnical Testing Journal* (accepted).

Shinoda,M. & Bathurst,R.J. 2004b. Lateral and axial deformation of PP, HDPE and PET geogrids under tensile load, *Geotextiles and Geomembranes* (in press).

Shinoda,M., Bathurst,R.J., Tatsuoka.F. & Horii.K. 2002. Time-dependant deformation and strength characteristics of geogrids due to viscous properties, *Proc. 17th Geosynthetics Symposium (Japan Chapter of IGS)*: 137-144 (in Japanese).

Shinoda,M., Uchimura,T & Tatsuoka,F. 2003. Increasing the stiffness of mechanically reinforced backfill by preloading and prestessing, *Soils and Foundations* 43(1): 75-114.

Siddiquee,M.S.A., Tatsuoka,F. & Tanaka,T. 2003. FEM simulation of viscous effects on the stress-strain behaviour of sand in drained PSC, *Proc. 38th Japan National Conf. on Geotechnical Engineering, JGS (Akita)* 374: 415-416.

Simac.M.R., Christopher,B.R. & Bonczkiewicz,C. 1990. Instrumented field performance of a 6 m geogrid soil wall, *Proc. of the Fourth International Conference on Geotextiles, Geomembranes and Related Products*: 53-59.

Soong,T.-Y. & Koerner,R.M. 1998. Modeling and extrapolation of creep behavior of geosynthetics, *Proceedings of the Sixth International Conference on Geosynthetics* 2: 707-710.

Soong,T.-Y. & Lord,A.E.,Jr. 1998. Slow strain rate modulus assessment via stress relaxation experiments, *Proceedings of the Sixth International Conference on Geosynthetics* 2: 711-714.

Tatsuoka,F. & Yamauchi,H. 1986. A reinforcing method for steep clay slopes with a non-woven fabric, *Geotextiles and Geomembranes* 4(3/4): 241-268.

Tatsuoka,F., Correia,A.G., Ishihara,M. & Uchimura,T. 1999. Non-linear resilient behaviour of unbound granular materials predicted by the cross-anisotropic hypo-quasi-elasticity model, *Proc. of Workshop on Modelling and Advanced testing for Unbound Granular Materials, January 21 and 22, 1999, Lisboa (Correia eds.)*: 197-204, Balkema.

Tatsuoka,F., Ishihara,M., Di Benedetto,H. & Kuwano,R. 2002. Time-dependent shear deformation characteristics of geomaterials and their simulation, *Soils and Foundations* 42(2): 106-132.

Tatsuoka,F., Koseki,J., Tateyama,M., Munaf,Y. & Horii,N. 1998. Seismic stability against high seismic loads of geosynthetic-reinforced soil retaining structures, Keynote Lecture, *Proc. 6th Int. Conf. on Geosynthetics* 1: 103-142, Atlanta.

Tatsuoka,F., Masuda,T. & Siddiquee,M.S.A. 2003. Modelling the stress-strain behaviour of sand in cyclic plane strain loading, *Journal of Geotechnical and Geoenvironmental Engineering, ASCE* 129(6): 450-467.

Tatsuoka,F., Sato,T., Park,C.-S., Kim,Y.-S., Mukabi,J.N. & Kohata,Y. 1994. Measurements of elastic properties of geomaterials in laboratory compression tests, *Geotechnical Testing Journal, ASTM* 17(1): 80-94.

Tatsuoka,F., Tateyama,M, Uchimura,T. & Koseki,J. 1997. Geosynthetic-reinforced soil retaining walls as important permanent structures, 1996-1997 Mercer Lecture, *Geosynthetics International* 4(2): 81-136.

Tatsuoka,F. 2001. Impacts on Geotechnical Engineering of Several Recent Findings from Laboratory Stress-Strain Tests on Geomaterials, 2000 Burmister Lecture at Columbia University, *Geotechnics for Roads, Rail Tracks and Earth Structures (Correia & Brandle eds.), Balkema:* 69-140.

Tatsuoka,F., Uchimura,T., Hayano,K., Di Benedetto,H., Koseki,J. & Siddiquee,M.S.A. 2001. Time-dependent deformation characteristics of stiff geomaterials in engineering practice, Theme Lecture, *Proc. of the Second International Conference on Pre-failure Deformation Characteristics of Geomaterials, Torino, 1999, Balkema (Jamiolkowski et al., eds.)* 2: 1161-1262.

Uchimura,T., Tateyama,M., Tanaka,I. & Tatsuoka,F. 2003. Performance of a preloaded-prestressed geogrid-reinforced soil pier for a railway bridge, *Soils and Foundations* 43(6): 155-172.

Uchimura,T., Tatsuoka,F., Hirakawa,D. & Shibata,Y. 2004. Residual deformations of geosynthetic-reinforced soil structure subjected to sustained and cyclic loading, *Proc. 3nd European Geosynthetics Conference, EuroGeo3,* Munich.

Villard,P., Kotake,N. & Otani,J. 2002. Modelling of reinforced soil in finite element analysis, Keynote Lecture, *Proc. of 7th International Conference on Geosynthetics* 1: 35-95, Nice."